



THE HONG KONG
POLYTECHNIC UNIVERSITY

香港理工大學

Pao Yue-kong Library

包玉剛圖書館

Copyright Undertaking

This thesis is protected by copyright, with all rights reserved.

By reading and using the thesis, the reader understands and agrees to the following terms:

1. The reader will abide by the rules and legal ordinances governing copyright regarding the use of the thesis.
2. The reader will use the thesis for the purpose of research or private study only and not for distribution or further reproduction or any other purpose.
3. The reader agrees to indemnify and hold the University harmless from and against any loss, damage, cost, liability or expenses arising from copyright infringement or unauthorized usage.

IMPORTANT

If you have reasons to believe that any materials in this thesis are deemed not suitable to be distributed in this form, or a copyright owner having difficulty with the material being included in our database, please contact lbsys@polyu.edu.hk providing details. The Library will look into your claim and consider taking remedial action upon receipt of the written requests.

FLEXIBLE BROADBAND ACOUSTIC METAMATERIALS

LIANG SHANJUN

PhD

The Hong Kong Polytechnic University

2020

The Hong Kong Polytechnic University

Department of Mechanical Engineering

Flexible Broadband Acoustic Metamaterials

LIANG Shanjun

A thesis submitted in partial fulfilment of the requirements for
the degree of Doctor of Philosophy

August 2019

CERTIFICATE OF ORIGINALITY

I hereby declare that this thesis is my own work and that, to the best of my knowledge and belief, it reproduces no material previously published or written, nor material that has been accepted for the award of any other degree or diploma, except where due acknowledgement has been made in the text.

_____ (Signed)

LIANG Shanjun _____ (Name of student)

ABSTRACT

Metamaterials are artificial structures designed to provide exotic properties and unconventional functionalities for wave control. In the past two decades, the concept of acoustic metasurfaces has been developed as an evolution of acoustic metamaterials, allowing realization of wavefront modulation or absorption with meta-lenses in a planar profile. This thesis focus on how to broaden the bandwidth of acoustic metasurfaces and match their impedance to that of the surrounding materials. It may as well provide strategy that enhance the flexibility of metasurfaces. The work aims to optimize the properties of metasurfaces for practical application scenarios.

After a review of metamaterials and metasurfaces, the research work in this thesis starts with a thorough investigation of gradient helicoid metamaterials both with theoretical exploration and experimental demonstration. By using relatively larger pitch at both end of the helicoid unit-cell, the interface between metamaterial and the background media gets better impedance matching over a large frequency range and weakens the Fabry–Pérot resonance. The phase shift over spectra is also in a gentle slope. The “V”-shaped pitch distribution of helicoid metamaterial brings broadband focal lens, which has been verified in experiment. The monotone distribution of pitch offers an ideal broadband sound amplifier. The following chapter focuses on the modular design of metasurface for anomalous refraction to provide adjustable refractive angle. This work opens a new freedom of metasurface design based on the rearrangement of unit-cells. A modular-designed metasurface shows three different working modes when reordering their unit-cells. The phenomena have been experimentally demonstrated. To show the practicality of anomalous refraction, a broadband Bessel beam launcher is realized. Final part is theoretical generalization of helicoid metamaterial. The formation

of helicoid metamaterial has been demonstrated both for their shape and acoustic characteristics. A spiralling metamaterial is proposed as a general model. This model gives an analytical description to the effective impedance and refractive index. Furthermore, this new developed general model can perfectly match the impedance to the background media and inherits all the advantages of helicoid metamaterials. A three-dimensional wavefront converter has been designed and experimentally measured to show its functionality and broadband performance.

Publications arising from the thesis

Journals

S. Liang, T. Liu, F. Chen, J. Zhu, Theoretical and experimental study of gradient-helicoid acoustic metamaterial. *Journal of Sound and Vibration*, (2018).

T. Liu, **S. Liang**, F. Chen, J. Zhu, Inherent losses induced absorptive acoustic rainbow trapping with a gradient metasurface. *Journal of Applied Physics* 123, 091702 (2018).

T. Liu, X. Zhu, F. Chen, **S. Liang**, J. Zhu, Unidirectional Wave Vector Manipulation in Two-Dimensional Space with an All Passive Acoustic Parity-Time-Symmetric Metamaterials Crystal. *Physical review letters* 120, 124502 (2018).

Conferences

S. Liang, T. Liu, F. Chen, J. Zhu, in *INTER-NOISE and NOISE-CON Congress and Conference Proceedings*. (Institute of Noise Control Engineering, 2017), vol. 255, pp. 1839-1843.

S. Liang, T. Liu, H. Gao, F. CHEN, J. Zhu, A kind of polar coordinate system adaptable metasurface and its broadband wavefront manipulation. *The Journal of the Acoustical Society of America* 144, 1676-1676 (2018). (ASA conference)

ACKNOWLEDGEMENTS

First and foremost, I would like to thank my chief supervisor, Dr. ZHU Jie, for providing me a wonderful opportunity to finish the PhD program. During the whole process, I would not have completed the study without his understanding, support and encouragement. His invaluable guidance and suggestion are greatly appreciated. Meanwhile, my deep appreciation is dedicated to my co-supervisor, Dr. CHOY Yat Sze, who gave me generous help in the daily life and great support for career planning. I wish to thank Dr. JING Yun from North Carolina State University who gave me a precious opportunity in the attachment program as a host supervisor. The experience broadens my views on the specific research field of acoustic metamaterials.

At the same time, many thanks to the technician of ME department, Dr. Stephen, who always setup the equipment in time for my experiment. As the experimental work is an essential part of my study. Many thanks to the home-like service provided by ME department and research office of The Hong Kong Polytechnic University.

I am very grateful to everyone in our research group: Dr. LIU Tuo, Mr. CHEN Fei, Dr. GU Zhongming and Ms. GAO He. I truly learned a lot from them. Meanwhile, they were the first people I turned for help when faced with difficulties.

I would like to thank my family members for their selfless support and company. They are always the people who bring me the power, strength and courage. Special thank to my beloved girlfriend, Dr. LIU Chun, for sticking it out with me throughout the endurance trial of the PhD study. Your words continuously push me forward with encouragement in front of challenges. When being with you, I have no exhaustion at all.

TABLE OF CONTENTS

ABSTRACT.....	I
Publications arising from the thesis	III
ACKNOWLEDGEMENTS.....	IV
Chapter 1. Introduction	1
1.1. Metamaterials and metasurfaces	1
<i>1.1.1 A brief history of electro-magnetic metamaterials and metasurfaces</i>	<i>1</i>
<i>1.1.2 Acoustic metamaterials and metasurfaces.....</i>	<i>4</i>
2. Motivation and objectives.....	6
3. Broadband and flexible design of acoustic metasurfaces	7
5. Organization of the thesis	9
Chapter 2. Gradient-pitched helicoid metamaterials	11
2.1 Theory of retrieving effective parameter	11
2.2 Helicoid structure with gradient pitch.....	16
<i>2.2.1 Gradient-indexed (GRIN) effective media of the unit cells.....</i>	<i>16</i>
<i>2.2.2 Acoustic characteristic of the unit cell.....</i>	<i>27</i>
2.3 Narrow-band and broadband focal lens	31
<i>2.3.1 Design</i>	<i>31</i>
<i>2.3.2 Realization by uniform-pitched helicoid metamaterial.....</i>	<i>32</i>
<i>2.3.3 Realization by gradient-pitched helicoid metamaterial.....</i>	<i>33</i>

2.3.4 <i>Experimental setup</i>	40
2.4 Sound amplification by GRIN unit cell	43
2.5 Summary	48
Chapter 3. Flexible design of acoustic metalens.....	51
3.1 Generalization of Snell’s law	51
3.2 Reconfigurable metalens.....	52
3.2.1 <i>Design</i>	52
3.2.2 <i>Realization of the metalens with multi-angle refraction</i>	54
3.2.3 <i>Experimental results</i>	62
3.3 Broadband Quasi Bessel beam launcher.....	66
3.3.1 <i>Design</i>	66
3.3.2 <i>Realization</i>	66
3.3.3. <i>Broadband performance of the unit-cell</i>	69
3.3.4 <i>Experimental results</i>	70
3.4 Summary	75
Chapter 4. Spiraling-structured acoustic metamaterials	77
4.1. Equivalent medium of a tube with a segment of shrunk radius	77
4.2 Construction of spiralling acoustic metamaterials.....	81
4.3 Broadband acoustic wavefront convertor	87
4.4 Summary	92
Chapter 5. Summary and Suggestions for Future Research	94

5.1 Brief summary of the thesis	94
5.2 Suggestions for future research.....	96
References.....	98

Chapter 1. Introduction

1.1. Metamaterials and metasurfaces

1.1.1 A brief history of electro-magnetic metamaterials and metasurfaces

Metamaterials are artificial structures composed of small building blocks and behaves like continuous materials with unconventional effective parameters[1]. The word “meta” is from Greek that means “beyond”. In 1967 a research work by Victor Veselago theoretically discussed negative values of ϵ and μ in electrodynamics, which is the earliest attempt to use negative refractive index. The work was translated to English version in 1968[2]. Due to the limited technology on manufacturing at that time, people could not create such an unconventional material. Until 2000, the negative-indexed material was experimentally realized by a group at UC San Diego, led by David Smith[3]. Fig. 1.1 shows four types of metamaterials divided by their effective parameters in electrodynamics. The realization of “metamaterials” opens the An example of double-negative metamaterial[3].

Fig 1.2 demonstrates the four types of metamaterial divided by the effective permittivity, permeability and refractive index. The natural materials are most in the first quadrant of the $\epsilon - \mu$ system, while the development of metamaterial brings rich diversity to the rest of the quadrants. A typical type is the left-handed materials[4]–[7] in the third quadrant that can support backward propagating waves. Nevertheless, metamaterials are not limited to the signal of the effective parameter, by novel designed unit-cells or constructions, more unconventional phenomena can be realized by metamaterials. In the following the applications of metamaterials will be discussed briefly.

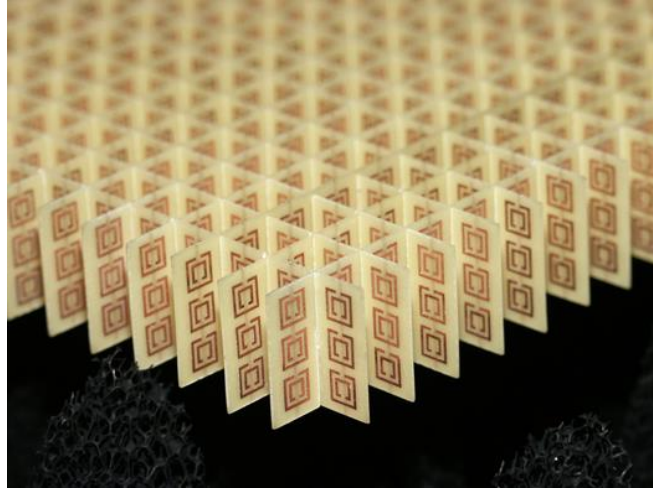


Fig. 1.1. An example of double-negative metamaterial[3].

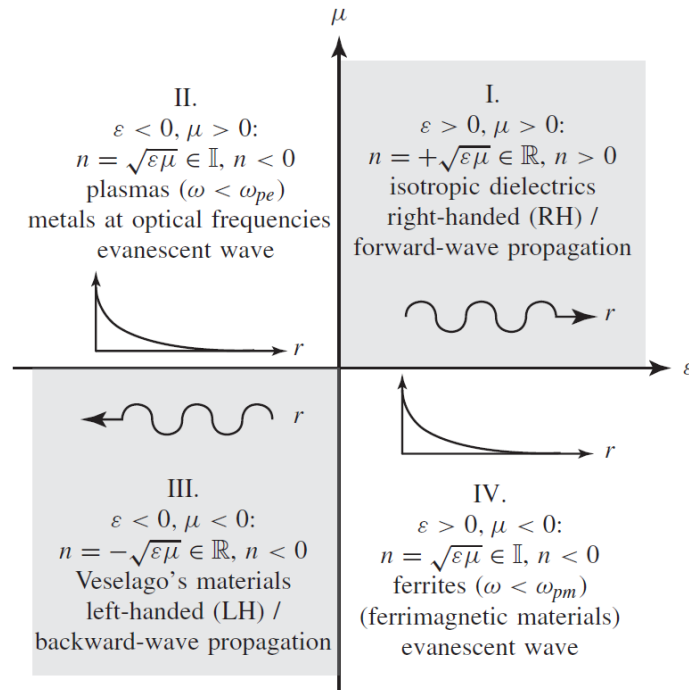


Fig. 1.2. Permittivity-permeability and refractive index diagram[8].

The past two decades witnessed the rapid progress in the field of metamaterials. The optical transformation theory guides the development of related devices, for instance, the invisibility cloaks[9]–[12], polarization splitters[13], wave rotators[13], [14], antennas of Luneburg lenses[15], [16], etc. Metamaterials also help to overcome the diffraction limit, resulting in superlens[17] or magnifying superlens[16, 18] for a better

imaging quality. The study on metamaterials brings numerous applications for radiated- and guided- wave due to its enhanced control on the effective properties of the devices.

Metasurface inherits the “meta” properties of metamaterials; introduces abrupt changes in optical properties[19] to the wave propagation for wavefront modulation[20]–[22], beam formation[23] and wave reshaping[24], etc. The development of metasurface origins from the generalization of laws of reflection and refraction[19], [25]. The generalized laws are:

$$\begin{cases} n_t \sin(\theta_t) - n_i \sin(\theta_i) = \frac{1}{k_0} \frac{d\phi}{dx} \\ \cos(\theta_t) \cos(\varphi_t) = \frac{1}{n_t k_0} \frac{d\phi}{dy} \end{cases} \quad (1-1a)$$

$$\begin{cases} \sin(\theta_r) - \sin(\theta_i) = \frac{1}{n_i k_0} \frac{d\phi}{dx} \\ \cos(\theta_r) \sin(\varphi_r) = \frac{1}{n_i k_0} \frac{d\phi}{dy} \end{cases} \quad (1-1b)$$

where the variables of the symbols are shown in Fig. 1.3.

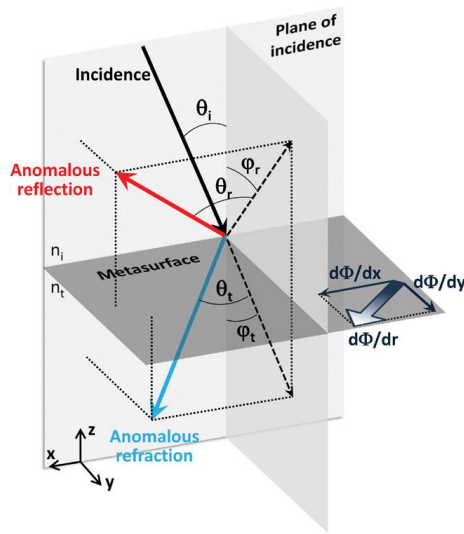


Fig. 1.3 A phase discontinuity on the metasurface leads to anomalous refraction and reflection[26]

1.1.2 Acoustic metamaterials and metasurfaces

Acoustic metamaterial is the counterpart of metamaterials in acoustics, dealing with sound and vibrational waves. Acoustic waves behave like electro-magnetic waves due to the similarity of their govern equations. Generally, the exploration of acoustic metamaterials is similar to that of electro-magnetic metamaterials. The tailored effective parameters make acoustic metamaterials an attractive way for wave control and absorption. The initial of acoustic metamaterial is for sound attenuation by using unit-cells composed of metal cores coated with rubber[27], see Fig.1.4.

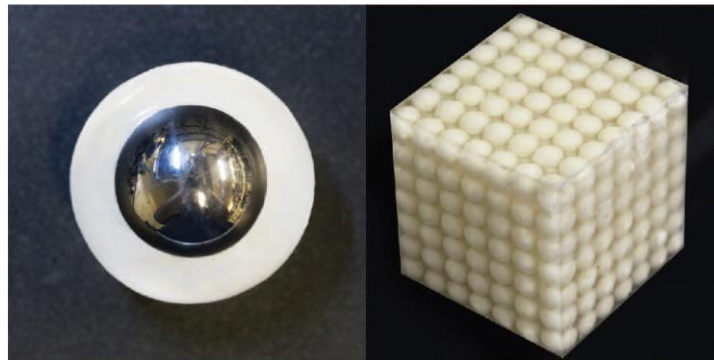


Fig. 1.4 Images of the locally resonant sonic materials' sample. On the left is the structure of a unit-cell and the right-hand side is the periodic structure by the unit cells[27], [28].

The spring-mass model[28] reveals the negativity of the dynamic effective mass. Obviously, it is frequency dependent. Meanwhile, the resonance-based metamaterial is an easy way to realize single- and double- negativity[29]–[34], which make negative parameters being considered for design. Lee et al. firstly demonstrate the double negativity in experiment by overlapping the frequency dispersion of dynamic density and bulk modulus[34]–[36]. This property can be used to create devices to enhance acoustic imaging call acoustic superlens[37]. The doubly negative superlens carries more information because of the evanescent wave components. Notably, the local resonance can also couple evanescent waves to propagating waves by Fabry–Pérot resonance[38], [39]. Thus, the imaging result can break the diffraction limit for a “super

resolution”. The sample is in Fig. 1.5. To have a broad bandwidth and capability for far field imaging, acoustic hyperlens[40]–[43] is achieved that can convert evanescent waves into propagating waves.

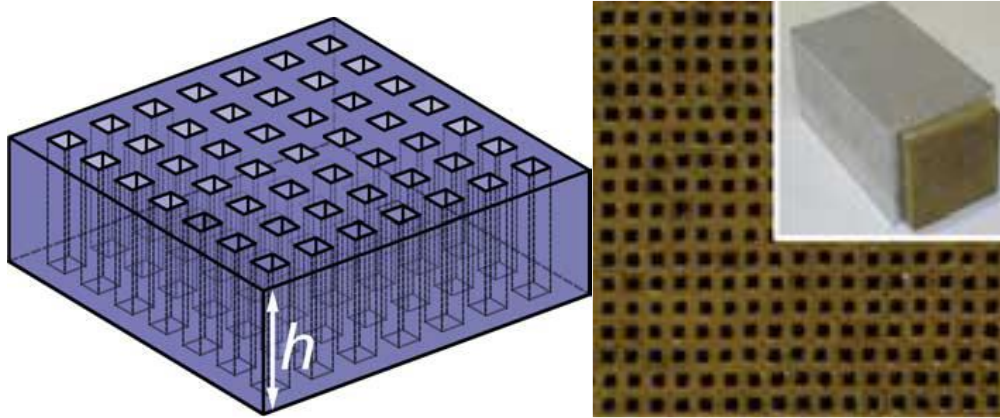


Fig. 1.5 Images of the holey-structured acoustic metamaterial for deep-subwavelength acoustic imaging[39].

Apart from imaging, many other appealing functionalities have also been realized based on acoustic metamaterials. Because the effective properties' distribution relies on the construction of the unit-cells, one can introduce transformation acoustics[44] in theory to obtain required spatial-varying parameters for desired applications. Acoustic cloaking[45]–[47] is a remarkable example. Active acoustic metamaterials[48]–[50] give a way to deal with loss and enhance the practicality. In acoustics, the gain and active components are more readily available than they are in optics, leading to an intensive investigation on parity-time symmetric acoustic metamaterials [51]–[53], such as the novel cloaks and advanced sensors. There are also all-passive parity-time symmetric metamaterials[54] developed to provide more possibilities for passive devices.

In this context, we prefer wavefront steering with a reduced dimension rather than bulky metamaterials because of the long wavelength of sound waves. Once realized, acoustic

metasurface with planar profile is more applicable for practical scenarios. With such sound devices, one can design novel functionalities in wavefront modulation in an unconventional way. Following the generalized laws of refraction and reflection in optics, it is believable to design metasurface in acoustics based on phase engineering[55]. The designed devices can be divided into two parts: one is reflective type and the other is refractive type. The acoustic metasurfaces are always constructed by some typical structures, such as coiling-up space structure[56]–[61], Helmholtz-resonator-like structure[62]–[64] or membrane-type structure[30], [65]–[67], etc. Based on the phase profile retrieved from the desired field, the unit-cells geometry can be determined separately to meet the phase delay on the corresponding position. Previous studies demonstrate various application scenarios, exemplified by sound focusing[57], [68], [69], perfect and ultrathin absorbers[70]–[72], ultrathin Schroeder diffusers[73], and so on. The transmissive type of metasurfaces are similar to their reflective counterparts. Hence the metasurfaces can be designed to change the direction of wave propagation[62], [74]–[76], form various types of beams[77], [78], realized asymmetric transmission[79] or achieve acoustic hologram[80].

2. Motivation and objectives

In section 1, a brief history of the metamaterial has been investigated both in electromagnetic and acoustic branch. These two topics merely in a parallel structure. After an intensive review, acoustic metasurfaces are chosen to be an interested topic of this thesis. With an application-oriented idea, I focus on how to broaden the operating frequency bandwidth of the existing metasurfaces as well as to find out more possibilities to design meta-structures taking advantage of its natural flexibility.

This thesis aims to broaden the operating frequency band of current metamaterials to enhance their practicality, making them applicable for more working conditions.

Due to the complexity of the current design procedure, such as parameter sweeping or optimisation algorithms, to develop more efficient method or more controllable model can make the design strategy more efficiency.

3. Broadband and flexible design of acoustic metasurfaces

There are two reasons that the current metasurfaces suffer from limited bandwidth. First, for those approaches that utilize cavity resonance based structures[62], [74], [81] to generate phase delay, they only work near the resonant frequencies. Secondly, if the high index is introduced by coiling up space[57], [60], [61], the designed metasurfaces are always accompanied by the impedance mismatching and the Fabry–Pérot resonances incurred. The dramatical decrease of the transmission coefficient occurs near to the Fabry–Pérot resonant frequencies. To extend the working frequency range, corrugated surface[82] and circular-holed cube[68] were adopted. They can effectively modulate the reflected acoustic wave, but not suitable for the transmitted wave. In this context, metamaterials with varying geometrical shape[69], [83]–[87] were introduced to improve the spectral performance, as the graded interface between metamaterial and background media can decrease the reflection with a better impedance matching behavior. For some of the design[69], the high index region is restricted by the viscous or structural loss because of the structural complexity. Also, many approaches[85], [88] were in a primary stage, and more experimental investigation is needed. Notably, by ‘compressing the space’ by using helicoid surface[89], a broadband dispersion-free metamaterial can be obtained, and its effective parameters can be adjusted precisely by changing the helical pitch. Former works attempted to make an impedance-matched

layer by using gradient pitch distribution[75], [88], [90] and sound devices with diverse functionalities has been demonstrated with numerical results. However, little systematic investigation has been conducted on the overall reconstruction of the uniform helicity design, especially the theoretical analysis on subsequent benefits in the frequency response of phase delay and transmission efficiency. Also, there lacks the experimental work to evaluate the effect of viscous and thermal loss and demonstrate the broadband sound wavefront modulation with high energy transitive ratio.

The study of the thesis is around helical structured metamaterials which firstly presented by Zhu et al. in 2016 as a dispersion-free slow wave propagation material for phase engineering[89]. The effective indices and dynamic densities are retrieved in this work. An Airy beam was used to show its phase control ability. For the phase engineering on a planar surface, a demonstration also has been presented by Hussein with a title “Generation of acoustic helical wavefronts using metasurfaces”[91]. In this paper, the helicoid describes mathematically by the parametric equation

$$\vec{r}(\rho, t) = \langle x, y, z \rangle = \langle \rho \cos \left[2\pi \int_0^t f(\tau) d\tau \right], \rho \sin \left[2\pi \int_0^t f(\tau) d\tau \right], bt \rangle. \quad (1-2)$$

where ρ is the radius of the helicoid, b is the constant rate of gradual displacement along the middle axis. A metasurface constructed by the helicoid structures convert plane wave to helical wavefront in a circular waveguide. The acoustic metacouplers[88] and gradient-indexed impedance matching layer[90] shows that the gradient variation of the pitch can be an intermediate segment on the interface between two materials. A thoroughly theoretical analysis and experiment investigation is still highly desired. In the following years, the helical structures have also been adopted for the wavefront modulation such as coded metasurface[75], beam splitters. Because the structure of the

helicoid components looks like screw and nut, the related mechanism is also introduced to the tunability of unit cells, resulting in continuously tunable metasurfaces both for transmitted[92] and reflected[93] wavefront modulation. It is worth noted that the research of this thesis also contributed to the development of the gradient helicoid metamaterials by intensively theoretical work and experimental investigation. In this work, I pushed forward the effective media theory of the helicoid metamaterial by proving the equivalence between the gradient helicoid metamaterial and an inhomogeneous media[94].

To make the current acoustic metamaterials more practical, there are two questions for this topic. Is it possible to simplify the design procedure? How to make further efforts to develop the potential of acoustic metasurfaces flexibility? Approaches in the recent years give many attempts to reply those two questions. Taking the position and dimension as the parameters of such kind of gradient-index[95], [96] structures, optimistic algorithms (such as genetic algorithm[97] (GA)) are used to enhance the efficient of the lens both in 2-dimensional and 3-dimensional concentric rings. Some researchers resort to building libraries[98] or making desecrates cells[87] for inverse design.

5. Organization of the thesis

This thesis demonstrates the design of acoustic metamaterials for wavefront modulation with broad bandwidth and better flexibility. Chapter 2 introduces linear distribution to the pitch of the helicoid metamaterial, building a gradient helicoid metamaterial. A broadband focal lens and a broadband sound signal amplifier are constructed to demonstrate the functionalities of the gradient helicoid metamaterial. On the basis of chapter 2, chapter 3 focuses on building more flexible wavefront modulator with

gradient helicoid metamaterial in broad bandwidth. A diffractive metasurface for anomalous refraction has been achieved; its three working modes can be switched between each other by reordering the unit-cells. Chapter 4 demonstrates the practicality of broadband anomalous refraction by using experimentally realized Bessel beam. Based on the accumulation of the previous chapters, a more general theory has been developed in chapter 5 to describe the behavior of the helicoid metamaterial. This chapter establishes the spiralling unit-cells and build connection between the geometrical and acoustic parameters. A broadband wavefront converter has been constructed to demonstrate its performance.

Chapter 2. Gradient-pitched helicoid metamaterials

In this chapter, the effective model of a uniform-pitched helicoid unit cell is first introduced, and then the modeling of the gradient-pitched helicoid metamaterials is discussed. With the gradient effective index, the novel designed unit cell presents its broadband performance through two functionalities, namely, a broadband sound signal amplifier and a broadband focal lens with predictable focal length.

2.1 Theory of retrieving effective parameter

The effective parameter model is based on the dispersion free of the uniform-pitched helical-structured metamaterial.

The mathematical expression for the blades' surface of uniform-pitched helicoid is written as follows:

$$\begin{cases} x = r \sin \theta \\ z = r \cos \theta, \\ y = a \cdot \theta \end{cases} \quad \frac{d}{2} \leq r \leq \frac{D}{2}, \quad \theta_1 \leq \theta \leq \theta_2, \quad (2-1)$$

where d and D are the inner and outer diameters of a unit cell, respectively.

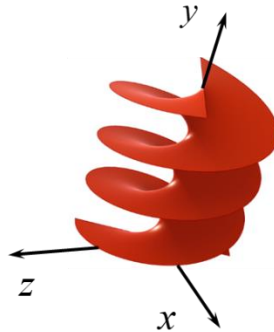


Fig. 2.1 A schematic diagram of a helicoid surface.

The coiled-up space between the blades prolongs the route of wave propagation, resulting in an increased refractive index. Given the uniform distribution of the helical space, the structure is equivalent to a dispersion-free homogeneous medium with slow wave propagation. In this context, the effective parameter of this kind of metamaterial can be retrieved on the basis of the transmission coefficient or transfer-matrix method. The latter one is commonly used for the measurement of acoustic parameters, such as refractive index or impedance.

Fig. 2.2 shows the analogy to an equivalent medium and the transfer-matrix-based four-microphone method[99]. Such technique is used to numerically and experimentally test the complex transmission coefficient and evaluate the transmission loss.

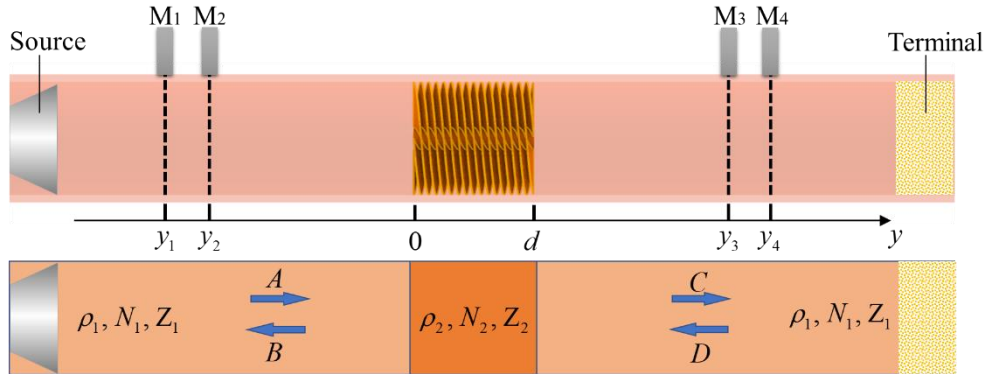


Fig. 2.2 Uniform-pitched helicoid metamaterial and its equivalent medium. A uniformly helical-structured metamaterial of thickness d is positioned to the middle of an impedance tube. Left-hand side is a plane wave source and right-hand side is a terminal with absorption. The helical-structured unit-cell is equivalent to a material whose equivalent density, refractive index and impedance are ρ_2 , N_2 , and Z_2 , respectively. Rest of the parameters with subscript '1' is the acoustic property of the background media. A to D represents the positively and negatively propagating plane wave inside the tube.

In this process, a loudspeaker acts as the source of plane wave. Four microphones positioned at x_1 to x_4 read complex pressure P_1 to P_4 , taking the following forms:

$$P_1 = (Ae^{-jky_1} + Be^{jky_1})e^{j\omega t}, \quad (2-2a)$$

$$P_2 = (Ae^{-jy_2} + Be^{jky_2})e^{j\omega t}, \quad (2-2b)$$

$$P_3 = (Ce^{-jky_3} + De^{jky_3})e^{j\omega t}, \quad (2-2c)$$

$$P_4 = (Ce^{-jky_4} + De^{jky_4})e^{j\omega t}. \quad (2-2d)$$

Eq. 2-2a to d yield positive and negative going complex pressure values at both sides of the measured unit cell, that is,

$$A = \frac{j(P_1e^{jky_2} - P_2e^{jky_1})}{2 \sin k(y_1 - y_2)}, \quad (2-3a)$$

$$B = \frac{j(P_2e^{-jky_1} - P_1e^{-jky_2})}{2 \sin k(y_1 - y_2)}, \quad (2-3b)$$

$$C = \frac{j(P_3e^{jky_4} - P_4e^{jky_3})}{2 \sin k(y_3 - y_4)}, \quad (2-3c)$$

$$D = \frac{j(P_4e^{-jky_3} - P_3e^{-jky_4})}{2 \sin k(y_3 - y_4)}. \quad (2-3d)$$

The transfer matrix connects the sound pressure and normally directional particle velocity between the incident and the transmitted interface, as shown in Fig. 2.2 position $x=0$, and $x=d$. We have

$$\begin{bmatrix} P \\ V \end{bmatrix}_{x=0} = \begin{bmatrix} t_{11} & t_{12} \\ t_{21} & t_{22} \end{bmatrix} \begin{bmatrix} P \\ V \end{bmatrix}_{x=d}. \quad (2-4)$$

Considering the reciprocity and symmetry of the acoustic wave propagation, the following relationship can be obtained:

$$t_{11} = t_{22}, t_{11}t_{22} - t_{12}t_{21} = 1. \quad (2-5)$$

To solve the transfer matrix in Eq. 2-4, variables P and V are required. These variables can be expressed by the positive- and negative-going waves, that is,

$$P|_{x=0} = A + B, \quad (2-6a)$$

$$V|_{x=0} = \frac{A - B}{\rho_0 c}, \quad (2-6b)$$

$$P|_{x=d} = Ce^{-jkd} + De^{jkd}, \quad (2-6c)$$

$$V|_{x=d} = \frac{Ce^{-jkd} - De^{jkd}}{\rho_0 c}. \quad (2-6d)$$

Substituting Eq. (2-5) and (2-6) back into Eq. (2-4), the elements in transfer matrix are

$$t_{11} = \frac{P|_{x=d} V|_{x=d} + P|_{x=0} V|_{x=0}}{M}, \quad (2-7a)$$

$$t_{12} = \frac{P|_{x=0}^2 - P|_{x=d}^2}{M}, \quad (2-7b)$$

$$t_{21} = \frac{V|_{x=0}^2 - P|_{x=d}^2}{M}, \quad (2-7c)$$

$$t_{22} = \frac{P|_{x=d} V|_{x=d} + P|_{x=0} V|_{x=0}}{M}, \quad (2-7d)$$

where $M = P|_{x=0} V|_{x=d} + P|_{x=d} V|_{x=0}$.

Considering the physical background of the normal-incidence transfer matrix for an inhomogeneous embedded middle layer, the elements contain the information of refractive index and impedance, namely, the effective parameter of the helical-structured metamaterial, that is,

$$\begin{bmatrix} t_{11} & t_{12} \\ t_{21} & t_{22} \end{bmatrix} = \begin{bmatrix} \cos(N_{eff}kd) & jZ_{eff} \sin(N_{eff}kd) \\ j \sin(N_{eff}kd) / Z_{eff} & \cos(N_{eff}kd) \end{bmatrix}. \quad (2-8)$$

In this context, the effective refractive index and effective impedance can be evaluated by

$$N_{eff} = \frac{\arccos t_{11}}{kd}, \quad Z_{eff} = \sqrt{\frac{t_{12}}{t_{21}}}. \quad (2-9)$$

A previous study has shown the dispersion-free characteristic of the helical-structured unit cells in a large frequency range[89]. The next section will discuss the acoustic behavior of a gradient-helicoid metamaterial on the basis of the retrieval method in this section. Notably, the parameter-retrieval method mentioned in this chapter for numerical analysis and experimental measurement are all based on this strategy.

2.2 Helicoid structure with gradient pitch

This section demonstrates the characteristics and performance of the gradient-helicoid metamaterial unit cells.

2.2.1 Gradient-indexed (GRIN) effective media of the unit cells

The performance of the helicoid acoustic metamaterial with constant helical pitch decays away from the Fabry–Pérot (F–P) resonance frequencies owing to the impedance mismatch at two ends of the unit cells. To investigate the behavior of the graded helicoid metamaterial over a broad bandwidth and offer a new wavefront modulation capability, I propose a design with linearly pitch distribution. Through this distribution, the impedance matching on the interfaces is improved. The unit element of the proposed helical structure exhibits a large pitch at two ends and a small one in the middle, symmetric about the middle point. The effective impedance of such gradient helical-structured unit cells is no longer uniform along the wave propagation but instead decided by the on-site pitch value.

The geometrical governing equation determines the helicoid shape by controlling the pitch distribution. The helicoid equation is written as follows:

$$x = r \cos \theta, \quad (2-10a)$$

$$z = r \sin \theta, \quad (2-10b)$$

$$y = \int_0^\theta p(\tau) / 2\pi d\tau, \quad (2-10c)$$

where r is the radius that ranges from $d/2$ to $D/2$, and p is the pitch function with respect to the independent variable θ defined as follows:

$$p(\tau) = ae^{b\tau}, \quad (2-11)$$

where a and b are constants to adjust the helicoid shape.

Hence, function y takes the form

$$y = \frac{a}{2\pi b} (e^{b\theta} - 1). \quad (2-12)$$

Considering functions p and z , the linearity is evident:

$$p = 2\pi b \cdot y + a. \quad (2-13)$$

By choosing appropriate values of a and b , one can adjust the shape of the helicoid blades.

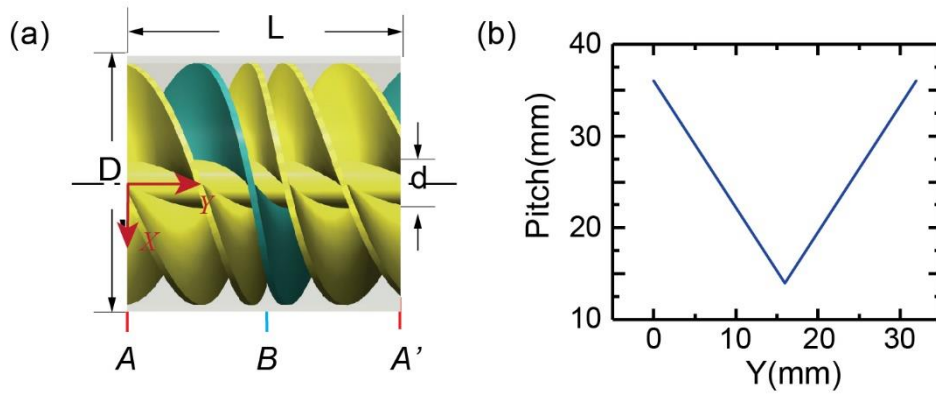


Fig. 2.3 A gradient helicoid metamaterial. (a) Detailed interior design of a helical unit cell with four blades and gradient pitch. In this chapter, the inner diameter, outer diameter, and total length are d (6 mm), D (30 mm), and L (32 mm), respectively. (b) shows the pitch distribution along the Y axis.

The previous investigation reported that the helical-structured metamaterial keeps dispersion-free over spectrum. In this context, the non-dispersive property is assumed

to still work for the GRIN model. The theoretical analysis of this helical-structured metamaterial with a gradient-pitched element design can be resolved with the effective medium model. We obtain the effective refractive index, mass density, and impedance corresponding to a certain pitch through a retrieval method, which is based on the transmission and reflection spectrum through the method in Section 2.1. For an element with a constant diameter and gradient pitch illustrated by Fig. 2.3(b), the effective parameter variations along the wave propagation direction caused by different pitch values are calculated and plotted in Fig. 2.4. The three parameters share the same variation trend that is against the pitch change. From the end to the middle point along the Y axis, the parameters gradually increase with decreasing pitch value and a tight arrangement of the blades.

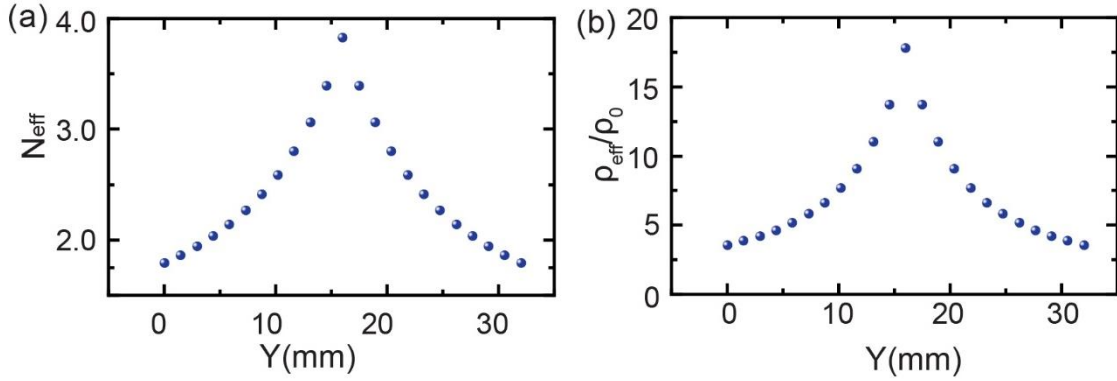


Fig. 2.4 The gradient distribution of effective parameters along the Y axis of the unit cell in Fig. 2.3. (a) and (b) show the effective index and effective dynamic density of the gradient-pitched helicoid unit cell in Fig. 2.3.

The index and dynamic mass density demonstrate a similar trend along the Y axis. The effective impedance of the unit cell has same distribution, that is, with the minimum value at both ends and maximum at the middle of the unit cell. Fig. 2.5 illustrates the variation. This distribution results in an enhanced impedance match at the interface of the metamaterial to the background media and weakens the F–P resonance. Therefore,

the minimum energy-transfer coefficient over spectra is expected to be enhanced, which makes sense for the broadband utilization. In this case, selecting the appropriate pitch distribution enables flexible and ideal inhomogeneous media to be obtained for diverse functionalities and working conditions.

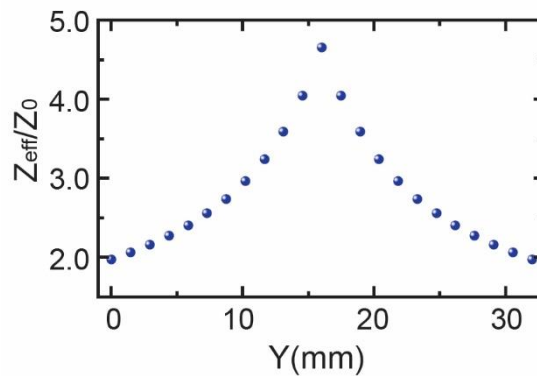


Fig. 2.5 Effective impedance distribution along the Y axis of the unit cell in Fig. 2.3.

The effective parameter of a helical duct with a constant diameter can be the pitch function. On this basis, the behavior of the helical-structured metamaterial elements can be estimated by the effective parameters instead of considering the circuitous geometric space. An inversely proportional function is used in Tables 2.1 and 2.2 to fit the distribution of index and mass density of the cell displayed in Fig. 2.3. This task is initiated to analytically describe the relationship between the effective parameter and the position along the Y axis. As a symmetric profile with respect to the middle of the unit cell, the effective materials can be divided into two layers corresponding to the increasing and decreasing trend of parameters. After the above-mentioned operation, the geometrical model of the graded helicoid metamaterial has been replaced by the effective medium. Fig. 2.6 illustrates the fitting results with excellent agreement to the original data of effective parameters.

Table 2.1 Fitting of the effective refractive index

Interval of y	$0 - \frac{L}{2}$		$\frac{L}{2} - L$	
Expression	$N_{eff} = \frac{1}{\alpha_1 y + \beta_1}$		$N_{eff} = \frac{1}{\alpha_2 y + \beta_2}$	
Independent variable	y			
Dependent variable	N_{eff}			
Method	Trust region method			
Coefficients to be fitted	α_1	β_1	α_2	β_2
Result	-19.66 m^{-1}	0.5804	19.66 m^{-1}	-0.04862
Sum of squares due to error	0.04375		0.04375	

Table 2.2 Fitting of the effective mass density

Interval of y	$0 - \frac{L}{2}$		$\frac{L}{2} - L$	
Expression	$\rho_{eff} = \frac{1}{\mu_1 y + \nu_1}$		$\rho_{eff} = \frac{1}{\mu_2 y + \nu_2}$	
Independent variable	y			
Dependent variable	ρ_{eff}			
Method	Trust region method			
Coefficients to be fitted	μ_1	ν_1	μ_2	ν_2
Result	-10.98	0.2218	10.98	-0.1295
	$\text{kg}^{-1}/\text{m}^2$	$\text{kg}^{-1}/\text{m}^3$	$\text{kg}^{-1}/\text{m}^2$	$\text{kg}^{-1}/\text{m}^3$
Sum of squares due to error	$0.7205 \text{ kg}^2/\text{m}^{-6}$		$0.7205 \text{ kg}^2/\text{m}^{-6}$	

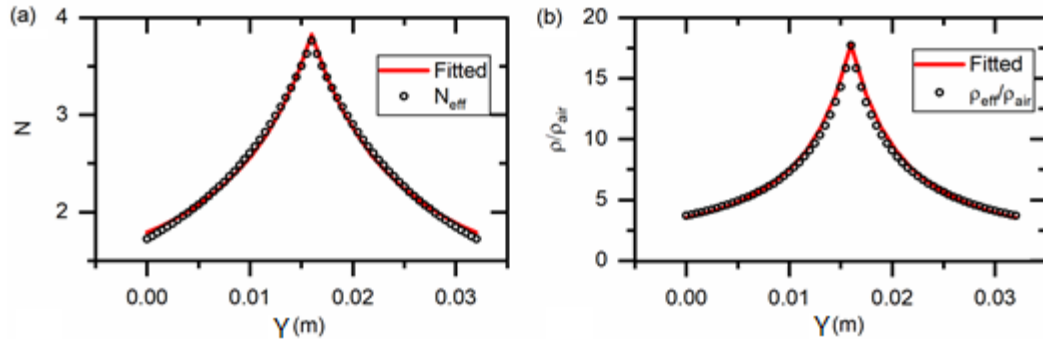


Fig. 2.6 Fitting of the effective parameter: (a) comparison of the fitted index and the original data; (b) comparison of the fitted density and the original data.

The analytical description of the effective medium states that the acoustic behavior can be also analytically predicted. Similar to Fig. 2.2, Fig. 2.7 shows the inhomogeneous medium analogy for the gradient-helicoid metamaterial.

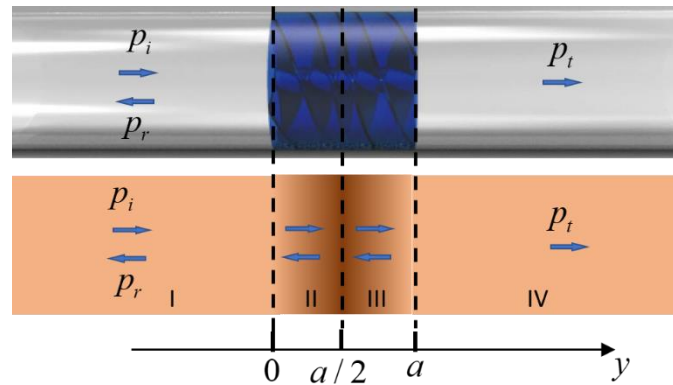


Fig. 2.7 A gradient helicoid metamaterial and its schematic diagram in terms of acoustic index.

Outside the metamaterial region, the 1D monochromatic-wave equation in the background medium (layers I and IV) is (time dependency $e^{j\omega t}$ has been eliminated)

$$\frac{d^2 p(y)}{dy^2} + \left(\frac{\omega}{c}\right)^2 p(y) = 0, \quad (2-14)$$

with the solution expressed as follows:

$$p(x) = \Psi_1^1 e^{-jky} + \Psi_1^2 e^{jky}, \quad (2-15)$$

where Ψ_1^1 and Ψ_1^2 are constants, which can be determined by the boundary conditions.

For the particle velocity along the propagation direction, we have

$$\rho \frac{\partial v}{\partial t} = -\frac{\partial p}{\partial y}, \quad (2-16)$$

and thus

$$v_I(x) = \Psi_I^1 \frac{ke^{-jky}}{\omega\rho_0} - \Psi_I^2 \frac{ke^{jky}}{\omega\rho_0}. \quad (2-17)$$

The wave equation of the inhomogeneous media in layers II and III is as follows:

$$\frac{d^2 p_1(y)}{dy^2} + \left(\frac{\omega}{c} n_{eff}(y) \right)^2 p_1(y) - \left(\frac{d \ln \rho_{eff}(y)}{dy} \right) \frac{d}{dy} p_1(y) = 0, \quad (2-18)$$

where $n_{eff}(y)$ and $\rho_{eff}(y)$ are the space-dependent variables that can be expressed as follows:

$$n_{eff} = \begin{cases} \frac{1}{\alpha_1 y + \beta_1}, & 0 \leq y \leq L/2 \\ \frac{1}{\alpha_2 y + \beta_2}, & L/2 < y \leq L \end{cases}, \quad \rho_{eff} = \begin{cases} \frac{1}{\mu_1 y + \nu_1}, & 0 \leq y \leq L/2 \\ \frac{1}{\mu_2 y + \nu_2}, & L/2 < y \leq L \end{cases}, \quad (2-19)$$

where α_i , β_i , μ_i , and ν_i ($i=1,2$) are the coefficients obtained by curve fitting in Tables 1 and 2.

Considering the complexity of the mentioned inhomogeneous equation, I resort to the symbolic calculation of computer software. The solution of Eq. (2-18) can be written as

$$\begin{aligned}
p_{II}(x) &= \Psi_{II}^1 F([n_1, n_2], d, z) \cdot (\alpha y + \beta)^{\frac{1}{2} \frac{\sqrt{\alpha^2 c^2 - 4\omega^2} - c\alpha}{c\alpha}} + \\
&\Psi_{II}^2 F([n_1', n_2'], d', z') \cdot (\alpha y + \beta)^{\frac{1}{2} \frac{\sqrt{\alpha^2 c^2 - 4\omega^2} + c\alpha}{c\alpha}} \\
&= \Psi_{II}^1 \Lambda(y) + \Psi_{II}^2 \Theta(y)
\end{aligned}$$

where $F([n_1, n_2], d, z)$ is the hypergeometric function which has the form

$$F([n_1, n_2], d, z) = \sum_{k=0}^{\infty} \frac{z^k \Gamma(n_1 + k) \Gamma(n_2 + k) \Gamma(d)}{k! \Gamma(n_1) \Gamma(n_2) \Gamma(d + k)}.$$

Meanwhile, Ψ_{II}^1 and Ψ_{II}^2 are constants for the two linearly independent solutions denoted by $\Lambda(x)$ and $\Theta(x)$. For details,

$$\begin{aligned}
n_1 &= -\frac{1}{2} \frac{\sqrt{\alpha^2 c^2 - 4\omega^2} - 2j\omega - c\alpha}{c\alpha}, n_2 = -\frac{1}{2} \frac{\sqrt{\alpha^2 c^2 - 4\omega^2} + 2j\omega - c\alpha}{c\alpha} \\
d &= \frac{-\sqrt{\alpha^2 c^2 - 4\omega^2} + c\alpha}{c\alpha}, z = \frac{(\alpha y + \beta)\mu}{-\alpha\nu + \beta\mu} \\
n_1' &= -\frac{1}{2} \frac{\sqrt{\alpha^2 c^2 - 4\omega^2} - 2j\omega + c\alpha}{c\alpha}, n_2' = -\frac{1}{2} \frac{\sqrt{\alpha^2 c^2 - 4\omega^2} + 2j\omega + c\alpha}{c\alpha} \\
d' &= \frac{\sqrt{\alpha^2 c^2 - 4\omega^2} + c\alpha}{c\alpha}, z' = \frac{(\alpha y + \beta)\mu}{-\alpha\nu + \beta\mu}
\end{aligned}$$

Following the property of hypergeometric functions, as two general solutions of the inhomogeneous equation, $\Lambda(y)$ and $\Theta(y)$ are linearly independent.

To ensure correctness, we put $\Lambda(y)$ and $\Theta(y)$ back in to

$$D = \frac{d^2 p_1(y)}{dy^2} + \left(\frac{\omega}{c} n_{eff}(y) \right)^2 p_1(y) - \left(\frac{d \ln \rho_{eff}(y)}{dy} \right) \frac{d}{dy} p_1(y)$$

and D has been calculated being 0. Furthermore, the good agreement of the theory and simulation result shows the rationality of the derivation.

The solution of Eq. (2-18) has the form

$$p_{II}(x) = \Psi_{II}^1 \Lambda(y) + \Psi_{II}^2 \Theta(y), \quad (2-20)$$

where Ψ_{II}^1 and Ψ_{II}^2 are constants for the two linearly independent solutions denoted by $\Lambda(y)$ and $\Theta(y)$. The details of the solution are presented in the Appendix. The following particle velocity in layer II is obtained by combining Eq. (2-16) and (2-20)

$$v_{II}(y) = \Psi_{II}^1 \frac{j}{\omega \rho} \frac{d\Lambda(y)}{dy} + \Psi_{II}^2 \frac{j}{\omega \rho} \frac{d\Theta(y)}{dy}. \quad (2-21)$$

The sound pressure and particle velocity in layer III have the same form as that in layer II, but the α , β , ν , and μ values differ. The independent solution can be denoted by $\Lambda'(y)$ and $\Theta'(y)$. With the continuity of sound pressure and normal particle velocity at the interfaces, we can obtain the following relationship for the background and effective medium layers.

$$\begin{cases} p_I(0) = p_{II}(0) \\ v_I(0) = v_{II}(0) \end{cases}, \quad \begin{cases} p_{II}\left(\frac{a}{2}\right) = p_{III}\left(\frac{a}{2}\right) \\ v_{II}\left(\frac{a}{2}\right) = v_{III}\left(\frac{a}{2}\right) \end{cases}, \quad \begin{cases} p_{III}(a) = p_{IV}(a) \\ v_{III}(a) = v_{IV}(a) \end{cases} \quad (2-22)$$

The following relationship between layers I and IV is obtained by changing Eq.

(2-22) to the matrix form and eliminating the middle term:

$$\mathbf{T} = \mathbf{T}_{II}|_{y=a} \cdot \mathbf{T}_{II}|_{y=\frac{a}{2}}^{-1} \cdot \mathbf{T}_I|_{y=\frac{a}{2}} \cdot \mathbf{T}_I|_{y=0}^{-1} \cdot \mathbf{M}|_{y=0}. \quad (2-23)$$

In Eq. (2-23),

$$\mathbf{T}_I = \begin{pmatrix} \Lambda(y) & \Theta(y) \\ \frac{j}{\omega\rho(y)} \frac{d\Lambda(y)}{dy} & \frac{j}{\omega\rho(y)} \frac{d\Theta(y)}{dy} \end{pmatrix}, \mathbf{T}_{II} = \begin{pmatrix} \Lambda'(y) & \Theta'(y) \\ \frac{j}{\omega\rho(y)} \frac{d\Lambda'(y)}{dy} & \frac{j}{\omega\rho(y)} \frac{d\Theta'(y)}{dy} \end{pmatrix},$$

$$\mathbf{M} = \begin{pmatrix} e^{-jky} & e^{jky} \\ \frac{ke^{-jky}}{\omega\rho_0} & \frac{ke^{jky}}{\omega\rho_0} \end{pmatrix}.$$

Based on the continuity of sound pressure and normal particle velocity, the relationship between the pressure p_i of incidence and transmission p_t is expressed as follows:

$$\mathbf{T} \begin{bmatrix} p_i \\ p_r \end{bmatrix} = p_t e^{-jkL} \begin{bmatrix} 1 \\ \frac{k}{\omega\rho_0} \end{bmatrix}, \mathbf{T}^{-1} = \begin{bmatrix} t_{inv11} & t_{inv12} \\ t_{inv21} & t_{inv22} \end{bmatrix}. \quad (2-24)$$

where k and ω are the wave number and angular frequency of the plane wave, respectively; and ρ_0 is the mass density of air. In this case, the overall complex transmission coefficient of sound pressure t_p is derived as follows:

$$t_p = \frac{e^{jkL}}{t_{inv11} + \frac{k}{\rho_0} \frac{1}{t_{inv12}}}. \quad (2-25)$$

The small difference between the real structure and the effective model should be considered. The effective model can be slightly shorter than the length of the blade region (32 mm) because of the large pitch of helicity at both ends of the cells. For the numerical calculation and simulation model with an effective parameter, we cut 2 mm at both ends for accurate results.

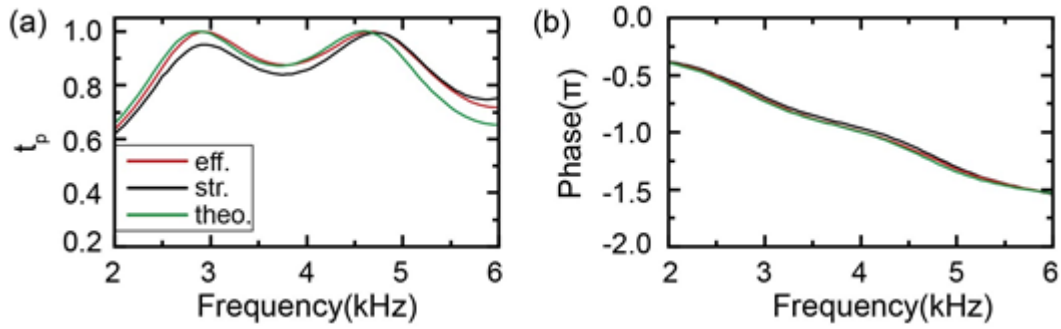


Fig. 2.8 Calculated performance of an element. (a) Transmission spectrum of normal incident plane waves crosses the unit cell. (b) Corresponding phase spectrum response. (a) and (b) share the same legend in (a). Notes of legend: *eff.*—simulation results by using effective media, *str.*—simulation by using the helicoid model, and *theo.* —numerical results corresponding to the theoretical analysis.

The calculated sound pressure transmission and phase delay through the gradient index unit cell are shown in Fig. 2.8. The curve in Fig. 2.8(a) clearly shows the transmission coefficient higher than 80% over the frequency range. The phase delay shows a smooth variation with a gentle slope over the studied frequency range. This outcome is attributed to the gradient index along the propagation direction that weakens the strong dispersion of phase shift caused by specific F–P resonance. With such a smooth curve, controlling the phase delay for phase engineering within the whole wide frequency range of interests is easy and practical.

The good agreement of three groups of results in Fig. 2.8 indicates the feasibility of the effective medium model and the theoretical analysis. The small difference of transmission coefficient of sound pressure may come from the round-off error of the numerical computation and thickness of the structure’s blades. The illustration of the phase delay [Fig. 2.8(b)] shows that a slight shift can be neglected. On one hand, the result shows the validity of the inhomogeneous medium model to replace the real structure. Thus, the designed metamaterial with air-like acoustic properties has relatively high stiffness, which can be used as inhomogeneous sound media. On the

other hand, the conformity guarantees the ‘inverse design’ from the required material parameters’ distribution to the related helical structure. This property remains a huge potential for the flexible design of acoustic metamaterial. The computation above is in a lossless condition. The influence of viscous and thermal loss has been evaluated through an experiment in the following section.

2.2.2 Acoustic characteristic of the unit cell

In this part, the experimental results are illustrated to show the performance and characteristics of the graded helicoid metamaterial.

The performance of the newly designed helical-structured acoustic metamaterial unit cell with gradient pitch has been experimentally measured inside an impedance tube using the four-microphone two-load method, as shown in Fig. 2.9. The samples were manufactured by 3D printing. The huge impedance mismatch between the photopolymer (Somos GP Plus) material we used to fabricate the sample and air makes it possible for us to regard it as rigid in theory model. We performed time- and frequency-related experiments.

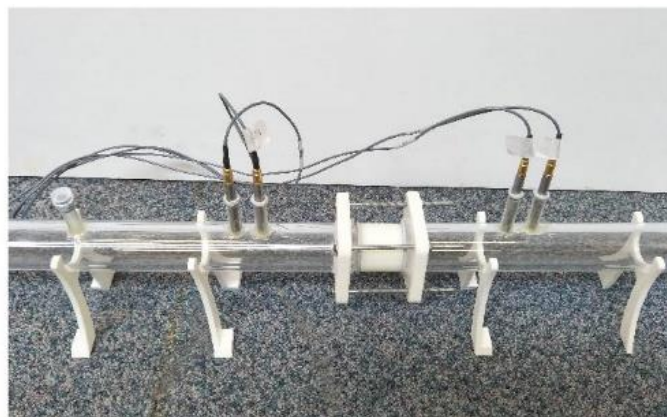


Fig. 2.9 Setup of the lab-made impedance tube. The white-colored cell is fixed in the middle by two flanges. Four microphones are positioned at both sides of the sample.

A short pulse is generated and sent inside the impedance tube to demonstrate that the new gradient-pitched helical-structured design still possesses the sound deceleration function. The recorded transmission signals with and without the metamaterial sample are shown in Fig. 2.10. The sound signal is further delayed by approximately 1.19×10^{-4} s by adding the metamaterial unit cell. The time delay functionality for the signal transmission has been verified.

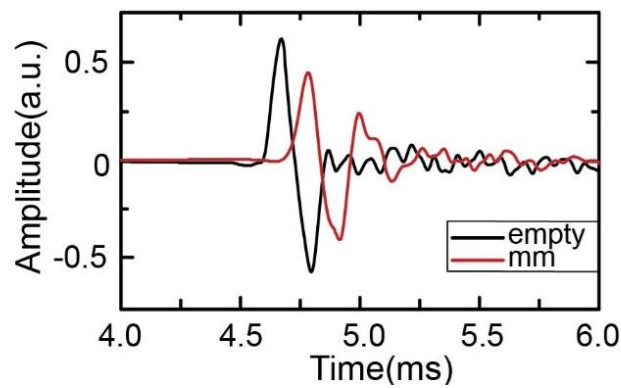


Fig. 2.10 Delay of the pulse sound signal introduced by the gradient-pitched helical-structured element.

The uniform-pitched distribution to the graded model demonstrates that the impedance mismatch has been weakened, so the F–P resonance is related to the reflection at interfaces. The difference can be observed by the comparison of transmission spectrum between elements with constant and gradient pitches. Fig. 2.11(a) shows the experimentally measured spectral transmission performance. The transmission coefficient of the uniform pitched model violently changes caused by relatively pure F–P resonance mode. The 3-dB half-power bandwidth is rather narrow (approximately 0.52 kHz). As shown in the blue curve, the transmission through the gradient-pitch unit cell remains at high values close to unity over a wide frequency range. This finding is in good agreement with the prediction from the transfer-matrix method. The 3-dB half-power band is now 2.6 kHz wide, covering from 2.68 kHz to 5.28 kHz, about one octave.

Such extraordinary sound pressure transmission of the gradient-pitched model over spectrum can be attributed to two physical mechanisms: enhanced impedance matching with the background medium at two ends of the unit cell because of the larger pitch there; and the gradient index profiles that can bridge additional sound energy to counter the effects of specific F–P resonance mode. Fig. 2.11(b) demonstrates the measured phase shift of the two unit-cells. Although the gradient-pitched unit cell shows a smooth phase delay curve without a notable inflection point in the 3-dB band, the phase shift offered by the uniform-pitched unit cell fluctuates around the resonant frequency at 4 kHz. This experiment shows two advantages after eliminating the F-P resonance. On the one hand, instead of periodic valley on the transmission spectrum, the gradient helical structures' response pulls up the valleys and lead to a broadened operating frequency bandwidth. On the other hand, with weak resonance, the phase shift becomes gentle and smooth. That contributes to a stable frequency response for broadband utilizations.

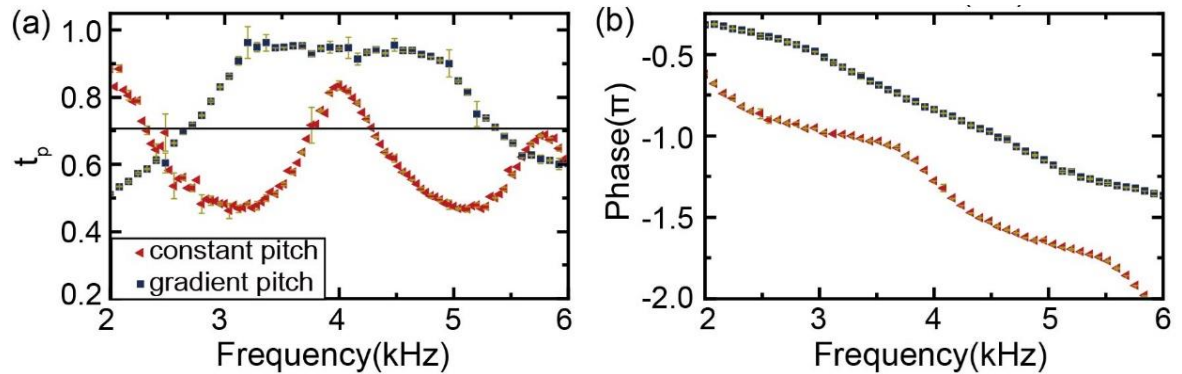


Fig. 2.11 (a) Sound pressure transmission coefficient of a uniform-pitched and gradient pitched element. (b) Phase shift spectra of a uniform-pitched and gradient pitched element. The leading pitch for the uniform-pithed element is 20 mm, and the pitch distribution for the gradient pitched unit cell is the same as that in Fig. 2.3.

The previous work pointed out the dispersion-free property of the uniform-pitched element. By contrast, the dispersion property of the gradient-pitched model is yet to be

experimentally studied. We calculated the spectra of energy transmission and reflection to sufficiently evaluate the characteristic of the helicoid metamaterial. Thus, the viscous and thermal loss of the element can be obtained according to the following relationship:

$$TL = 1 - t_I - r_I, \quad (2-26)$$

where TL is the energy loss; and t_I and r_I are the transmission and reflection coefficients of the energy, respectively. The thermal and viscous loss is kept at a low level over the spectrum [Fig. 2.12(a)]. By contrast, the energy loss of a uniform-pitched element is large near the resonance frequency. The small loss can be also further demonstrated by the effective refractive index. With regard to the gradient distribution of the helical pitch, retrieval of effective parameters cannot be straightforward. However, we can measure the average value of the effective refractive index by taking it as a homogeneous medium. The real part of the index in Fig. 2.12(b) shows the dispersion-free property of the graded helical duct over the spectrum. The imaginary part—the attenuation coefficient—is near zero and remains flat during the calculated frequency range. Hence, the gradient-pitched helical structure can be reasonably described by a lossless model.

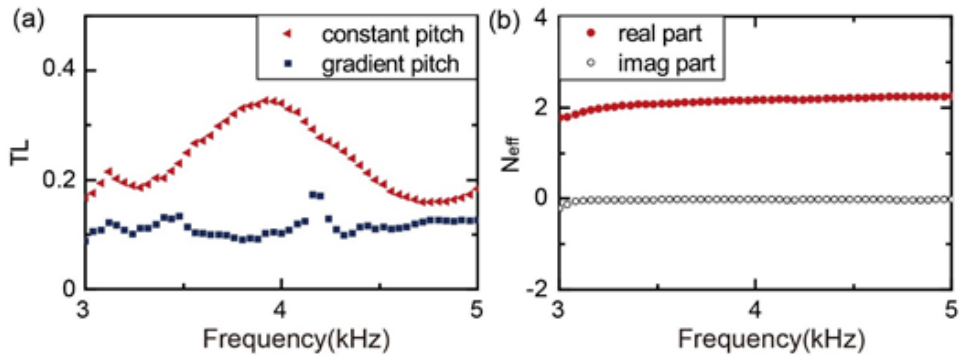


Fig. 2.12 Energy loss and effective index. (a) Measured viscous and thermal loss of uniform and graded helicoid cell. (b) Measured average refractive index of the graded helicoid cell.

2.3 Narrow-band and broadband focal lens

In this section, a flat focal lens, which works in a wide frequency range, has been realized. The lens characteristic indicates that the position of the focal spot at the different operating frequency is calculated and verified by experiment. The focal lens by uniform-pitched helicoid metamaterials has been designed as a control group to demonstrate the broadband performance of the gradient-helicoid metamaterial.

2.3.1 Design

The Huygens principle states that the phase lead-and-lag of the point source array will create the shape of the wave front with an envelope. Fig. 2.13 shows the position of a unit cell and focal spot f . The gradual radiation means that a unit cell can be regarded as a point source without coupling between the neighbors.

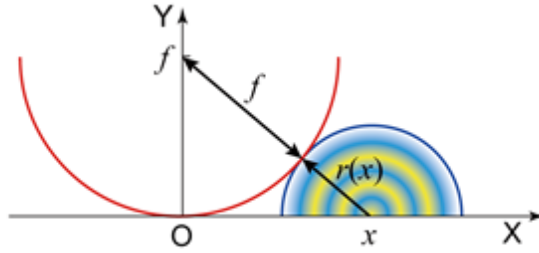


Fig. 2.13 Geometric relationship between focal length and the wavefront of a point source at position x .

The geometrical relationship illustrated in Fig. 2.13 should be satisfied with the following equation to design a focal lens for a normal incident-transmitted plane wave

$$\varphi(x) = \frac{2\pi f}{c} \left(\sqrt{x^2 + F^2} - F \right). \quad (2-27)$$

Eq. (2-27) provides the required phase adjustment distribution along the surface of the flat focusing lens, where φ denotes the phase delay at any specific location x , f is the

operating frequency, c is the sound speed in the air (343.2 m/s^{-1}), and F is the focal length.

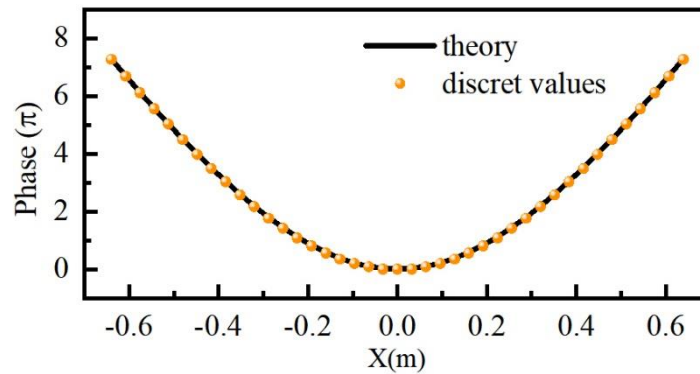


Fig. 2.14 Phase profile of the designed focal lens at 4000Hz. Dots represent the phase of each unit cell at the corresponding positions, and the black line is the theoretically designed phase profile at 4 kHz by Eq. (2-23). The focal length F is selected as 0.5 m without loss of generality.

2.3.2 Realization by uniform-pitched helicoid metamaterial

Before designing the meta-lens by using a gradient-pitched helicoid metamaterial, a meta-lens is realized by using uniform pitched helicoid metamaterials as a control group. Forty-one unit cells are used to construct the meta-lens. The amount of the unit cell is the same as the discrete point in Fig. 2.14. With a working frequency of 4000 Hz, the phase delay of a single unit cell is adjusted by changing the pitch. The length of unit-cells are all fixed at 20 mm. The outer and inner radii are 30 and 6 mm, respectively.

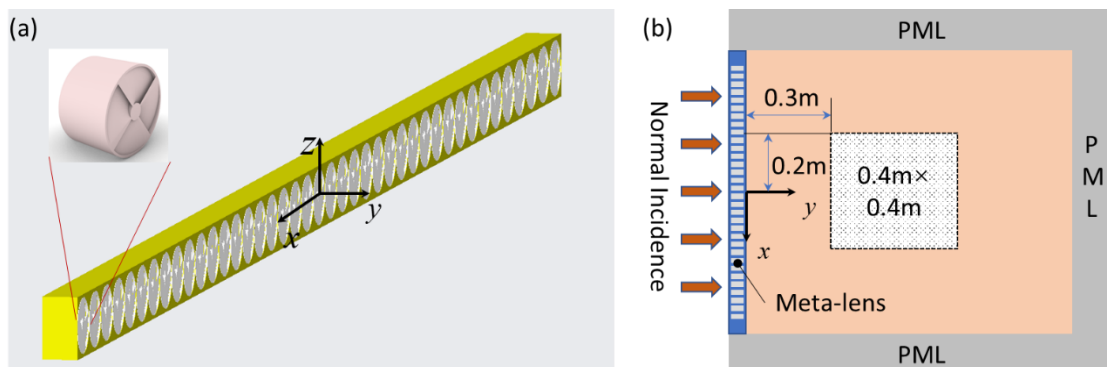


Fig. 2.15 Setup of simulation and its tested region. (a) shows the assembly of the flat meta-lens. The lens is constructed by embedding forty-one cylinder unit-cells into a frame with holes. (b)

illustrates the simulation environment. The data collection is in the $0.4\text{ m} \times 0.4\text{ m}$ region near the position of focal spot.

The calculation result shows a focal spot at the designed operating frequency of 4000 Hz. When the frequencies are set to 3500 and 4500 Hz, the intensity pattern failed to have a focal spot. This finding shows that the uniform-pitched helicoid metamaterial is limited in frequency domain. When the working frequency shifted from the designed frequency, the performance dramatically decreases. Two reasons lead to such results. First, the uniform pitched unit cell has a strong F–P resonance. Hence, the transmission coefficient of the working frequency far from the resonant frequency is much lower than the peak values. Second, the phase delay is influenced by the resonance and lost the required distribution for other frequencies. A gradient pitch for the existing design should be introduced to determine the issue of impedance mismatching and broaden the cell band, which will be discussed in Section 2.3.3.

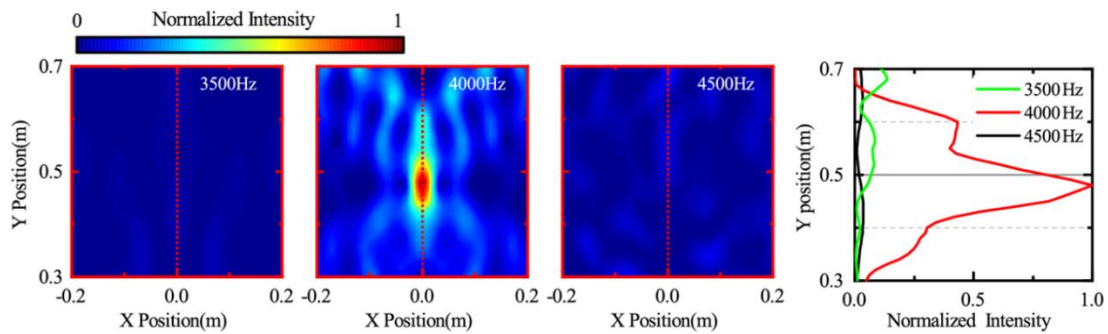


Fig. 2.16 Intensity pattern of the tested focusing region for three frequencies. The right-side line chart shows the sound intensity distribution along the cross-sectional line, dotted in the intensity pattern.

2.3.3 Realization by gradient-pitched helicoid metamaterial

The new helical-structured acoustic metamaterial with gradient pitch offers extraordinary sound transmission and smooth phase adjustment within a wide frequency range. Realizing a series of phase delays by appropriate pitch distributions is

now possible, without the fear of suffering from the lower transmission. With the smooth phase shift, the difference in phase delay between any two unit-cells remains invariable over the spectrum. Taking advantage of this unique characteristic, we design and fabricate a thin flat focal lens with an array of new gradient-pitched helical-structured acoustic metamaterial unit cells. The lens thickness is less than half of the smallest wavelength.

This continuous phase profile is further discretized into 41 segments. Accordingly, the whole lens can be constructed with 41 individual unit cells embedded in a holding frame, as exhibited in Fig. 2.18. The required phase modulation at each of the forty-one unit-cells is achieved by adjusting the leading pitch. We subsequently calculate the phase profiles for three different frequencies, namely, 3.5, 4, and 4.5 kHz, and present the discretization results in Fig. 2.17. The two elements can keep a relatively constant phase difference over the spectrum, which forms a uniform phase profile, because of the smooth phase delay of the elements in terms of frequency. This condition paves the way towards realizing a broadband sound focusing with one set of gradient-pitched helical-structured acoustic metamaterial unit cell array. Considering the consistency of the phase distribution in terms of frequency, the position of the focal point is frequency dependent and can be predicted. In Eq. (2-27), we can obtain the focal length at different frequencies with curve fitting method by taking F as the parameter to be fitted, and x and $\varphi(x)$ as the independent and dependent variables, respectively. In the fitting process, we first have the following expression:

$$y = \frac{c}{2\pi f} \varphi(x) = \sqrt{x^2 + F^2} - F, \quad (2-28)$$

where y is the wavefront based on the phase profile. The focal length F can be obtained by using the trust region fitting method. As shown in Fig. 2.18, the radius of the output wavefront envelope, that is, the focal length, will increase with frequency (i.e., 0.40 m at 3.5 kHz, 0.50 m at 4 kHz, and 0.58 m at 4.5 kHz).

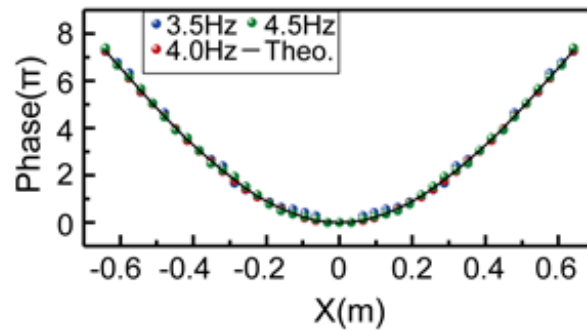


Fig. 2.17 Phase profile requirement of the flat focal lens for different sound frequencies. The dots represent the phase of each unit cell at the corresponding positions. The black line is the theoretically designed phase profile at 4 kHz by Eq. (2-27).

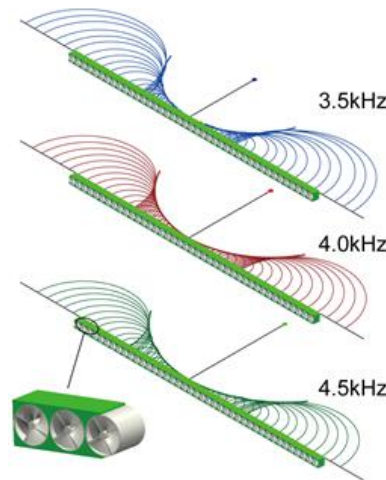


Fig. 2.18 Focal point for three operating frequencies. The semicircle is the wavefront from each unit cell. The envelope curve obtained by fitting method that appears in bold is the focusing wavefront. At the bottom left corner of (c), the structure of the flat lens is partially magnified. Forty-one cells are embedded in the holey frame whose total width is 1.312 m.

The unit cells are all manufactured by 3D printing with a photopolymer. Fig. 2.19 shows the white-colored cylinder unit cells that have similar pitches at both ends while diverse pitch values in the middle. Hence, the impedance in the lens direction remains nearly uniform to match the air's impedance.



Fig. 2.19 Gradient helicoid unit cells with a uniform height of 32 mm.

We conducted simulation and experiments to validate the thin flat focal lens design. The sound intensity patterns for three separated frequencies, namely, 3.5, 4, and 4.5 kHz, are extracted and plotted in Fig. 2.20. We measured only the region around the focal point, marked with red boxes in Figs. 2.20(a)– 2.20(c) and illustrated by Figs. 2.20(d)– 2.20(f), because of the limited range of our sound mapping system. The well-matched simulation and experimental results show that the thin flat lens can focus incident acoustic waves of different frequencies covering 1/3 octave coverage. The shape of the focal spot is clear for all three frequencies. The sound intensity at the focal point also remains on the same level for three frequencies, indicating similar high transmission over the spectrum. Simulations for incident acoustic waves with frequencies different from the aforementioned ones are also conducted. In all cases, the similar extraordinary sound transmission and focusing effects can be clearly observed. Refer to Appendix C for the predicted behavior and pressure field. The high energy transmission coefficient in the whole operating frequency range is witnessed by almost the same maximum intensity under 3.5, 4, and 4.5 kHz, as shown in Fig. 2.20(g)–(i). In the wave travelling direction, the intensity sharply drops after passing through a focal spot. This behavior is of great significance in contributing to the energy concentration. The peak position exhibits that the experimentally determined focal lengths are 0.36, 0.47, and 0.56 m for the corresponding frequency in Fig. 2.20(g)–(i). The small difference between the theoretical and experimental results of the focal length indicates the good controllability and high accuracy of the lens. The error of the experiment may

come from the slight shaking of the microphone during the test process. The intensity gradient near the focal spot is particularly steep that a slight shaking may lead to a large error.

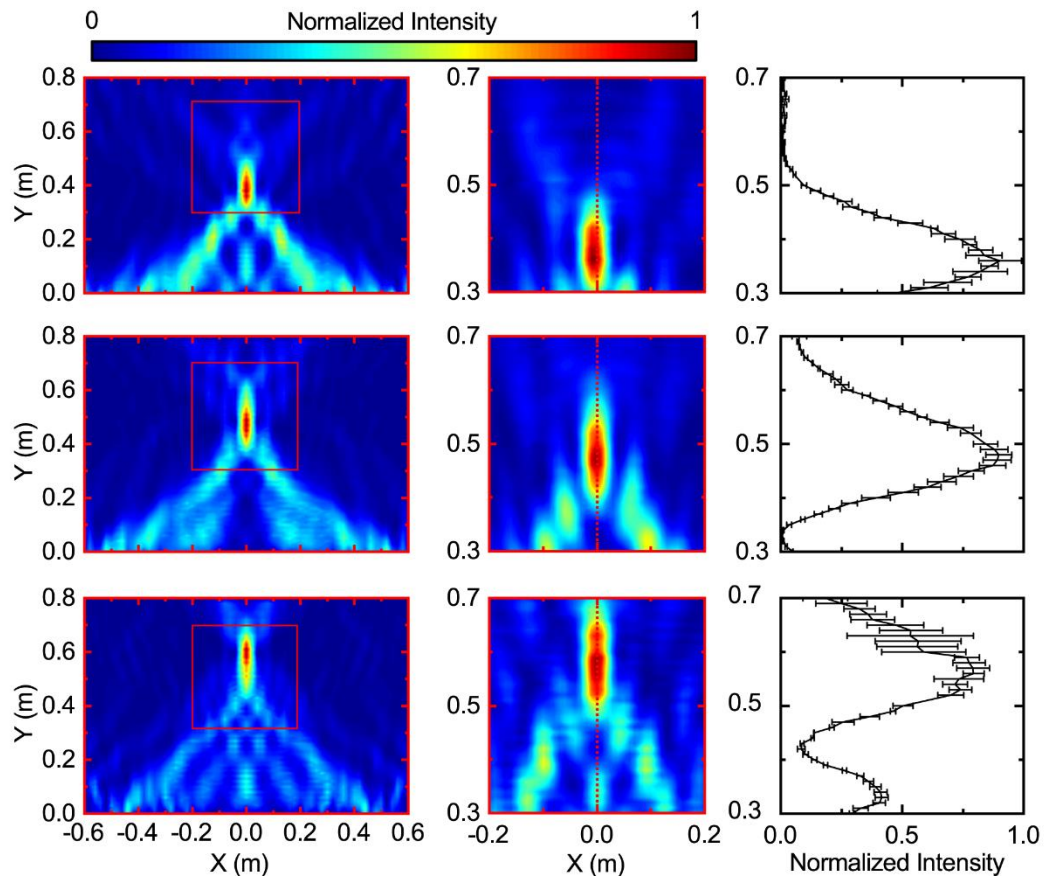


Fig. 2.20 Intensity field of broadband sound focusing. (a)–(c) Simulated sound intensity field distribution at 3.5, 4, and 4.5 kHz, respectively. The red blocks inside mark the scanning area adopted in the experiments. (d), (e), and (f) are the experimentally measured sound intensity field distribution at 3.5, 4, and 4.5 kHz, respectively. (g), (h), and (i) are the transverse cross-sectional intensity distribution along the Y axis (the red dash lines) at $x=0$ for 3.5, 4, and 4.5 kHz, respectively.

The pressure pattern of simulation and experiment has been plotted in Fig. 2.21 to further demonstrate the capability. On one hand, the bent wavefronts are clearly illustrated. On the other hand, the focal spot moves further along with the frequency increase, which is in good agreement with the theoretical analysis.

The available frequency band of the designed focal lens ranges from approximately 3.5 kHz to 4.5 kHz, which is not limited to the three separated frequencies demonstrated in the main text. Simulations at other frequencies have been conducted to intensively verify the flat lens' performance. The simulated acoustic intensity fields in Fig. 2.22 shows that the lens has an ideal and uniform performance for sound focusing over a considerable bandwidth.

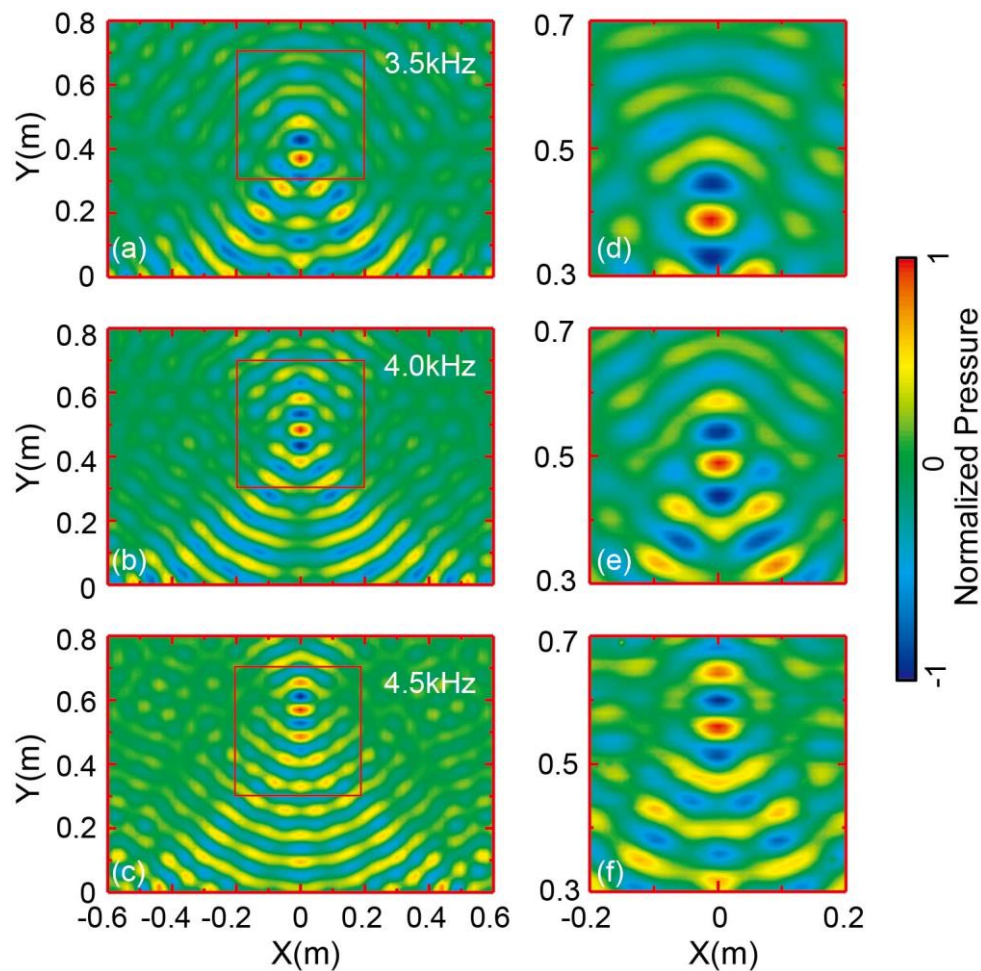


Fig. 2.21 Comparison of the measured and simulated acoustic pressure fields. (a)–(c) and (d)–(f) are the simulation and experimental results, respectively. The red boxes in the left sub-panels denote the scanned area.

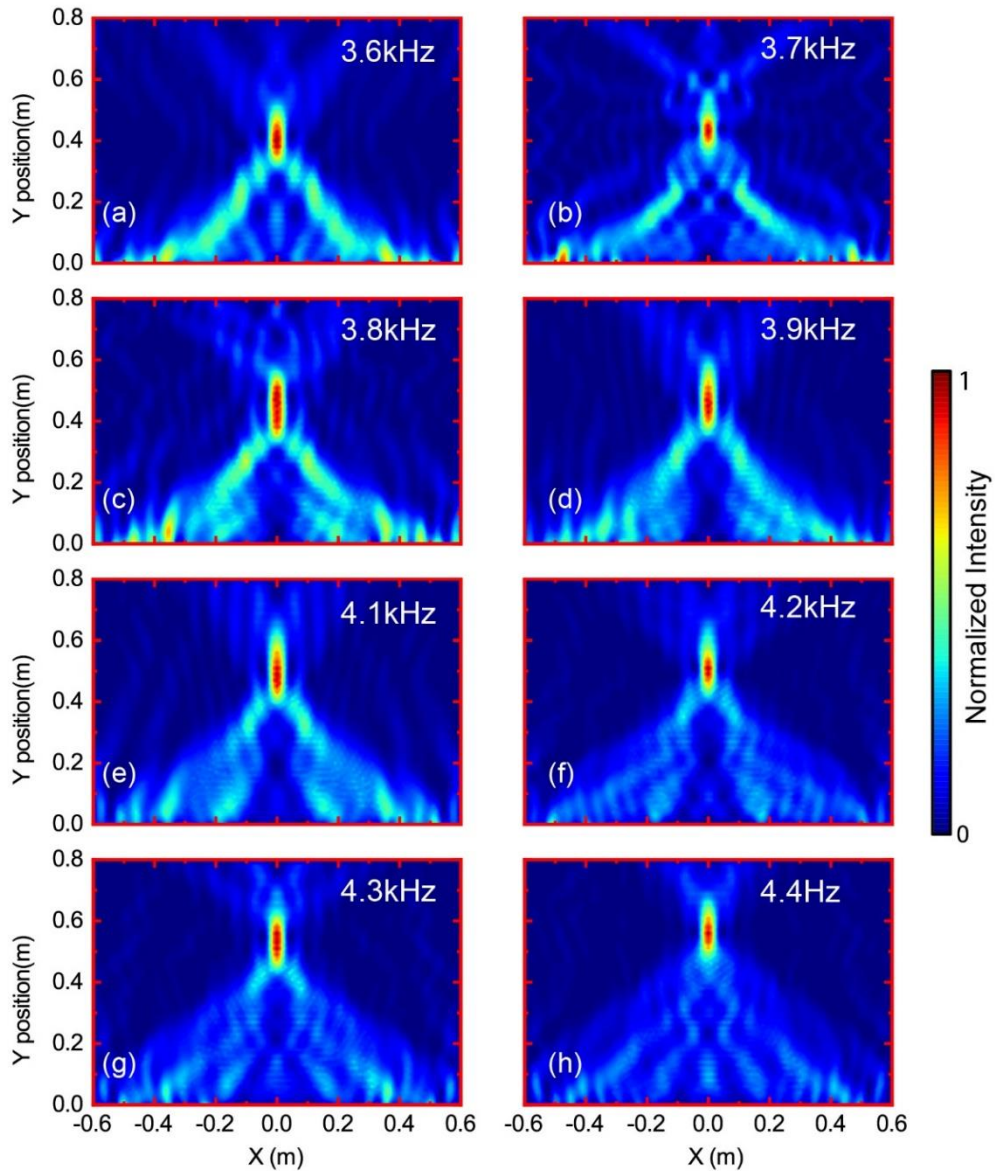


Fig. 2.22 Simulated intensity distributions at different frequencies within 3.5–4.5 kHz.

We have conducted a simulation considering the mechanical properties of the helical structure to ensure that the design can work in the practical condition. The good agreement of the field patterns in Fig. 2.23 indicates the rationality of the theoretical assumptions compared with the simulation under ideal boundary condition (rigid boundary).

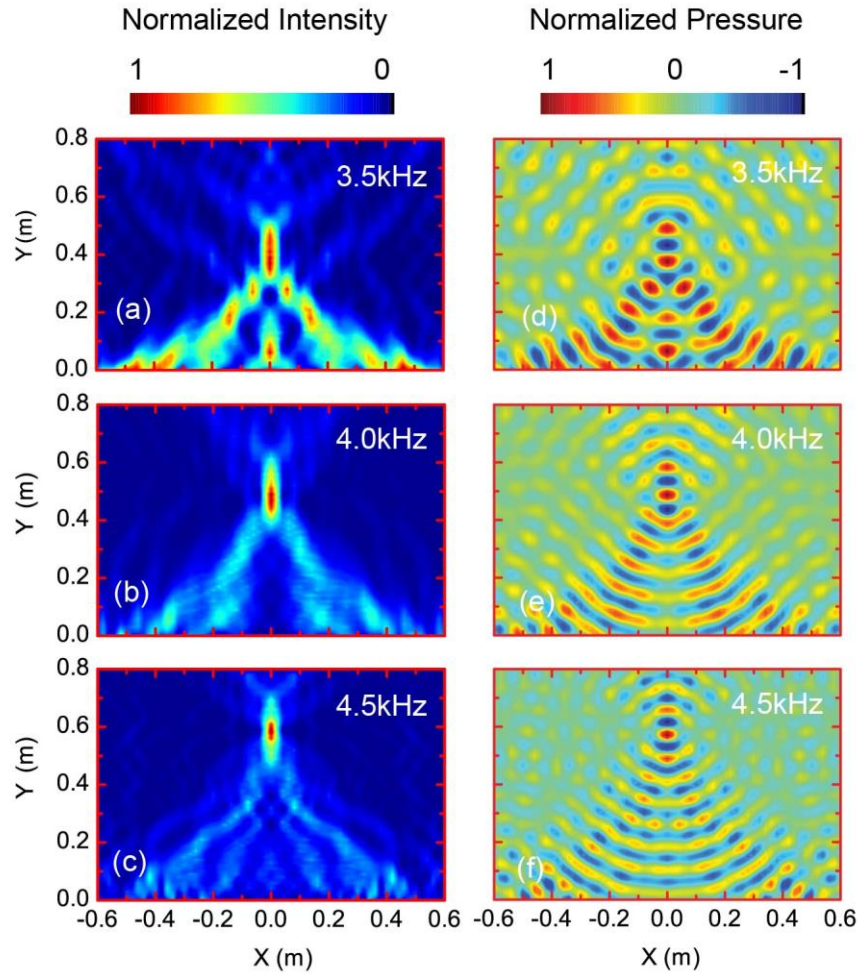


Fig. 2.23 Full-wave simulation with real structure properties. (a)–(c) and (d)–(f) are for the intensity and pressure fields.

2.3.4 Experimental setup

The unit cells are made from photosensitive resin (material type, Somos GP Plus 14122) and printed on the basis of laser sintering stereo-lithography. A self-made impedance tube is used to test the complex transmission coefficient. The parts of the tube are as follows:

1. Source, a loudspeaker (Tymphany PMT-40N25AL01-04) driven by a signal generator (Brüel and Kjær 3560D with 7539 controller modules and 3109 output modules) and a power amplifier (Brüel and Kjær Type 2706)

2. Signal collection, Brüel and Kjær type microphone 1/4 inch (Type 4935)

The transmission coefficient and phase delay of the unit cell sample have been calculated by using the transfer-matrix method and measured complex pressure.

A broadband sound focusing experiment has been conducted in half space. Thirty loudspeakers with an interval of 40 mm are used to assemble a line source and synchronously driven by Zurich Instruments HF2LI Lock-in Amplifier and a power amplifier (Brüel and Kjær Type2716C). Such task is initiated to generate an experimental plane wave. Forty-one printed unit cells are fixed by a holey frame, and the interval is 32 mm. The frame structure is manufactured by the MakerBot Z18 3D printer using PLA material. For the scanning of the field, we used a two-axis mobile platform to carry the microphone (Type 4935) for the point-by-point test. The measurement of the sound pressure is completed by the Lock-in system and software.

In the simulation and experimental setup, the lens is positioned along the X axis. The middle point of the lens is the same as the coordinate zero point. The experimentally scanned region is from -0.2 m to 0.2 m along the X axis and 0.3 m to 0.7 m along the Y axis to measure the focal spot. The plane wave source of speaker array on the other side of X axis is 70 mm away from the lens in a parallel position.

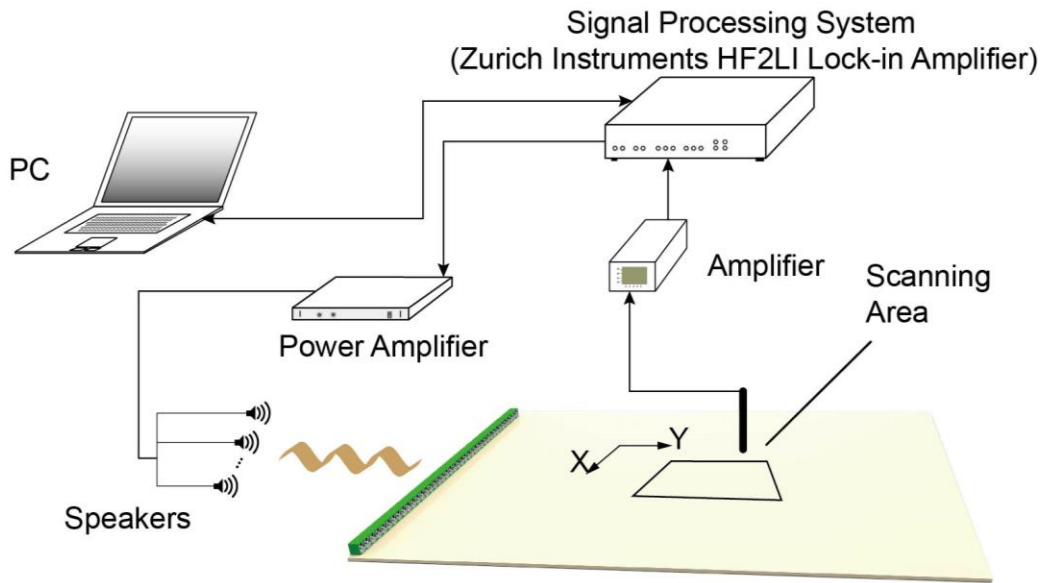


Fig. 2.24 Sound field scanning setup. The Lock-in amplifier controlled by the computer works as signal generation and data acquisition systems. Thirty speakers are in parallel to generate a plane wave positioned 0.07 m away from the meta-lens. For the scanning of the field, we measure the target region point by point with a step of 0.01 m.

I selected 3–5 kHz in Section 2.2.1 because of the performance of our lab that made the impedance tube much better in this regime. In the low frequency, the tested parameter can be influenced by the thermal and viscous loss of the duct itself. In high frequency, which is higher than the cut frequency, the high-order mode can be generated to ensure that the results lose the precision. When demonstrating the difference between two cells, the error causes a small influence on the outcome. However, when discussing the effective parameters in Section 2.2.1, an accurate data set is needed. Thus, the range 3–5 kHz can be accepted. The performance of the impedance tube can refer to Fig. 2.25. We measured the transmission of sound pressure over the spectrum because of the limited experimental conditions. In the low-frequency range (<3 kHz), a large attenuation was observed while a slight fluctuation in the high-frequency one (>5 kHz).

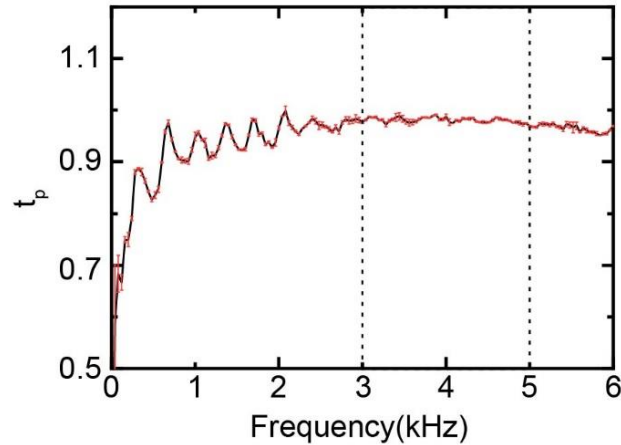


Fig. 2.25 Measured energy transmission of the empty lab-made impedance tube.

2.4 Sound amplification by GRIN unit cell

Acoustic sensors, or microphones, play an important role in defect detection. However, when a sound signal propagates in the target components, the attenuation is inevitable due to many reasons, such as diffusion, damping in the structure, and thermal and viscous loss. This kind of signal intensity decrease cannot be solved by resorting to electronic amplification methods because as the intensity may be undetectable. To solve such problem, we introduce gradient acoustic metamaterials to magnify the intensity before it converts to electrical signal. The presented helicoid structure can meet such a requirement by introducing a gradient refractive index along the propagating route. In this case, the acoustic intensity can be magnified because the wave is compressed by the gradient increasing index.

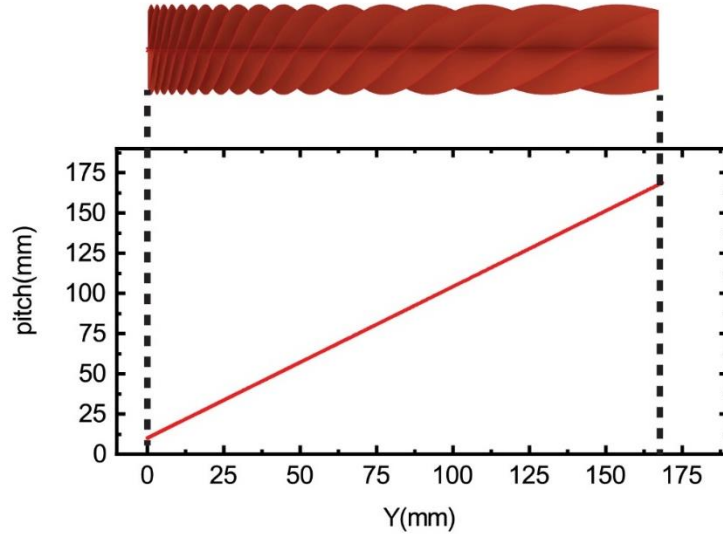


Fig. 2.26 Linearly distributed distribution of the pitch and the corresponding helicoid structure.

In practical applications, a monotone increasing helix is used to construct the structure.

Eq. (2-13) shows $p(y) = 2\pi b \cdot y + a$, where $b = 0.15$, and $a = 10$ mm. The structural pitch is determined by a and b , where the former is the pitch at the zero position, and the latter is proportional to the slope of the line. The helicoid surface can be obtained by Eq. (2-10a) to (2-10c), and its diagram is illustrated in Fig. 2.26.

The monotone increasing pitch creates a metamaterial with monotone decreasing refractive index and dynamic density, resulting in inhomogeneous media. In Section 2.2.1, the effective parameters are determined by not only the background media but also the geometrical shape, for instance, the helicoid pitch. The only parameter that governs the shape is pitch because the structural diameter remains uniform along the axis. The increasing pitch along the Y axis leads to a decreasing effective refractive index and dynamic density. The slow wave propagation behavior makes the helicoid metamaterial breaks the limitation of the refractive index, which is always smaller than one. In terms of frequency response, the excellent agreement of transmission and phase spectra between the ideal inhomogeneous media and the helicoid structure indicates the

slowly dispersive behavior of the helicoid metamaterial. On the basis of the dispersion-free property and pitch-determined parameter, the distribution of the effective parameter is equivalent to an ideal material whose index and density decrease along the Y axis. Fig. 2.27 shows the equivalent material's characteristic. On one hand, the large index can compress the wavelength. On the other hand, the similar impedance with background media weakens the reflection on the interface.

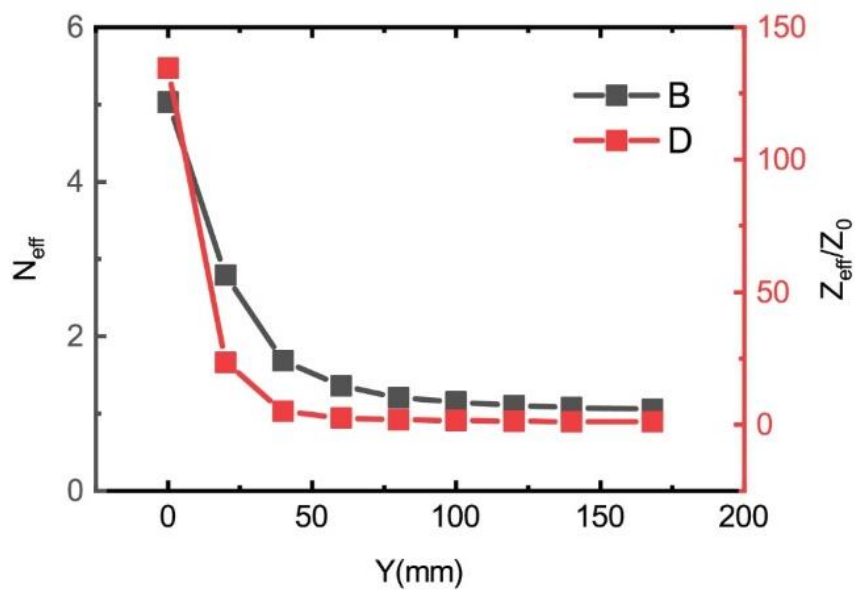


Fig. 2.27 Monotone parameter distribution of the designed gradient helicoid metamaterial.

In the simulation setup, the helicoid blades are in a cylindrical pipe with a constant radius. The plane wave incidence is parallel to the middle axis of the helicoid. The wave along the Y axis gains an increasing wave number while propagating through the pipe. The effective sound speed is ‘slow down’, while the energy flow in the pipe remains constant along the pipe. The wave compression enables pressure amplification, and the oscillating pressure gradually enhanced along the propagating direction and achieves its maximum at the N_{\max} point. The pressure amplification is different from that of active devices, in which the energy is from the electrical input. The magnitude of the

sound signal of the GRIN amplifier can be enhanced to be detected by the sensor, breaking the lower limitation of the detectable pressure for the sensor. In this case, the GRIN amplifier behaves as a passive one.

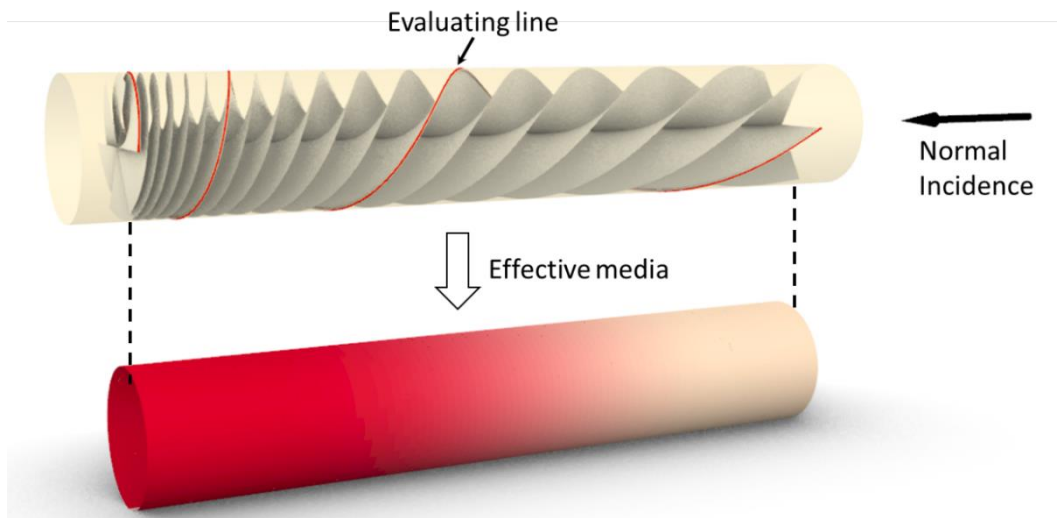


Fig. 2.28 Gradient helicoid metamaterial and its effective parameter. The evaluating line illustrates a helical curve along which the sound pressure is exported and plotted in Fig. 2.29. Fig. 2.28 shows the simulation setup. Section 2.2.1 demonstrates that the gradient-helicoid structure is regarded as a GRIN material. Fig. 2.29(a) shows the pressure field pattern considering a plane wave normal incidence to the circular cross-section in 4000 Hz. The wavelength compression from right side to left side is evident. The pressure color demonstrates the gradually amplified sound signal. In Fig. 2.29(b), the setup remains constant in spite of the replacement of the gradient-helicoid structure to a GRIN material whose parameter distribution is similar to that in Fig. 2.27. The pressure pattern is in agreement with the structure's frequency response. Hence, the agreement indicates the rationality of the equivalent material.

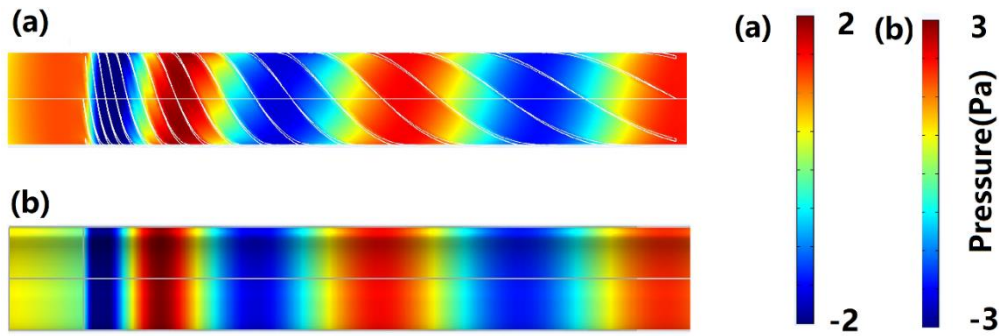


Fig. 2.29 Acoustic pressure in the gradient helicoid metamaterial. (a) and its effective medium(b) at 4000 Hz.

The slowly dispersive or nearly dispersion-free property of the helicoid metamaterial ensures broadband performance as a necessary condition. This characteristic also enables the broadband behavior of the sound amplification. Fig. 2.30 shows the full-wave simulation results to show the performance as the frequency varies. The absolute pressure along the Y axis of the structure and its equivalent material counterpart show a good similarity. The agreement indicates that the designed passive amplifier by gradient-helicoid metamaterial can work in a large frequency range, which is approximately two octaves. A slight shift is observed on the Y axis for the pressure of the helicoid metamaterial because the helicoid structure's effective length is slightly shorter than the structure.

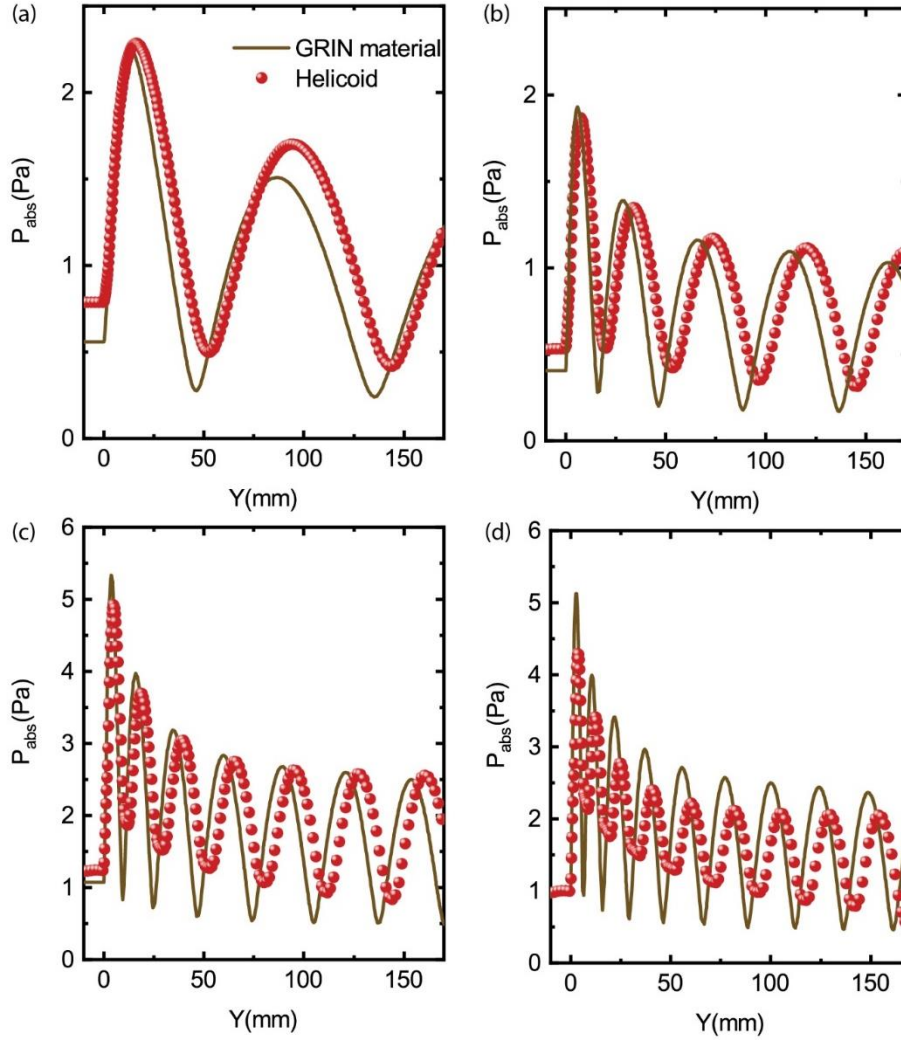


Fig. 2.30 Intensity along the Y axis. The lines illustrate the distribution of absolute pressure along the Y axis from $y=-10$ mm to $y=170$ mm. The scatters show the absolute pressure along the red line demonstrated in Fig. 2-28. Panels (a) to (d) correspond to working frequencies 1600, 3200, 4800, and 6400 Hz, respectively. For the scatters in (c), the original data of absolute pressure are half of the presented. The data have been doubled to show the pressure gain.

2.5 Summary

This chapter is divided into two aspects. The first aspect is the establishment of the gradient-helicoid metamaterials. The second one is the application demonstration. The various linear pitches along the middle axis have been established by assigning the exponential distribution of pitch with respect to the independent parameter. The dispersion-free characteristic of the uniform-pitched helical-structured metamaterial

indicates that the inhomogeneous equivalent media are in good agreement with the gradient-helicoid metamaterial, which is theoretically and experimentally verified. A detailed theoretical model has been established to evaluate the unit cell's performance and provide the possibility of inverse design from acoustic parameter distribution to its geometric parameter counterparts. The measured effective index shows the low viscous and thermal loss over the spectrum and the dispersion-free property of the graded helicoid metamaterial, adding substantial evidence for practical use.

The design of gradient pitch has two forms, namely, the 'V' shape distribution and the monotone increasing (decreasing) pitch along the middle axis. With the 'V' shape distribution of the pitch, the new helical-structured acoustic metamaterial provides enhanced impedance matching with the background medium at two ends and bridges more sound energy to counter the effects of the F-P resonance mode. A broadband meta-lens for sound focusing is designed and measured on the basis of impedance matching to the background media. Such design will not only benefit the physics research on realizing wavefront modulation with novel passive materials but also be anticipated as the new metamaterial that may be used in ultrasonography, ultrasound surgery, or DNA fragmentation, which need to focalize the energy to a specific region. We can make a gradient index by using a gradient-helicoid metamaterial to meet the requirement for obtaining extremely high sound pressure through wave compression, which can work in a wide frequency range. With the monotone increase of pitch along the middle axis, one can design a passive amplifier for the enhancement of sound pressure. When propagating through the gradient media, the wavelength is compressed by the slow down sound speed. The pressure gain achieves its maximum at the point of the large effective index. This design breaks the limitation of conventional materials' index, which is naturally smaller than one. The enhancement in broadband makes the

signal detectable with small amplitude, thereby improving the sensitivity of acoustic sensors.

Chapter 3. Flexible design of acoustic metalens

This chapter continues to discuss the design of a broadband metasurface. Based on the generalized Snell's law, the novel designed metalens composed of unit cells with square cross section displays enhanced energy transmission efficiency. Given the flexibility of the unit cell, diverse combinations of the helicoid unit cell array can be obtained by changing the positions of the unit cells. Thus, a broadband metalens is created for the anomalous refraction with changeable refractive angles. With the confirmed working capability in the broadband, the square-shaped helicoid unit cells can also behave ideally when a broadband Bessel beam launcher is built. With these functionalities, the experimental results agree well with the theoretical predictions.

3.1 Generalization of Snell's law

Snell's law governs the relationship between incident and refractive angles when wave propagates from one media to another. Derived from Fermat's law, Snell's law has the following form:

$$n_i \sin \theta_i = n_{II} \sin \theta_t, \quad (3-1)$$

where n_i and n_{II} are the refractive indices of two kinds of media; and θ_i and θ_t denote the angles of incidence and refraction, respectively. Fig. 3.1(a) illustrates the related wave path. According to Snell's law, two wave paths that are extremely close to each other have zero phase difference as follows:

$$kn_i \sin(\theta_i) dx - kn_t \sin(\theta_t) dx = 0. \quad (3-2)$$

Eq. (3-2) is equivalent to Eq. (3-1). Fig. 3.1(b) reveals that when an external phase discontinuity φ is introduced to the interface between two media by using an artificial

surface, the phase change of the wave passing through the surface can be a function with respect to the position x . With the phase discontinuity considered, the equation that maintains a zero phase difference is generalized as follows:

$$kn_i \sin(\theta_i) dx + (\varphi + d\varphi) - [kn_t \sin(\theta_t) dx + \varphi] = 0. \quad (3-3)$$

For instance,

$$n_t \sin(\theta_t) - n_i \sin(\theta_i) = \frac{1}{k} \frac{d\varphi}{dx}. \quad (3-4)$$

Eq. (3.4) is the generalized Snell's law. The new relationship provides a new design of freedom by phase engineering along the interface by using artificial structures.

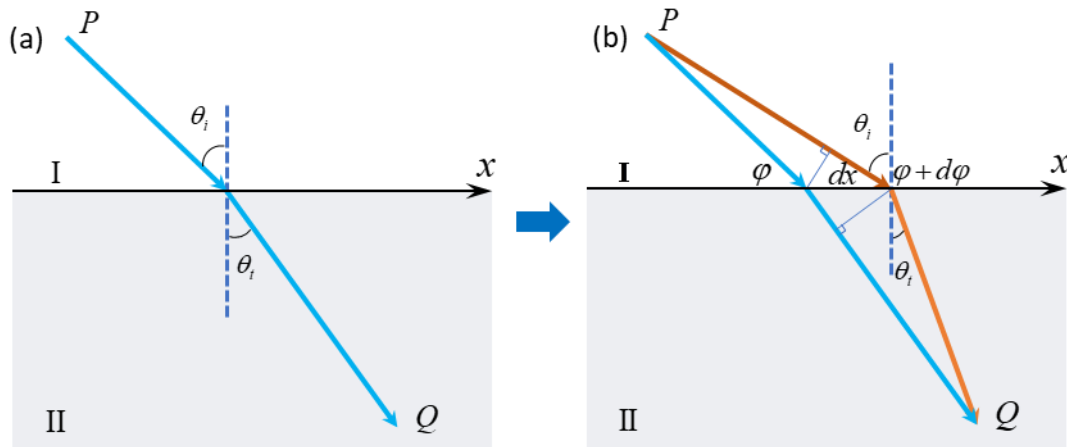


Fig. 3.1 Generalization of Snell's law. (a) Relationship of incidence and refraction on the interface between two media. (b) Change in the incident and refractive angles when a horizontal momentum is introduced along the interface

3.2 Reconfigurable metalens

3.2.1 Design

The generalized Snell's law provides the possibility of controlling wave propagation by introducing phase discontinuity, which can be realized by using a metasurface with low thickness and flexible parameter distribution. For instance, the equivalent parameter of a specific position on the metasurface is determined by the characteristic

of the unit cell at the corresponding position. Unit cells are always designed to be space-coiling structures or to consist of Helmholtz resonators to produce an extra phase delay. Fig. 3.2(a) demonstrates an array of unit cells of a gradient effective index. The change of color from red to white indicates the decreasing refractive index that introduces an increasing phase profile. The abrupt phase variation modulates the wave propagation by changing the direction of normal incidence. This strategy is used so the metasurface can modulate the wavefront. Contrary to conventional materials, metasurfaces can more flexibly change the parameter distribution. A simple reorganization of the array of unit cells may double or triple the tangent of the phase gradient. In this case, the refractive angle of the metalens will also change. Fig. 3.2(b) and (c) illustrate the new arrangement of the unit cells by selecting every second or third unit-cells from the original arrangement [Fig. 3.2(a)]. In Fig. 3.2(a), the largest phase difference is 2π , which guarantees phase continuity after the rearrangement. For the total n unit cells, the phase gradient will be as follows:

$$0, \frac{1}{n-1}\tau, \frac{2}{n-1}\tau, \dots, \tau,$$

where τ equals to the 2π corresponding to a wavelength at the operating frequency. If every second unit cells are taken to form a new array and the others are used to build another one behind, then the phase gradient changes as follows:

$$0, \frac{2}{n-1}\tau, \frac{4}{n-1}\tau, \dots, \frac{n-2}{n-1}\tau, \frac{1}{n-1}\tau, \frac{3}{n-1}\tau, \frac{5}{n-1}\tau, \dots, \tau.$$

Based on this strategy, if every third unit cells are taken out to form the original metalens, then the phase array as follows:

$$0, \frac{3}{n-1}\tau, \frac{6}{n-1}\tau, \dots, \frac{n-3}{n-1}\tau, \frac{1}{n-1}\tau, \frac{4}{n-1}\tau, \dots, \frac{n-2}{n-1}\tau, \frac{2}{n-1}\tau, \frac{5}{n-1}\tau, \frac{8}{n-1}\tau, \dots, \tau.$$

The above three phase profiles coincide with the metalens demonstrated in Figs.3.2(a)–(c), respectively.

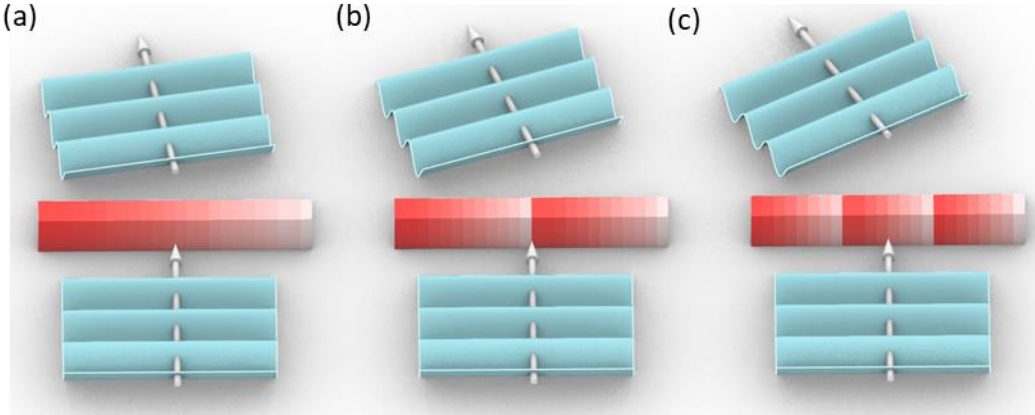


Fig. 3.2 Flexible diffractive lens for changeable anomalous refraction. (a), (b), and (c) illustrate the three working conditions of a metalens. (b) and (c) are obtained by selecting every second and third unit cells in (a) and combining these unit cells. The refractive angle is also doubled and tripled by this manipulation.

3.2.2 Realization of the metalens with multi-angle refraction

To realize the design by using a metasurface, 24 unit cells are chosen to build the metalens. Fig. 3.3 demonstrates the distribution of the design phase at the working frequency of 4000 Hz. Lens 1–3 indicate different permutations of the elements. Changing the working modes requires no new unit cells to be designed. Instead, readjusting the position of the unit cells changes their phase gradient. This strategy takes advantage of the metamaterials that cause the arrangement of elements to result in an extra freedom of design, thus introducing the flexibility of wavefront modulation.

As shown in Fig. 3.3, the red line covers the range of 2π . For the yellow and blue lines, the maximum phase is observed at some points and the difference of the neighboring

points is less than 2π , leading to slight discontinuities for the wavefront. This influence can be overcome by shrinking the size of unit cells to obtain additional elements in a period. This process will decrease the step size of the lens and increase the continuity of the wavefront.

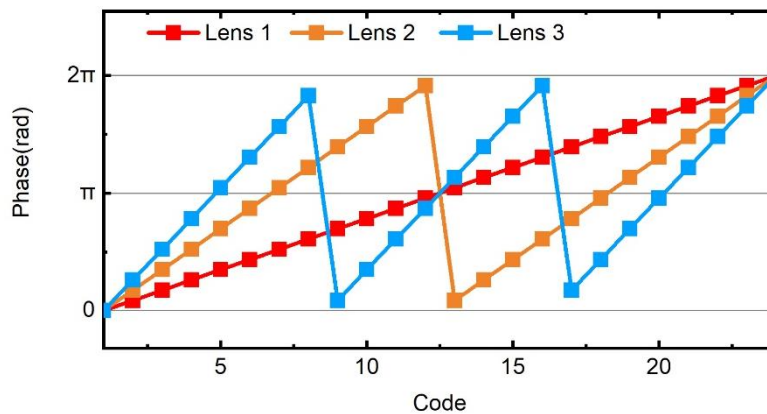


Fig. 3.3 Designed phase delay of the diffractive lens. The red line shows the phase delay of 2π with 24 unit cells coded from 1 to 24. The blue and yellow lines illustrate the arrangement by using every second and third unit cells, respectively.

Based on the phase distribution, the next step is to design the corresponding unit cells that can provide phase delay with slow wave propagation. Gradient helicoid metamaterials are adopted for the parametric design. Contrary to the previous unit cells of a circular cross section, square unit cells are used to efficiently improve the space utilization ratio. Controlled by the pitch distribution along the y-axis, the helicoid blades are wound more tightly from both ends to the middle, resulting in a gradient distribution that helps match the impedance to the background media.

The flexibility of the metalens requires unit cells to be movable and easy to fabricate. When disassembling the metalens and reassembling the parts back to the lens, the consistency of the dimensions of the unit cells facilitates its embedding into any

position. The blades and frame in this context are split. When changing the position of the unit cells, only the blades need to be pulled out and inserted into the target position.

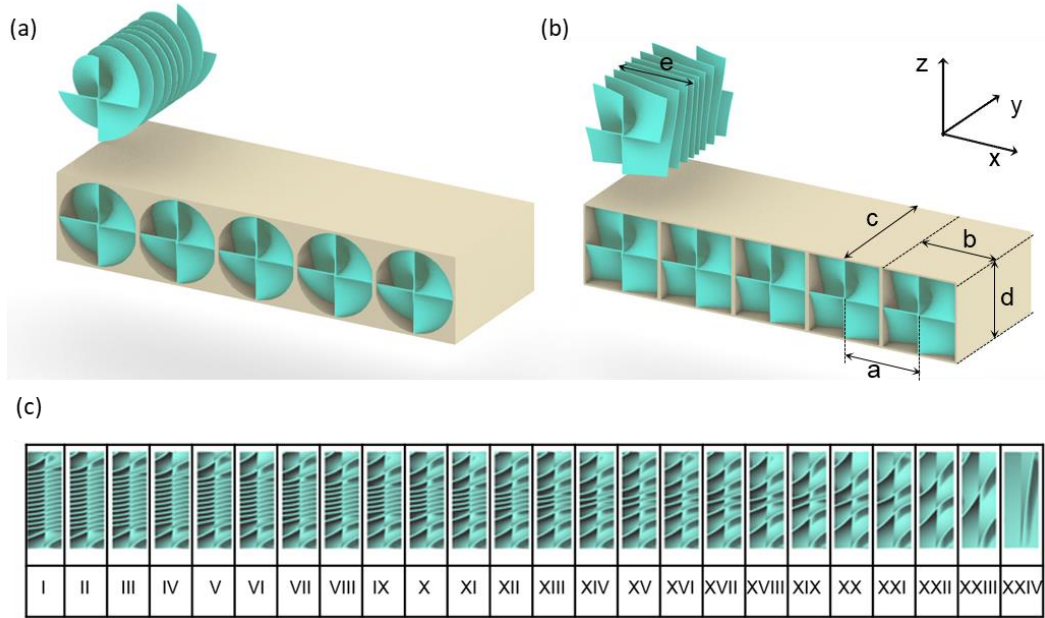


Fig. 3.4 Comparison of the circular and square helicoid blades. (a) Circular shape of the helicoid unit cell. (b) Square cross section of the unit cell, where the dimensions of the design are marked. The length, width, and height of a unit cell are $c=50$ mm, $b=19$ mm, and $d=19$ mm, respectively. The lattice parameter is $a=20$ mm. (c) Coded unit cells used to construct the multi-angle metalens.

A total of 24 unit cells are constructed to form the metalens. The top view is illustrated in Fig. 3.4(c). From left to right, the helicoid blades become looser, which corresponds to a smaller phase delay. Hence, the phase array is increasing, which coincides with the red scattering in Fig. 3.3.

The refractive angle of the lens is determined as follows:

$$\theta = \arctan \frac{2n\pi}{kl},$$

where n ($n=1, 2, 3$) is the working mode of the metalens, l (480 mm) is the length of the metalens, and k is the wavenumber. The calculated angles for $n=1, 2,$ and 3 are $9.85^\circ, 19.65^\circ,$ and $28.19^\circ,$ respectively.

The performance of a single unit cell is also tested in the given frequency. The 6th and 14th unit cells are used for computation. As shown in Fig. 3.5, a high transmission coefficient is maintained over the spectrum because of the matched impedance of the metalens and the background media. Phase shift in the same frequency range is also smooth, similar to the performance of the unit cells in Chapter 2 in the gradient helicoid metamaterial. In addition, the relationship of the phase with respect to the frequency is approximately linear, which is a necessary condition for the unit cell to delay the wavefront in the same extent over the spectrum.

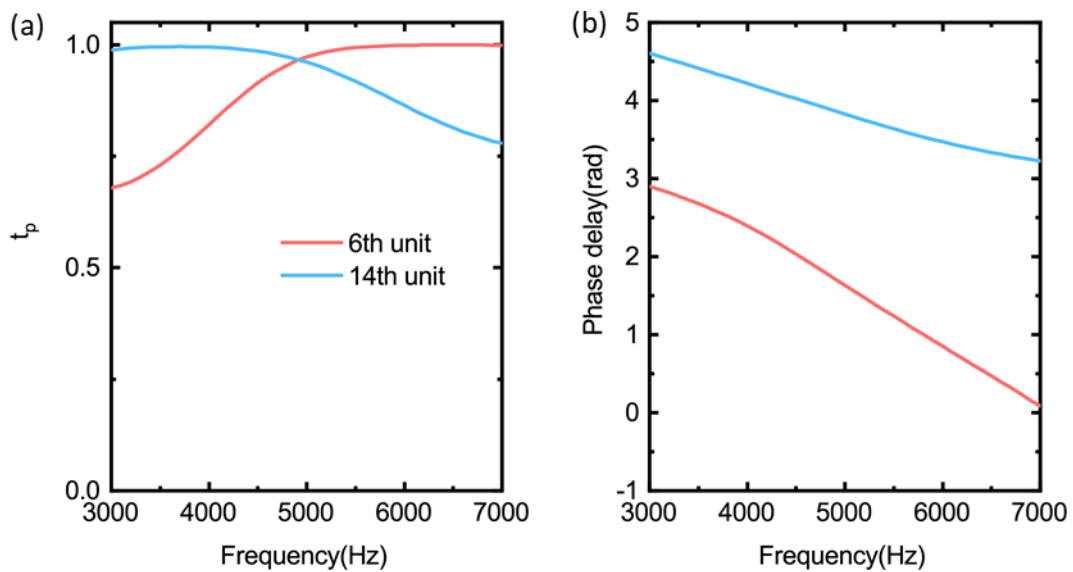


Fig. 3.5 Performance of single unit cells in the frequency domain. Transmission coefficient (a) and phase delay (b) of the unit cells over the spectrum from 3000 Hz to 7000 Hz.

The unit cells with diverse phase delays are constructed. The position of these elements should be determined first to form a metalens for anomalous refraction. The frame has 24 holes, which are marked with Arabic numbers from 1 to 24. At the same time, 24

unit-cell blades are coded by Roman numerals from I to XXIV. Table 3.1 shows the placement of the unit cells for three working modes.

Table 3.1 *The corresponding relationship between the position code and unit-cell*

Mode 1				Mode 2				Mode 3			
code	unit-cell	code	unit-cell	code	unit-cell	code	unit-cell	code	unit-cell	code	unit-cell
1	I	13	XIII	1	I	13	II	1	I	13	XIV
2	II	14	XIV	2	III	14	IV	2	IV	14	XVII
3	III	15	XV	3	V	15	VI	3	VII	15	XX
4	IV	16	XVI	4	VII	16	VIII	4	X	16	XXIII
5	V	17	XVII	5	IX	17	X	5	XIII	17	III
6	VI	18	XVIII	6	XI	18	XII	6	XVI	18	VI
7	VII	19	IXX	7	XIII	19	XIV	7	IX	19	IX
8	VIII	29	XX	8	XV	29	XVI	8	XXII	29	XII
9	IX	21	XXI	9	XVII	21	XVIII	9	II	21	XV
10	X	22	XXII	10	IX	22	XX	10	V	22	XVIII
11	XI	23	XXIII	11	XXI	23	XXII	11	VIII	23	XXI
12	XII	24	XXIV	12	XXIII	24	XXIV	12	XI	24	XXIV

At the beginning of this section, the operating frequency of the metalens was set to 4000 Hz. Given the smooth and gentle phase shift and enhanced transmission coefficient, the lens can function in the frequency range rather than at a single frequency. The behavior

of the metalens is shown in Fig. 3.6. Along the code direction (i.e., the y-axis of the lens), the unit cells placed in different arrangements show a consistent wavefront slope from 3500 Hz to 4500 Hz. This finding indicates that the metalens has a stable frequency response and an approximately constant refractive angle.

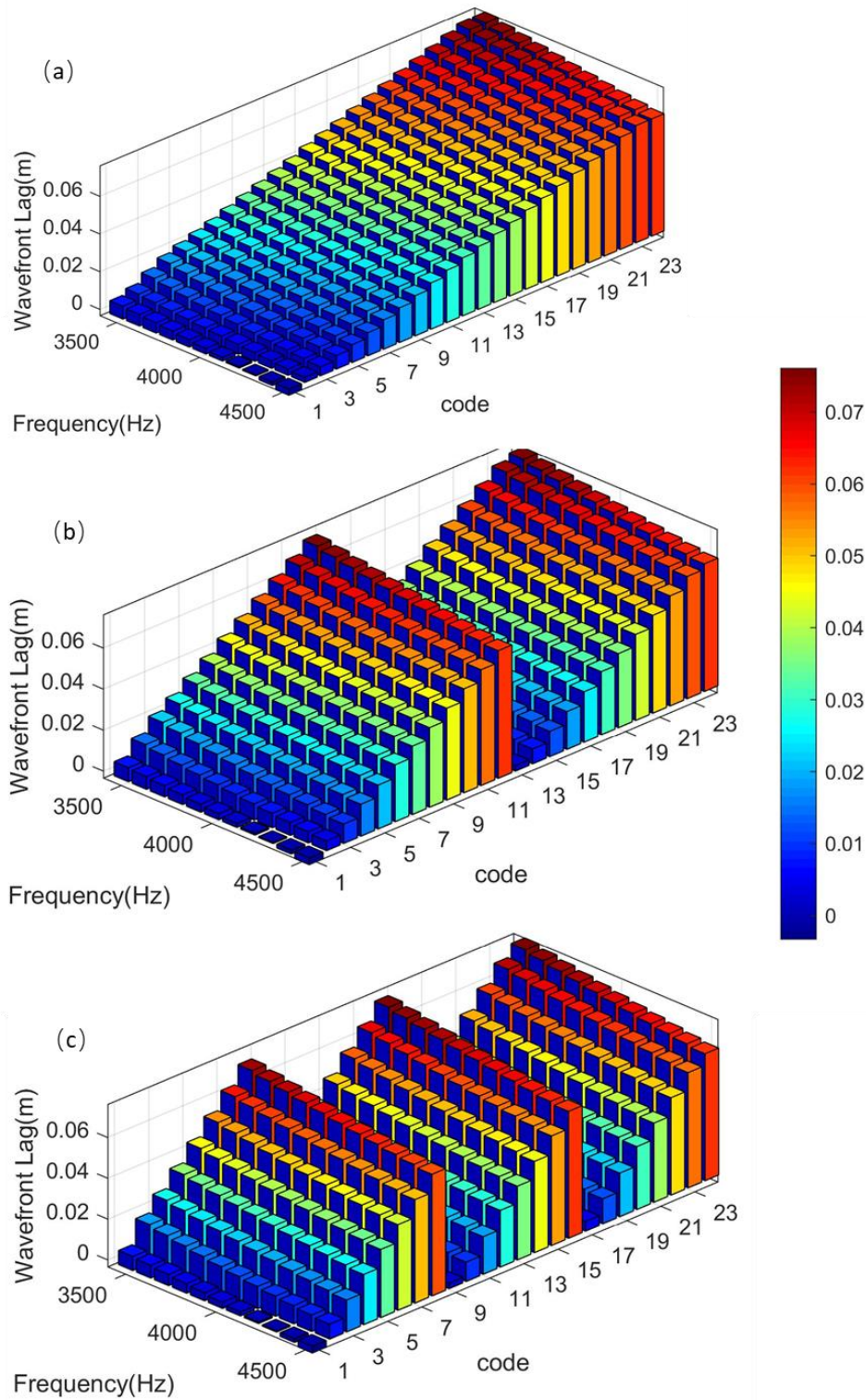


Fig. 3.6 Delay of wave propagation based on the phase. (a), (b), and (c) demonstrate the three working conditions for the three refractive angles. In (a), the unit cells are in the sequence of *i*, *ii*, *iii* ... In (b), the corresponding sequence of the unit cells is *i*, *iii*, *v*, ..., *ii*, *iv*, *vi*, ..., while the related sequence of the unit cells in (c) is *i*, *iv*, *vii*, ... *ii*, *v*, *viii*, ... *iii*, *vi*, *ix*, ... The Roman numbers are referred from Fig. 3.4(c).

For the energy transmission efficient, the transmission coefficient of the metalens is demonstrated by Fig. 3.7. The 3D bar chart shows that the transmission coefficient of the majority of unit cells is larger than 0.8 on the frequency and code axes.

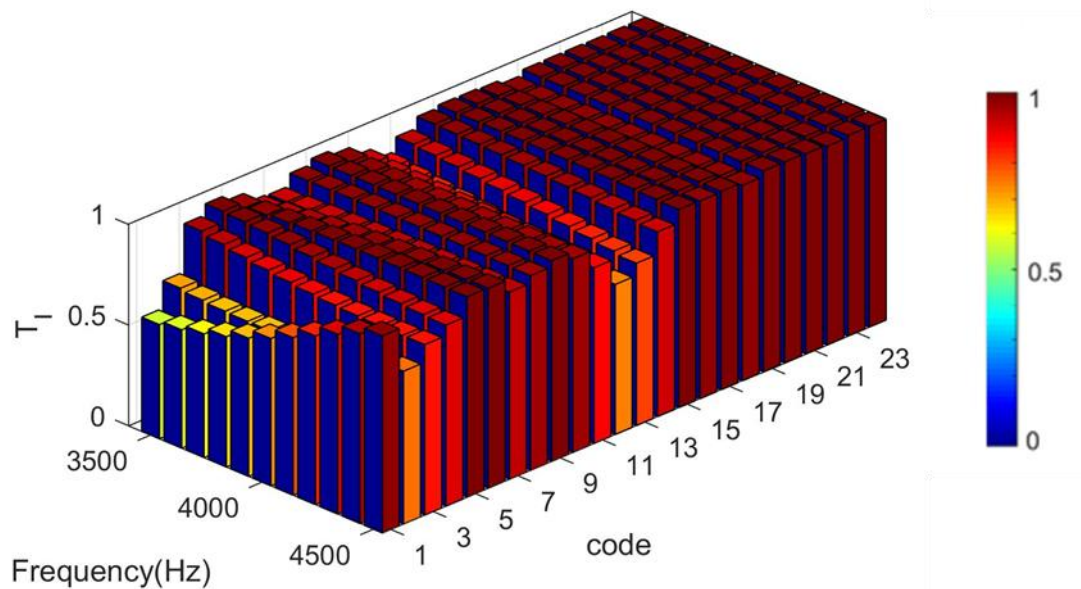


Fig. 3.7 Transmission spectrum of the designed metalens. The code axis shows the code of each unit cell, while the frequency axis shows the simulated frequency from 3500 Hz to 4500 Hz. The T_i -axis shows the corresponding energy transmission coefficient of a plane wave going through the unit cell.

During fabrication, the helicoid blades and their frame can be manufactured with high accuracy using 3D printing. The photosensitive polymer resin can be regarded as a rigid boundary that meets the theoretical results because of its mechanical strength and stiffness.

The frame and helicoid blades are printed separately to adjust flexibly the position of the unit cells. Fig. 3.8 is a photograph of the designed metalens and the inside structures. The lens has uniform width, thickness, and length. With its subwavelength thickness and flat shape, the metalens occupies lesser space than conventional acoustic devices.

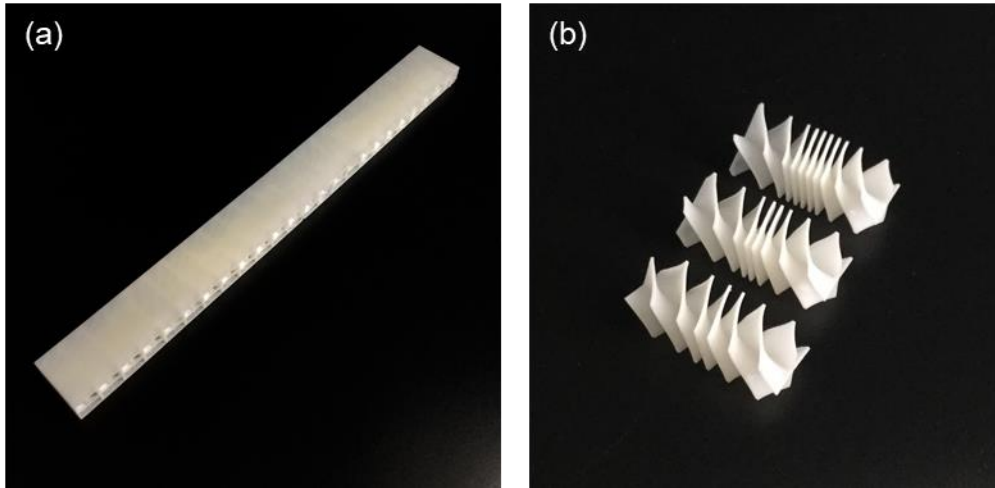


Fig. 3.8 Construction of the flat metalens. (a) The lens is composed of a frame and inner helicoid blades. The frame is a cuboid with an array of square holes. The dimensions of the design are shown in Fig. 3.4.

3.2.3 Experimental results

An experiment is set up to examine the performance of the metalens. A speaker array is used as the plane wave source. The lens is positioned in front of the speaker array, corresponding to the normal incidence condition. During its passage through the metalens, the wavefront will offset to the left-hand side of the direction of propagation. Hence, a rectangular region of the dashed line is scanned in the experiment. The influence of reflection can be avoided, and a clear pressure pattern can be obtained around the waveguide and beside the lens.

Fig. 3.10 demonstrates the sound pressure field of the metalens. The normal incident wave changes its direction with angles of approximately 10° , 20° , and 30° . The measured results show excellent agreement with the simulation results; that is, both results coincide with the designed angle. Furthermore, from the uniformly normalized pressure, the pattern shows that the intensity of the sound wave is unchanged before and after passing through the metalens. This phenomenon indicates excellent energy transmission efficiency.

The designed metalens is applicable not just for a single frequency but in a continuous frequency band. Fig. 3.11 shows the measured sound field at the neighbor of the working frequency. For the same working mode, the refractive angle is constant from 3800 Hz to 4200 Hz.

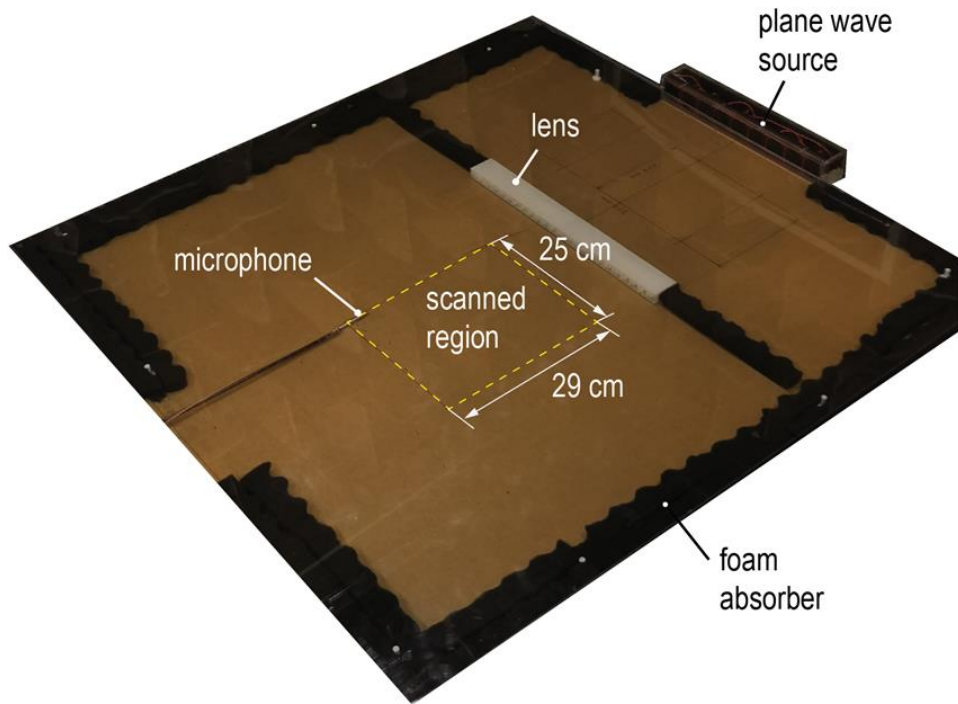


Fig. 3.9 Experimental setup for pressure field scanning. The length of the metalens is 480 mm, which can be the reference of the scale factor.

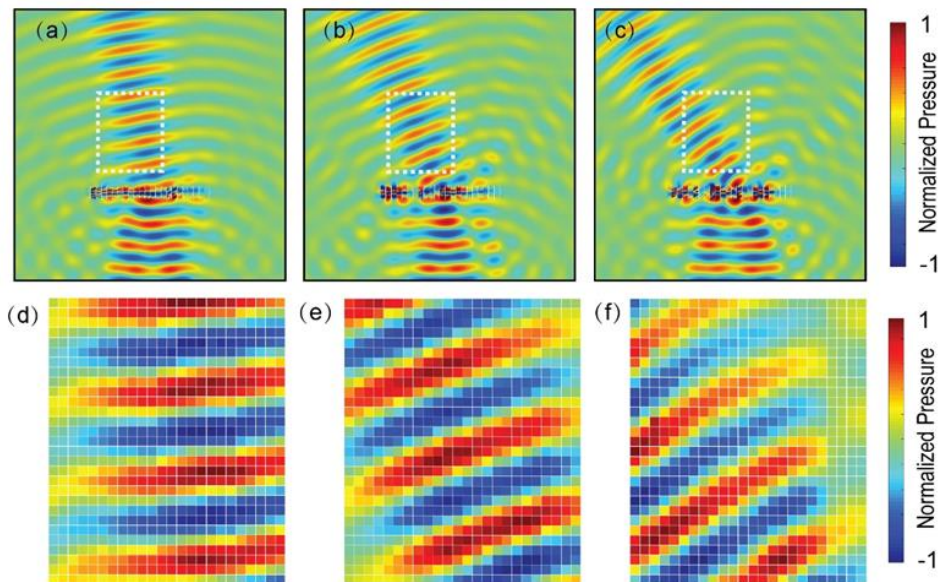


Fig. 3.10 Wavefront manipulation at 4000 Hz. (a)–(c) shows the simulation results of the sound pressure, corresponding to the three working conditions. (d)–(f) are the experimentally tested sound pressure in the scanned region shown in Fig. 3.9.

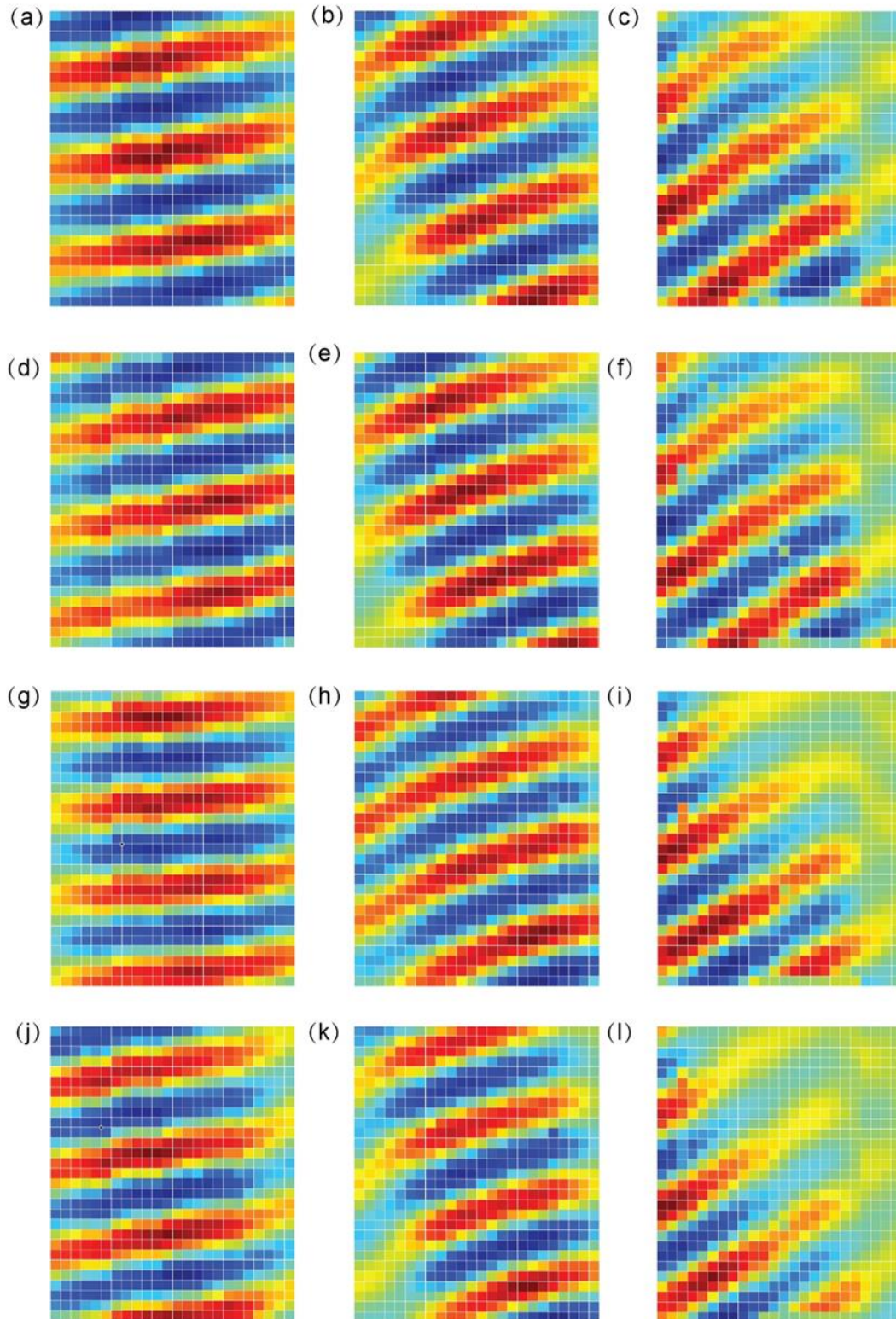


Fig. 3.11 Measured sound fields at the other frequencies. (a)–(c) 3800 Hz; (d)–(f) 3900 Hz; (g)–(i) 4100 Hz; and (j)–(l) 4200 Hz. The first column consisting of (a), (d), (g), and (j) shows the refractive angle of 0.056π . The second column consisting of (b), (e), (h), and (k) shows the refractive angle of 0.12π . The third column consisting of (c), (f), (i), and (l) shows the refractive angle of 0.17π .

3.3 Broadband Quasi Bessel beam launcher

In section 3.2, a metalens with anomalous refraction was demonstrated to have remarkable performance in a continuous frequency band. To further demonstrate the functionality of the anomalous refraction, especially for broadband utilization, a broadband Bessel beam launcher is fabricated and experimentally realized.

3.3.1 Design

The Bessel beam is a non-diffracting solution to the wave equation and was proposed by Durnin et al[100], [101] in 1987. In three-dimensional space, the field amplitude of a monochromatic wave propagating along z-axis has the form

$$\phi(x, y, z, k) = e^{j\beta z} J_0(\alpha\rho), \quad (3-5)$$

where $\alpha^2 + \beta^2 = \kappa^2$, $x^2 + y^2 = \rho^2$ and J_0 is the zeroth-order Bessel function of the first kind. The energy amount for an ideal Bessel beam is infinite, so that in practice we can just generate quasi-Bessel beams. Many metamaterial-based approaches[102]–[104] have been presented for this purpose. Notably, the high efficiency can be achieved by Huygens metasurface[103], [105]–[107]. For the two-dimensional case, one cannot generate an ideal Bessel beam as the original solution is suitable for cylindrical coordinate system. In a two-dimensional acoustic waveguide, however, Bessel-like beams can be generated by an axicon-shape device[108], [109]. The beam also preserves the outstanding features as an ideal Bessel beam, i.e., long collimation distance, self-generation and so on.

3.3.2 Realization

Following the generation of the quasi-Bessel beam by using the axicon[104], Fig. 3.12 shows the phenomenon. The superposition of the two refracted plane wave forms the

effective region of the Bessel-like beam with a length $L=R/\sin\theta$. The metalens introduce a phase gradient to the propagating plane wave, resulting in the change of direction. Eq. (3-4) shows the relationship between the incident and transmitted wave, that is

$$\sin\theta_t - \sin\theta_i = \frac{1}{k} \frac{d\varphi}{dx}, \quad (3-6)$$

where θ_t and θ_i are the refractive angle and incident angle, respectively. For normal incidence in Fig. 3.12,

$$\sin\theta = \frac{1}{k} \frac{d\varphi}{dx}. \quad (3-7)$$

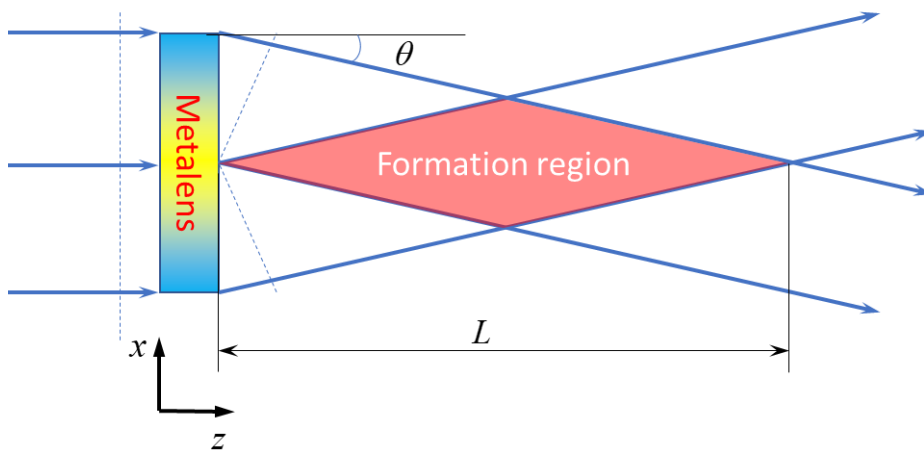


Fig. 3.12 The generation of Bessel beam based on the principle of axicon. The width of the metalens is $2R$. The length of the effective region is L . The blue-yellow-blue color range demonstrates the variation of the effective refractive index. The thickness of the metalens in this design is $l = 42\text{mm}$. The sign of θ is regarded as positive in this diagram.

For the normally incidence, the phase accumulation can only be determined by the effective velocity along the z -axis across the metalens, noted as $c(x)$. If the ratio of the sound velocity between the background media and the metalens is specified. The corresponding phase delay of the unit-cell at specific position x can be obtained being

$$\varphi(x) = l \frac{d \frac{c_0}{c(x)}}{dx} = l \frac{dN(x)}{dx}. \quad (3-8)$$

where l is the thickness of the lens, same value as the length t in Fig. 3.12 that shows the structure of building blocks, c_0 is the sound velocity of the surrounding media. In this case a parameter of the unit cell to represent its sound velocity is defined as $N(x) = c_0 / c(x)$. Substitute Eq. (3-8) back to Eq. (3-7), and one can get

$$\sin \theta = l \frac{dN(x)}{dx}. \quad (3-9)$$

Thus, once the parameter distribution $N(x)$ is determined, the obtained lens can generate a Bessel-like beam with normal incident plane wave.

On the basis of above discussion, a broadband Bessel-like beam launcher for normal incidence can be designed. In the middle of the lens, the parameter N is chosen to be 2.15, while at the edge of the lens, $N = 1$. A linearly distributed N is shown in Fig. 3.13. Because the refractive angle θ is pretty small, approximately, $\sin(\theta) \approx \tan(\theta)$. In this case, the length of the formation region along z-axis can be obtained by

$$L = \frac{R^2}{(N-1)l}. \quad (3-10)$$

Numerically, $L = 4.77m$.

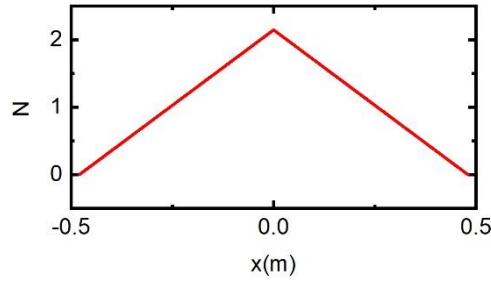


Fig. 3.13 The required distribution of N along the x axis.

The building blocks used in Chapter 3 can also be used for this purpose. However, the size should be readjusted to match the working environment. Lining up the 3D printed unit-cells, a metalens can be obtained, see Fig. 3.13. In this chapter for the Bessel-like beam launcher, thirty-one unit-cells are used to build a 0.96m wide metalens.

3.3.3. Broadband performance of the unit-cell

Previous work[110] has proved that as long as $c(x)$ keeps frequency-independent, the wavefront shape is changeless over spectrum. That means, one just need to keep the frequency-independence of the sound velocity for every unit-cells, and then the performance will not change as the frequency changes. Taking two advantages of the gradient helical structure, the designed metalens works well in a broad bandwidth. First one is the impedance marching between the metamaterial and its host media. Because the large pitch at both ends of unit-cells corresponding to the refractive index close to the surrounding medium. Second one is the naturally dispersion-free of the helicoid metamaterial proved by previous study[89]. To specifically demonstrate the performance, I chose the parameter N and transmission of a unit-cell in a frequency range from 3500Hz to 4500Hz. Details are illustrated by Fig. 3.14. It is clear that the velocity parameter $N = c_0 / c$ keeps flat over spectrum. Meanwhile, the transmission coefficient is also in a high level. The ideal performance of unit-cells guarantees the performance of the constructed metalens.

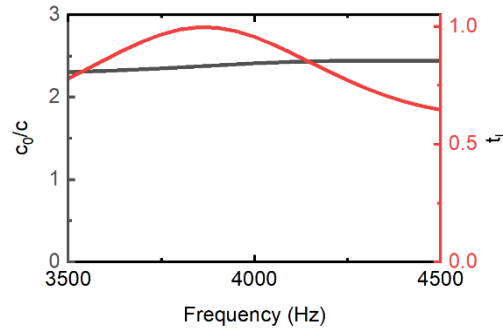


Fig. 3.14 The velocity parameter and energy transmission of a specific unit cell.

3.3.4 Experimental results

The 3D-printed unit cells are shown in Fig. 3.15. All the unit-cells have the same profile. Different helicoid blades are inside of the shells and are determined by the distribution of the pitch. The gradient helicoid unit cells inherit the excellent energy transmission efficiency and the slow wave propagation. These characteristics can delay the propagation of the wavefront to varying degrees depending on the pitch of the helicoid blades.

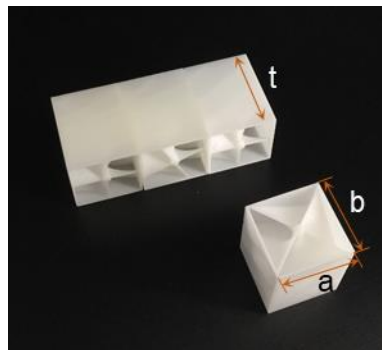


Fig 3.15 The 3D printed samples of gradient helicoid unit-cell. Related dimensions: $a=b=32\text{mm}$, $t=42\text{mm}$.

A full-wave simulation is performed to evaluate the performance of the broadband Bessel beam launcher from 3500 Hz to 4500 Hz. Thirty-one unit-cells are lined up along the x-axis. From -0.48m to 0.48m with a step of 0.032m is the position of their center axis. A plane wave incident from the left-hand side as the source. The region of the

calculated field is set to be 1.4m*6m. Around the region a 0.12m wide perfect matching layer boundary avoids the reflection.

The pressure field in Fig. 3-16 illustrates the generated of the Bessel-like beam. Compared to Fig. 3.12, the pressure pattern demonstrates a good similarity to the schematic diagram. The dark-colored region in the middle shows the Bessel-like beam propagating along the y-axis. On the left-hand side, the wavefront is in a '<' shape. It is result from the gradient velocity along the metalens. Hence, it is obvious that by using a flat lens designed above, the plane wave has been reconstrued by changing its propagating direction. The broadband behavior is firstly recognized by the consistency of the wavefront shape in spite of the wavelength. From 3500Hz to 4500Hz, the refractive angle of the lens keeps invariant. A rectangular region positioned in the middle of the field has been experimentally scanned to measure the performance of the demonstrated wavefront modulator. The experiment result shows excellent agreement with the simulation results. It is also clear that the in tested region the sound pressure has been enhanced in the middle. Furthermore, as the frequency increases, the width of the beam turns to be narrower, which is in accordance to the property of the ideal Bessel beam. To further investigate the performance of the generated Bessel-like beam, the magnitude of sound intensity has also been calculated and measured, see Fig. 3.17. In these two diagrams, the phenomenon is illustrated straightforward. One can see a long beam in the center of the region that works in a broad bandwidth from 3500Hz to 4500Hz, more than 1/3 octave. The measured result also agrees to the simulation very well. Meanwhile, the formation region in the intensity field is more obvious than the pressure pattern. The fringe in the experimentally measured region may caused by the slightly reflection of the boundary.

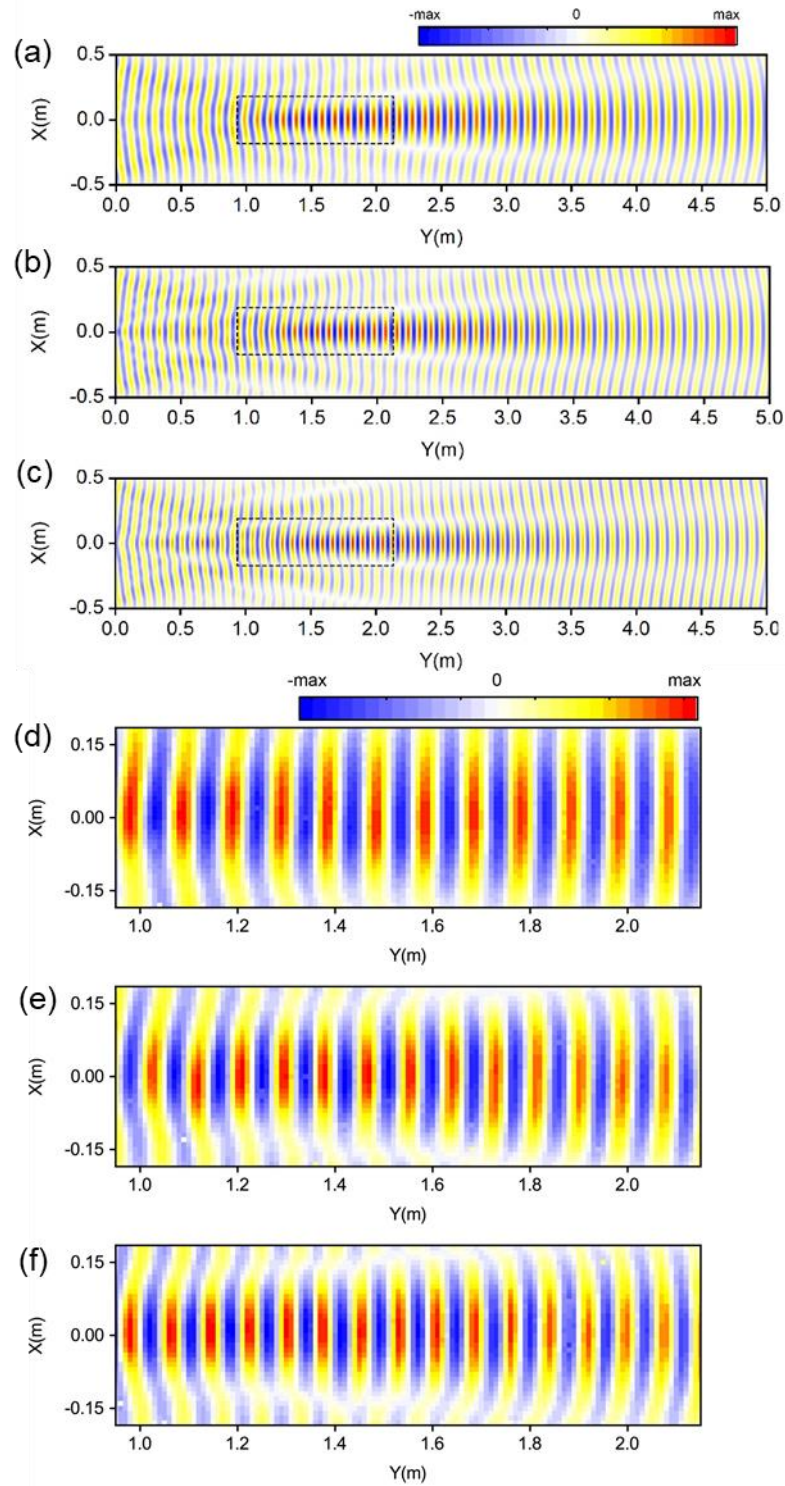


Fig. 3.16 Pressure field of the Bessel beam. (a)-(c) are the simulated pressure field at 3500Hz, 4000Hz and 4500Hz, respectively. The dashed block is the experimentally scanned region. (d)-(f) are the measure pressure field at 3500Hz, 4000Hz and 4500Hz, respectively.

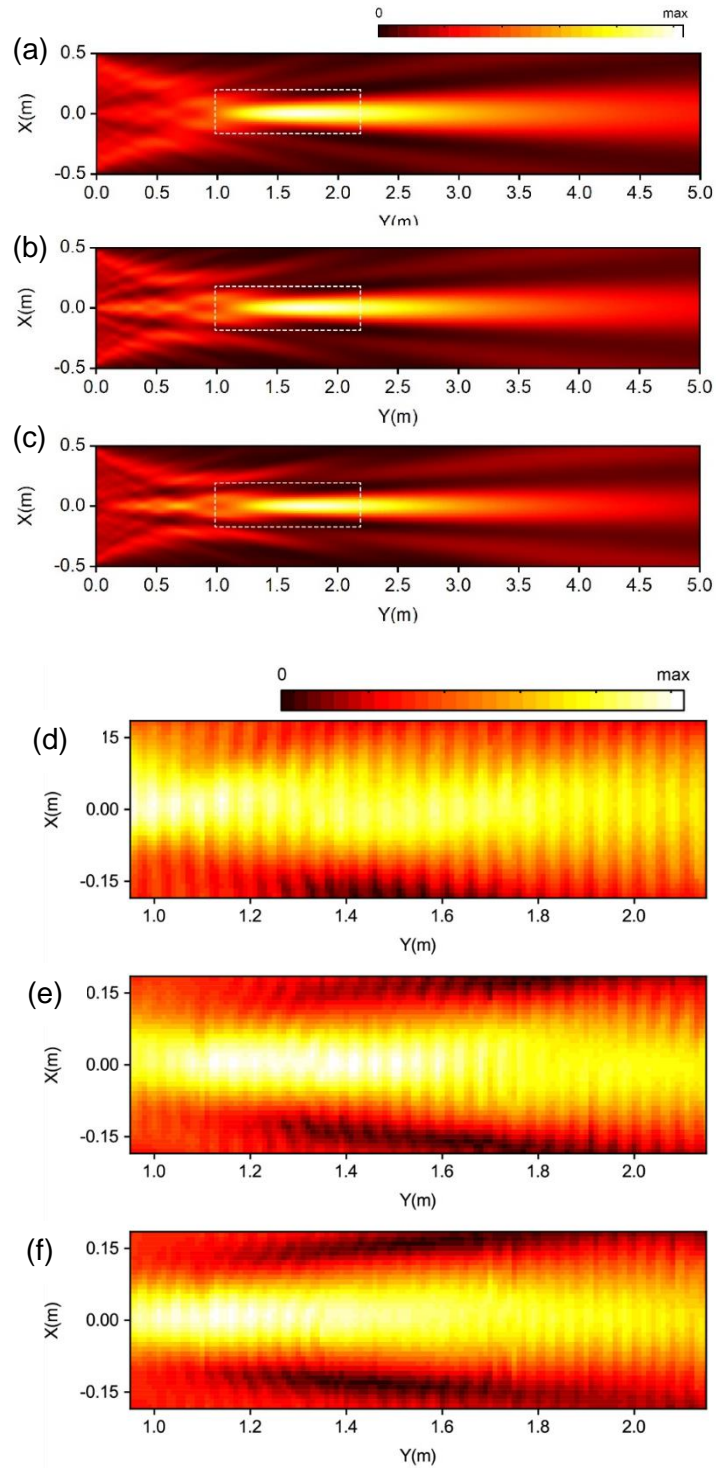


Fig. 3.17 Intensity field of the Bessel beam. (a)-(c) are the simulated intensity field at 3500Hz, 4000Hz and 4500Hz, respectively. The dashed block is the experimentally scanned region. (d)-(f) are the measure intensity field at 3500Hz, 4000Hz and 4500Hz, respectively.

In the experiment, the scanning system same to that in Chapter 2. The waveguide is built with the dimensions $1.2\text{ m} \times 2.4\text{ m}$, because the Bessel beam has a large size along the paraxial direction. A rectangular region of $0.36\text{ m} \times 1.2\text{ m}$ shows the pressure pattern based on the measured data in the experiment. The plane wave was generated by a speaker's array.

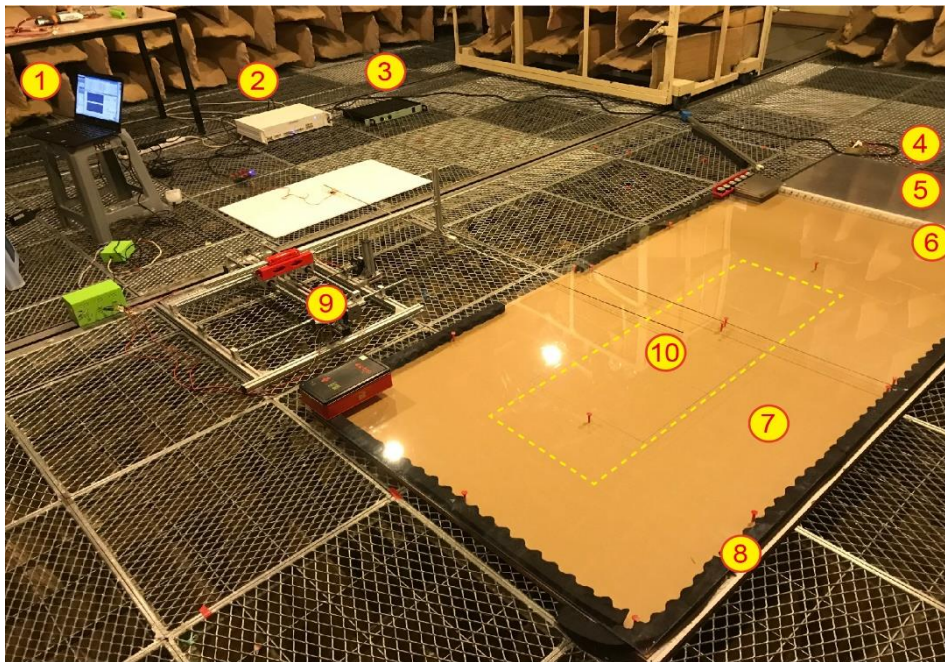


Fig 3.18 The experiment setup for broadband Bessel beam measurement. ① PC ② Lock-in amplifier ③ Power amplifier ④ Speakers' array ⑤ Plane wave guide covered with aluminum plate ⑥ Flat metalens ⑦ Wave guide covered with PMMA plate ⑧ Foam absorber ⑨ Moving system ⑩ Scanned region

As a Bessel-like beam, the property can be recognized by the concentration of wave form in a long distance. Fig. 3.19 shows the energy distribution along the x-axis cross section of the field. The results demonstrate the main branch of the beam. From 1m to 2 along the propagating direction, the colored lines show great consistency, corresponding to the focalized energy.

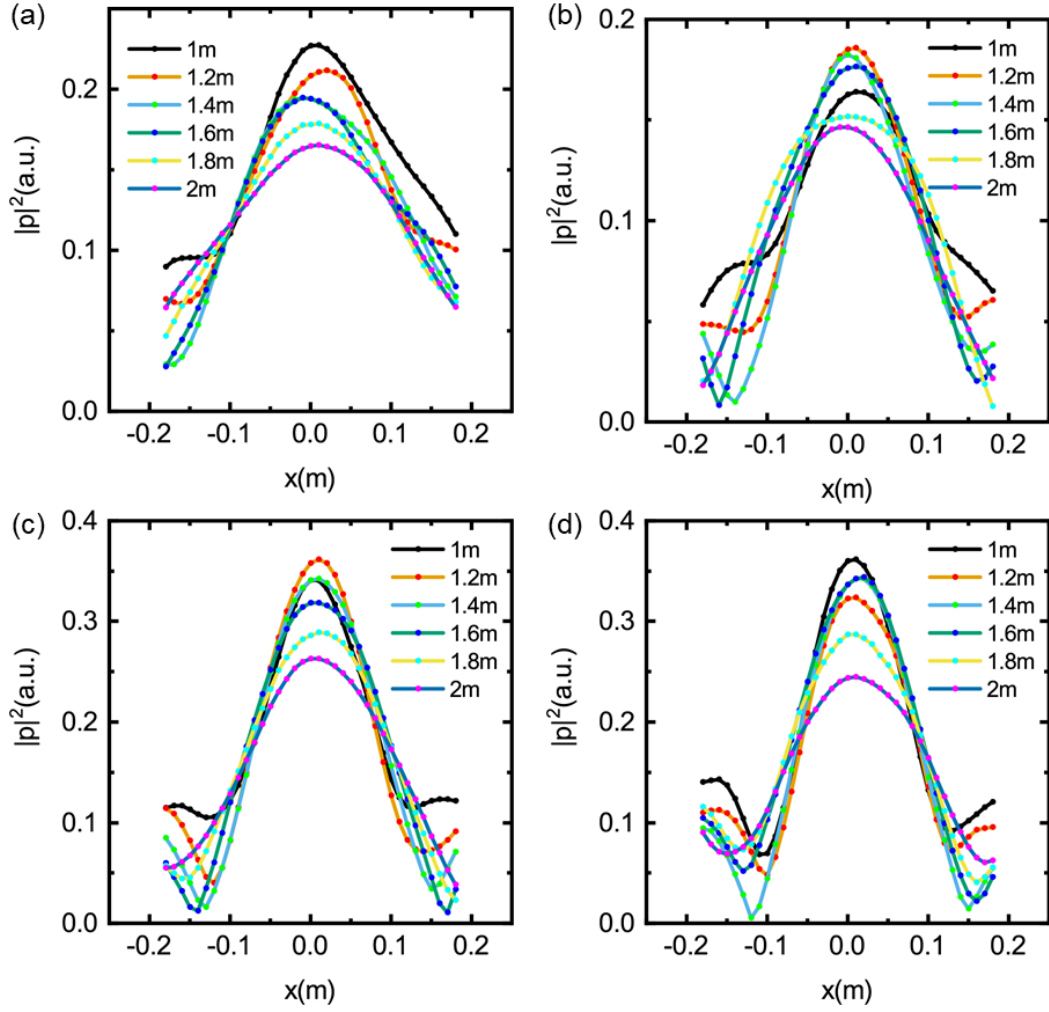


Fig. 3.19 Sound intensity distribution along the x -axis at different locations. From the black line to the blue line, the coordinates correspond to the position along the y -axis.

3.4 Summary

In this chapter, on the basis of the advantages of the gradient helicoid metamaterial, a new design strategy is proposed using the potential of a metasurface by developing its flexibility. The presented “modular design” procedure offers additional functionalities by using only one series of unit cells. No redesign process is needed when changing the working condition. Hence, a broadband metalens with adjustable refractive angles demonstrates the realization of the strategy. In the experiment, the measured result shows considerable agreement with the prediction. This design facilitates the fabrication of a multifunctional metalens to modulate the wavefront.

Furthermore, this chapter enriches the study of anomalous refraction by the practical utilization of a broadband acoustic Bessel-like beam. The performance of the metamaterial-based quasi Bessel beam launcher is experimentally demonstrated, and the experimental results show excellent agreement with the numerical results. The helicoid acoustic metamaterial with slow wave propagation and efficient energy transmission demonstrates great practicality for modulating the wavefront in broad bandwidth. The fabricated metamaterial is also a great alternative to conventional acoustic devices to save space efficiently.

Chapter 4. Spiraling-structured acoustic metamaterials

In the previous chapters, the development of a broad bandwidth and flexibility by using helicoid acoustic metamaterials is discussed. In this chapter, a more general and analytical model is established for helicoid metamaterials to gain insight into the characteristics of these materials. Hence, spiraling-structured metamaterials are introduced as the counterpart of the theory. This development allows the design of broadband metalens for 3D wavefront modulation without loss of capability for 2D functionalities. To demonstrate the performance of the novel designed metamaterial, 3D broadband wavefront converter and Bessel beam launcher are designed by the spiraling-structured metamaterials.

4.1. Equivalent medium of a tube with a segment of shrunk radius

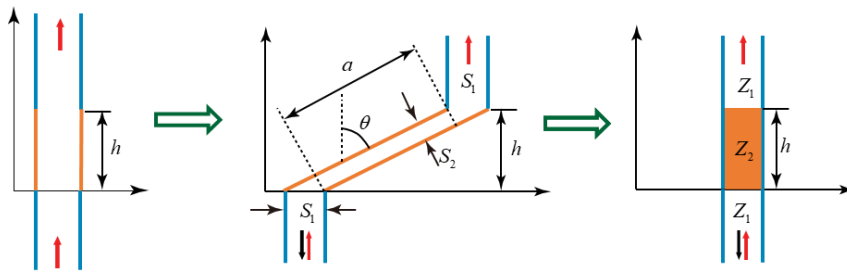


Fig. 4.1 Duct equivalence. (a) demonstrates a tube in which a segment with length h will be twisted. (b) shows the acoustically twisted structure of (a), consisting of a shrunk duct with cross-sectional area S_2 and length a in a duct of cross section S_1 . (c) illustrates the equivalent media of (b), in which the middle segment can be regarded as a material with different impedances.

In the “twisted” tube shown in Fig. 4.1(b), when the plane wave that propagates inside is lower than the cut-off frequency, the transmitted wave after passing through the slope is the same as that in Fig. 4.1(c), in which the middle shrunk segment has the same width S_2 and same length a as those in Fig. 4.1(b). Given the wave propagation in Fig.

4.1(b), the transmission coefficient of the complex sound pressure has the following form:

$$t_p = \frac{2j}{-2j \cos(k_1 a) + (S_{12} + S_{21}) \sin(k_1 a)}, \quad (4-1)$$

where $S_{12} = S_1/S_2$, $S_{21} = S_2/S_1$, and k is the wavenumber. a is the length of the middle segment. When the effect of width S_2 is neglected, a is calculated as follows:

$$a = \frac{h}{\cos \theta}. \quad (4-2)$$

Substituting Eq. (4-2) into Eq. (4-1) results in

$$t_p = \frac{2j}{-2j \cos\left(k_1 \frac{h}{\cos \theta}\right) + (S_{12} + S_{21}) \sin\left(k_1 \frac{h}{\cos \theta}\right)}, \quad (4-3)$$

which is similar to the intensity transmission for the layered media in Fig. 4.1(c). For instance,

$$t_p = \frac{2j}{-2j \cos(k_2 h) + (R_{12} + R_{21}) \sin(k_2 h)}, \quad (4-4)$$

where $R_{12} = Z_1/Z_2$, ; $R_{21} = Z_2/Z_1$; and k_1 and k_2 are the wavenumbers of the background media and the middle layer, respectively. A comparison of Eq. (4-3) and (4-4) clearly shows the similarity of the two equations. Hence, when the frequency response is considered, the twisted tube has the same property as the equivalent material with wavenumber $k_{eff} = k_2 = k_1 / \cos \theta$. Moreover, the effective impedance, which considers S_{ij} and R_{ij} as having impedance characteristics, takes the following form:

$$S_{ij} = R_{ji}. \quad (4-5)$$

Hence,

$$\frac{Z_2}{Z_1} = \frac{S_1}{S_2} = \frac{1}{\cos \theta}. \quad (4-6)$$

The relationship between the equivalent impedance of the twisted segment and the impedance of the background media is similar to that of the wavenumbers as follows:

$$Z_2 = Z_{eff} = \frac{Z_1}{\cos \theta}. \quad (4-7)$$

Hence, the circumference in 3D space can be easily estimated when the twisted tube is wound on a cylindrical surface, as illustrated in Fig. 4.2. The boundary of 2D schematic diagrams becomes a helical line [Fig. 4.2(a)], which is also the leading line of the orange-colored surface. In Fig. 4.2(b), a cylindrical layer of a “twisted space” is obtained, which is expected to have the same behavior as the tube in Fig. 4.1.

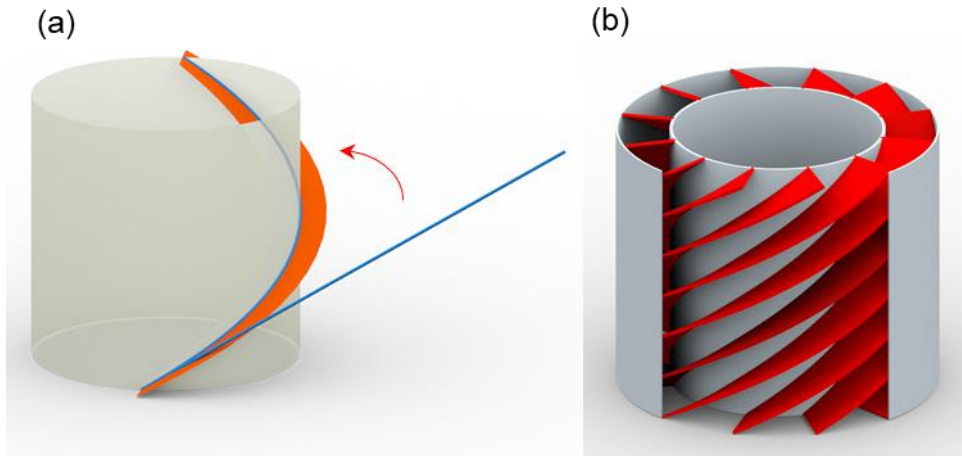


Fig. 4.2 Formation of the uniform spiraling metamaterial. (a) A straight line wound on a cylinder becomes the leading line of the spiral blade. With the middle axis of the cylinder chosen as the center of the central array, a series of blades divides the space between two concentric pipes into twisted spaces.

The equivalent parameters and frequency response are calculated to verify the similarity.

Fig. 4.3(a) shows the theoretical result of the effective media with the solid line with

$\cos \theta = 0.5$ set in the 3D model. To avoid the influence of singularity, the long wavelength signal is used in the calculation. Compared with the retrieved effective parameter of the structure in Fig. 4.2(b), the refractive index and impedance show good agreement with their theoretical counterparts. In the long wavelength condition, the effective parameters are not dependent on the frequency. The dispersion-free characteristic is not limited to the long wavelength in Fig. 4.3(a) but works in a high-frequency range. As shown in Fig. 4.3(b), the theoretically obtained parameters can describe the behavior of the structure as the wavelength close to the height of the twisted region. Figure 4.3(b) also shows the validity range of the effective medium method in frequency domain. The transmission and phase spectra show that the design works well when the wavelength is smaller than thickness of the constructed lens. To determine the upper bound of operating frequency, the cut-off frequency of the spiraling tube should be considered. For instance, substituting the longer edge length of the square tube $l = 0.01\text{m}$ and sound velocity $c_0 = 343.2\text{m/s}$ into $f_c = \frac{c_0}{2} \sqrt{\left(\frac{1}{l}\right)^2}$, the cutting-off frequency f_c is 17160Hz, much larger than the designed working frequency.

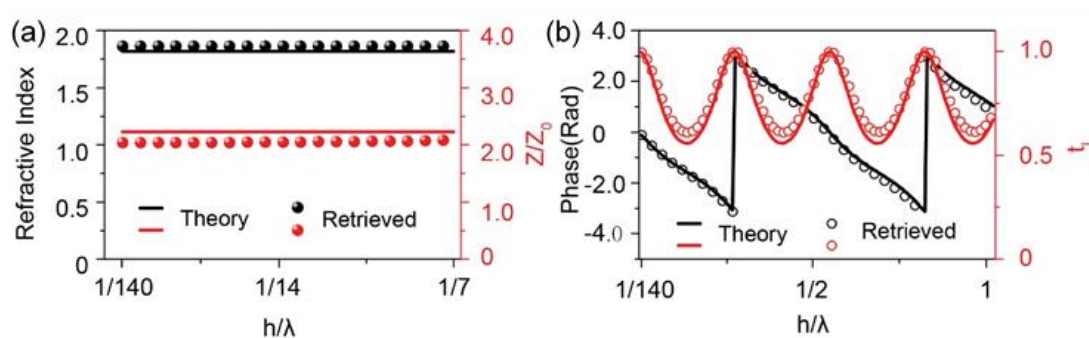


Fig. 4.3 Comparison between theoretical model and response of the structure. (a) Effective refractive index and relatively effective impedance of the uniformly spiraling structure. The results are retrieved from the transmission and reflection of the structure. The line charts demonstrate the analytically predicted parameter. (b) Transmission and phase spectra over a

frequency range, which is almost seven times larger than that in (a). The “Theory” group is calculated using the analytical model. The scatters are for the behavior of the structure.

4.2 Construction of spiralling acoustic metamaterials

On the basis of the behavior of the cylindrical layer, a novel type of metamaterial is established for slow wave propagation with dispersion-free effective parameters. This material is a generalization of the helicoid metamaterial discussed in Chapter 2. The structure with changeable diameter can work as a concentric unit cell to construct a metalens with a circular shape and radius-related index distribution. The resulting material is called a concentrically layered metalens (Fig. 4.4). Given the shape of the inner blades, these metamaterials are called spiraling metamaterials. Contrary to the conventional lattice, the unit cell of the spiraling metamaterials has a ring shape, which is suitable for the polar coordinate system. The shape of the unit cell is determined by the geometry it winds on. For example, when wound on the leading line on a cylinder, a ring-like unit cell is obtained. For a specific radius, the unit cell can be a helicoid structure shown in Chapter 2.

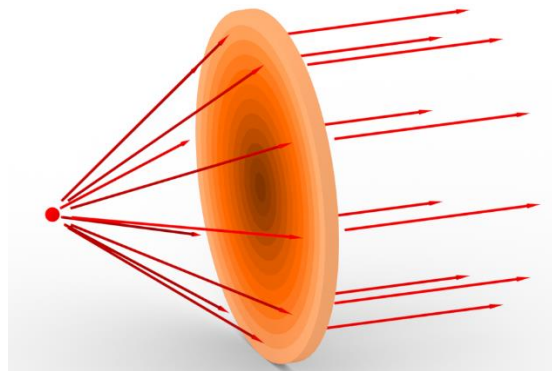


Fig. 4.4 Concentrically layered lens that can convert a spherical wave to plane wave by the gradient effective refractive index along the radius.

When the transmission coefficient of the twisted structure is considered, periodic valleys exist over the spectrum owing to the effect of the Fabry–Pérot resonance. In this

context, matching the impedance between the metamaterial and the background media is better to obtain a broad bandwidth with improved energy transmission.

From Eq. (4-2) and (4-7), the effective index and impedance have the same form. The ratio of the refractive index and the impedance between the background media and the metamaterial is equal to $1/\cos \theta$, where θ is the angle between the tangent of the leading line and the vertical direction. The angle θ of the leading line along the vertical axis will be a dependent variable with respect to the position, similar to their effective parameters, by changing the shape of the spiraling blades. This characteristic facilitates the development of a new design of spiraling metamaterial that can match the impedance to the host media. When the equation of the leading line is constructed appropriately, the spiraling blade with ideal properties can be obtained as follows:

- $\theta=90^\circ$ at both ends of the leading line. Then the effective impedance is equal to that of the host media.
- $0^\circ<\theta<90^\circ$ at the rest region. Its refractive index is larger than 1. This characteristic will slow down the wave propagation during the wavefront modulation.

The surface of a single blade at the i^{th} layer satisfies the following group of equations:

$$\begin{aligned} r(s,t) &= s, \\ \theta(s,t) &= \frac{l}{R_i} \left(\frac{t}{h} \right)^2 \left(3 - \frac{2t}{h} \right), \\ z(s,t) &= t. \end{aligned} \tag{4-8}$$

for $R_{i-1} < s < R_i$ and $0 < t < h$, where l is the parameter to adjust the degree of twisting of the blades, and h is the height of element along the z -axis (i.e., the thickness of the metalens). Note that l is the only parameter selected to control the shape of a unit cell.

The larger this parameter, the more tortuous the structure that can be obtained. This condition indicates a slower equivalent sound velocity along the z direction and a larger phase delay. For each layer for a required index, l can be uniquely identified because of the monotone relationship between l and the effective index.

The leading line of the blade's surface can be defined as the intersection to the surface $r = (R_{i-1} + R_i) / 2$. A cubic spline can be obtained by unwrapping the leading line to determine the geometrical and acoustic parameters of the layered unit. The expression of the unwrapped leading line satisfies the cubic Hermite spline function as follows:

$$L(t) = \theta(t) \frac{R_{i-1} + R_i}{2} = l \left(\frac{t}{h} \right)^2 \left(3 - \frac{2t}{h} \right). \quad (4-9)$$

In an unwrapped plane from the outer cylindrical surface, t is along the z -axis and circumferential θ -direction becomes straight and named as the L-axis.

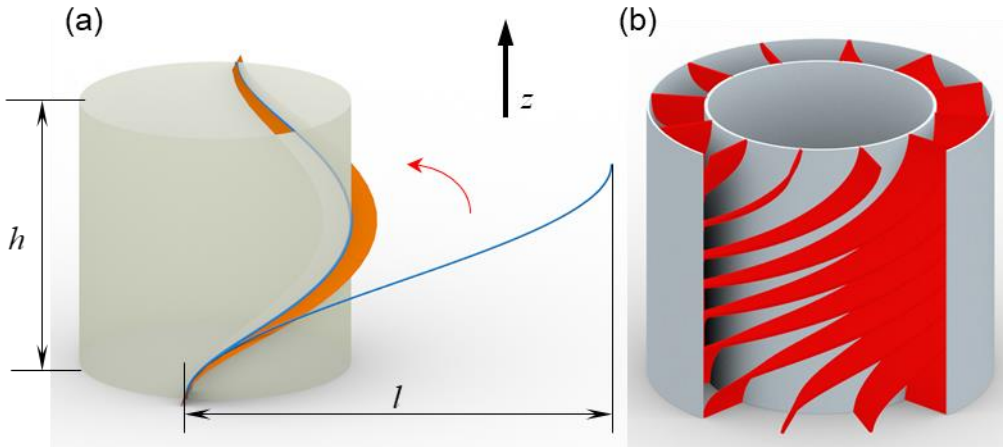


Fig. 4.5 Formation of the gradient spiraling metamaterial unit cell. With the straight line in Fig. 4.2 replaced by a Hermite spline, the wound-up leading line in (a) tend to be gradient along the axis direction of the cylinder. (b) is obtained after the same manipulation as in Fig. 4.2.

As shown in Fig. 4.5(a), l geometrically indicates the distance between the start and end points of the leading line along the circumferential direction. The cubic Hermite spline results in perfect impedance matching to the interface between the metamaterial and the host media. To illustrate, we first consider the angle between the leading line and the $z = 0$ plane and $z = h$ plane by calculating the derivative of L with respect to t . The slope of the curve can be obtained as follows:

$$\tan(\theta) = \frac{dL(t)}{dt} = \frac{6t(h-t)}{h^3}. \quad (4-10)$$

Therefore, the ratio of the parameters between the metamaterial and the background media can be determined as follows:

$$\frac{N_{eff}}{N_0} = \frac{Z_{eff}}{Z_0} = \frac{1}{\cos \theta} = \frac{1}{\cos\left(\arctan\left(\frac{dL(t)}{dt}\right)\right)} = \sqrt{1 + \left(\frac{dL(t)}{dt}\right)^2}. \quad (4-11)$$

where N_{eff} and Z_{eff} are the effective refractive index and effective impedance, respectively. Obviously, $dL(t)/dt|_{t=0,h} = 0$, which indicates that the leading line is perpendicular to the top and bottom planes (i.e., the incident and exit surfaces of the lens. In his study on helical-structured metamaterial, Ding showed that peaks and dips of transmission caused by F-P resonance can be avoided by introducing impedance-matching layers. The larger the pitch of a helical blade, the closer the effective impedance to the background media will be. The perpendicular geometrical relationship shows an infinity pitch value. Therefore, the effective impedance of the

designed lens can be regarded as equal to the background media, and this parameter can contribute to high transmission coefficients. Following Eq. (4-11), the effective impedance along the z-axis is distributed similar to that in Fig. 4.6(a).

This kind of tortuous structure prolongs the traveling path of the sound wave, resulting in a larger effective refractive index than that in air. We can evaluate

$$N_{eff} = \frac{S}{h}, \quad (4-12)$$

where $S = \int_0^h \sqrt{(Rd\theta/dt)^2 + (dz/dt)^2} dt$ and $R = (R_{i-1} + R_i)/2$. Without loss of generality, the third layer is used to numerically verify the theory and demonstrate how the parameter l determines the effective refractive index as a design variable. The increasing l stretches the curve, similar to the surface of the blade. When l is substituted into Eq. (4-9), the effective refractive index can be obtained theoretically [Fig. 4.6(b)].

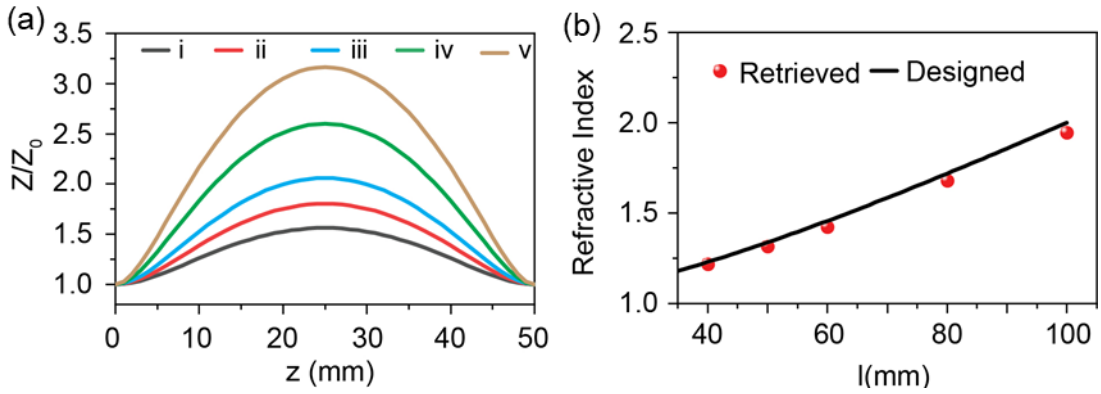


Fig. 4.6 Equivalent parameters of the gradient spiraling metamaterial. (a) Variation of the relative impedance of a unit cell along the middle axis. (b) Theoretically predicted relationship between the effective refractive index and the geometrical parameter l . The scatters show the retrieved index by using structures with the corresponding parameter l .

The calculated refractive index should be further verified to make it perform well in a practical scenario. For wave propagation, a previous study retrieved the effective index

using the transmission and reflection coefficients, and the influence of resonance is introduced. Therefore, during the design process, the geometrical parameter of the required metamaterial is not predictable only by the phase delay. A parameter sweeping is needed to determine the helicity. The novel design of perfect impedance-matching provides a stable and slowly dispersive frequency response of slow wave propagation. From Fig. 4.7(a), the delay of sound wave remains flat over the spectrum in a broad bandwidth. Fig. 4.7(b) shows the shape of the unit cell corresponding to the code in (a). From i to iv, the geometrical parameter l increasingly controls the extent of helicity.

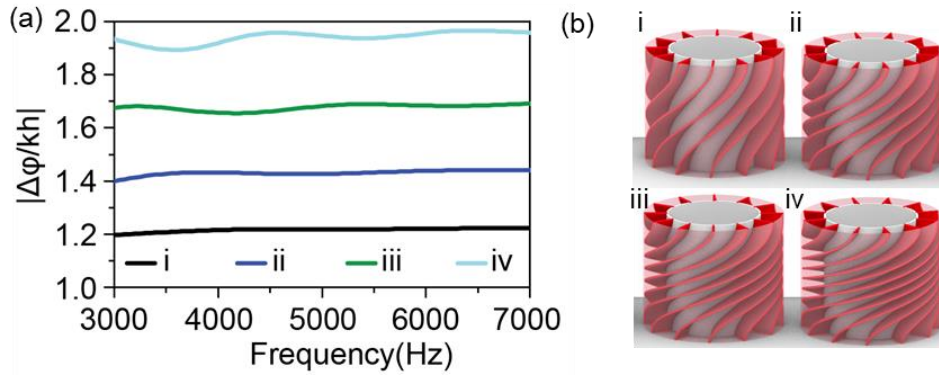


Fig. 4.7 Frequency response of the gradient spiraling metamaterial. (a) Spectrum of a dimensionless quantity that shows the delay of the wavefront from 3000 Hz to 7000 Hz. (b) Structure for the behavior in (a).

Impedance matching between the metamaterial and the background media eliminates the reflection on their interface. The spiraling metamaterial achieves impedance-matching everywhere because of the continuous variation in the acoustic parameter along the z -axis. This attribute is easy to demonstrate by cutting off part of the unit cell at both ends and calculating the transmission coefficient. As shown in Fig. 4.8, when the unit cell is cut from the top and bottom, the impedance-matching region will disappear step by step. As a result, the minimum of the transmission coefficient will decrease dramatically. Fig. 4.8(a) also shows that, for the unit cell with perfect impedance-matching layers, the valley of the energy transmission becomes shallower

as the frequency increase. This result indicates enhanced performance for high frequency.

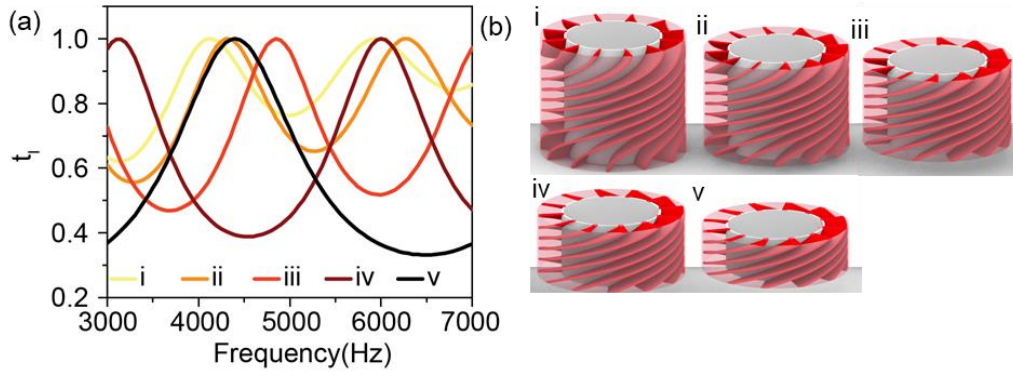


Fig. 4.8 Impedance matching of a unit cell. In (a), *i* is the original model. From *ii* to *v*, segments are cut from *i* by the planes perpendicular to the middle axis and 5, 10, 15, and 20 mm to the bottom (top) of the original structure, respectively. (b) Transmission coefficient of the corresponding structures.

The attributes of the high energy transmission and nearly dispersion-free refractive index result in an ideal acoustic device for slow wave propagation over a wide frequency range.

4.3 Broadband acoustic wavefront convertor

In this work, a ring-shaped waveguide is adopted to pair the shape of a layered cell and provide a plane wave from a spherical source. A detailed example of the construction of a wavefront converter is demonstrated in Section II. In Fig. 4.9(b), the continuously distributed index is separated into discrete values for each layer.

A spherical wavefront can be naturally generated by a point source, which is extensively used in practical scenarios, while a plane wave is another common but ideal form for generating complex cases. Therefore, a wavefront converter from the sphere wave to the plane wave is established to demonstrate the strategy of design and the performance of the new designed planar lens.

Based on the generalized acoustic Snell's law, the reshaping of the transmitted wavefront can be realized through phase engineering by passive devices. In Fig. 4.4 along the incident plane of the lens in r -direction is considered, the incident phase is as follows:

$$\varphi_i(r) = \varphi_s - k\sqrt{r^2 + d^2}, \quad (4-13)$$

where φ_s is the initial phase of the source, k is the wavenumber, and d is the distance between the source and incident plane of the lens. For the plane wave on the exit plane, the phase $\varphi_o(r)$ is subjected to the following:

$$\varphi_o(r_1) - \varphi_o(r_2) = 0, \quad (4-14)$$

where r_1 and r_2 are arbitrary positions along the r -axis.

For an impedance-matched planar lens free of resonance influence, the phase delay is determined by its thickness h and effective index $n(r)$, that is,

$$\varphi_o(r) - \varphi_i(r) = -khn(r). \quad (4-15)$$

When Eq. (4-15) is substituted into Eq. (4-13) and then the resulting equation is combined with Eq. (4-12), the required refractive index can be obtained as follows:

$$n(r_2) = n(r_1) - \frac{\sqrt{r_2^2 + d^2} - \sqrt{r_1^2 + d^2}}{h}. \quad (4-16)$$

In Eq. (4-16), let $r_1 = 0$ and $r_2 = r$,

$$n(r) = n(0) - \frac{\sqrt{r^2 + d^2} - d}{h} \quad (4-17)$$

With a given index $n(0)$ at the center of the lens, the index distribution can be uniquely identified. Fig. 4.8(b) shows a possible case when $n(0) = 2.516$.

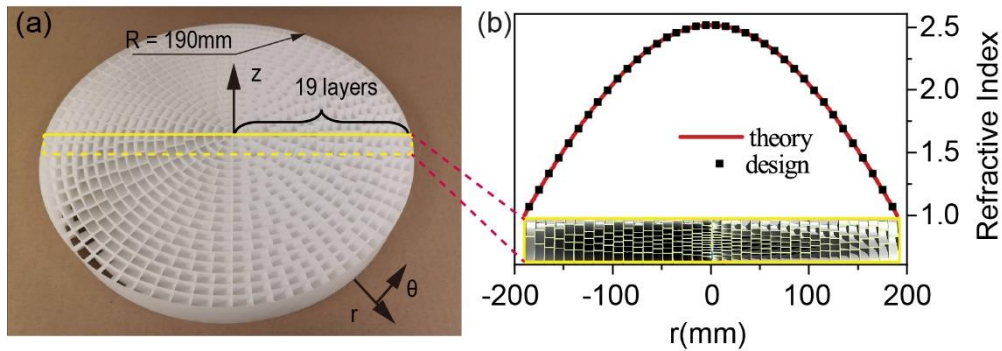


Fig. 4.9 Design of a wavefront modulator. (a) Sample of the modulator (b) Distribution of the refractive index of the lens. The red line shows the theoretically required index of the lens, while in the design, the lens is constructed layer by layer along the radial direction. Hence, the lens has a discrete index profile along its diameter.

A full wave simulation is conducted to demonstrate the functionality of the wavefront converter. The distribution of the refractive index is set to vary continuously along the radius [Fig. 4.9(b)] together with an impedance equal to that of the background media. A point source is placed in front of the lens to provide a spherical wave. In the frequency range from 3000 Hz to 7000 Hz, the lens (the rectangular region in Fig. 4.10) transforms the arc-surfaced wavefront to a plane wave. Compared with the expanded wave at the same distance to the source, the plane wave shows a larger sound pressure that is kept uniform.

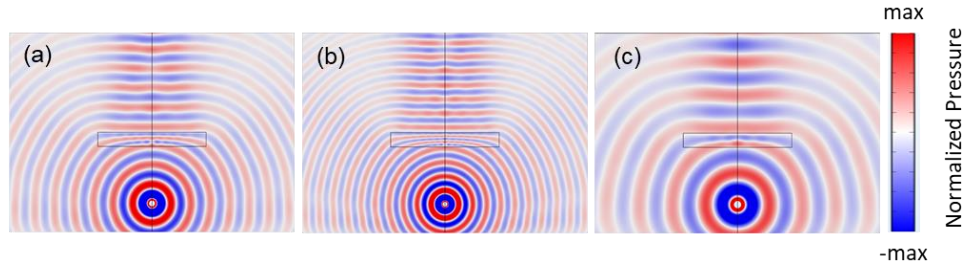


Fig. 4.10 Theoretical results of the wavefront modulator with ideal index distribution at (a) 3000, (b) 5000, and (c) 7000 Hz, respectively. The pressure patterns are normalized with the same data range.

With the geometrical model of the lens, a flat lens is manufactured by 3D printing. A measuring system is set up to test the performance of transforming sphere radiation into a plane wave in between 3000 Hz and 7000 Hz. The source is provided by a small high-frequency loudspeaker with a radius of 14 mm. The distance between source and lens is set to 200 mm. Afterward, a scanning measurement is conducted in a rectangular region on the output side of the lens. Fig. 4.11 shows the experimental configuration.

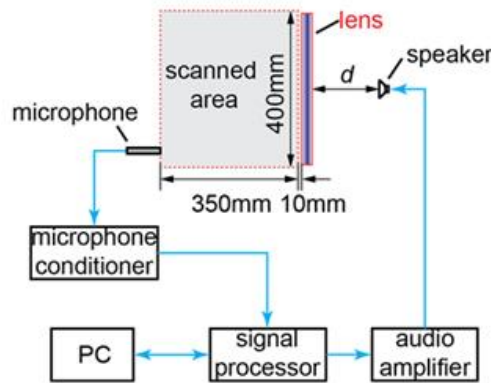


Fig. 4.11 Experimental setup to test the behavior of the broadband wavefront modulator. The whole system is in an anechoic chamber.

The metalens based on the spiraling metamaterial is in three dimensions, indicating that at least two planes are required to demonstrate the desired phenomena. The first scanned plane in the horizontal direction coincides with the diameter of the metalens. The second measurement is in the same plane as the first one. However, the circular lens is rotated to a right angle to test its vertical plane. The pressure pattern in Fig. 4.12

shows the formation of the 3D plane wave in a broadband. The spherical wavefront from the point source becomes a plane wave after passing through the lens, which is illustrated by two parallel red circles. Given the symmetry of the spherical wave, only one plane of its sound pressure is measured. The pressure pattern of the spherical wave in the vertical plane is copied from the horizontal measurement to more clearly demonstrate the phenomena. The experimental results show excellent agreement with the theoretical prediction in Fig. 4.10. Hence, a stable and consistent performance of the broadband wavefront converter is indicated.

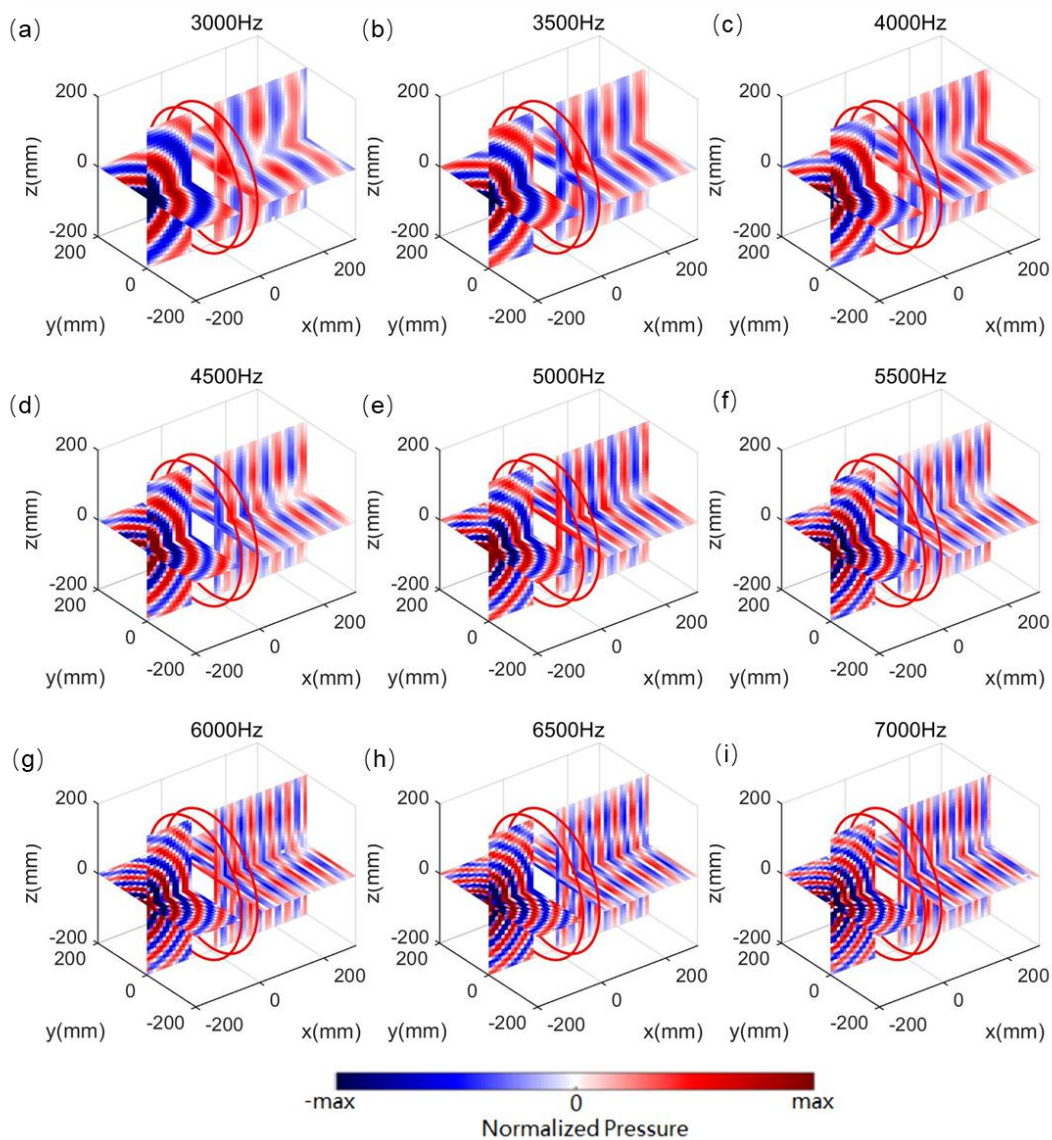


Fig. 4.12 Measured pressure pattern at both sides of the wavefront modulator. The red circular lines show the position of the modulator. (a)–(i) Pressure field from 3000 Hz to 7000 Hz with a step of 500 Hz. The values are normalized in the same data range.

To measure the energy transmission efficiency, a ratio is adopted between two arguments, one of which is the integration of sound intensity along the diameter line of the lens, and the other is the same integration as the lens is moved away. In Fig. 4.13, a decibel format of the energy transmission ratio is much larger than -3dB over the spectrum. Compared with the expansion under a free-field condition, the lens limits the expansion of the spherical wavefront, leading to the transmission ratio larger than 0 dB .

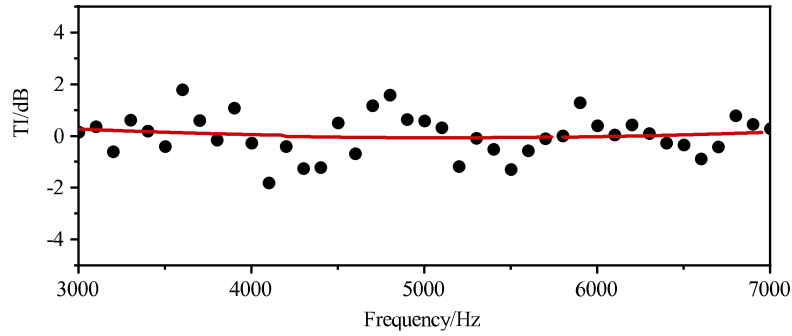


Fig. 4.13 Energy efficiency of the modulator.

Compared with the previous approaches, the proposed strategy avoids parametric sweeping in the design process when searching for an appropriate parameter. Instead, according to the required phase profile or index distribution, the construction of a broadband Fresnel lens involves only two steps: 1) the demanded refractive index distribution is discretized by the layers, and 2) the size of l for each layer is selected to match the required index.

4.4 Summary

A novel design strategy of concentrically layered lens is proposed in this chapter. I provide an analytical description of the lens to demonstrate its natural impedance

matched with the host media. The structure weakens the influence of the F-P resonance, enabling the direct prediction of the phase delay by using the effective refractive index. This step reduces the difficulty of the inverse design. A new scheme is proposed to enhance the suitability of a metalens for practical use on the basis of three merits. First, the metalens provides a nearly dispersion-free metamaterial, ensuring the uniform functionality of the device in a wide frequency range. Second, with perfect matched impedance interfaces with the host media, a high energy transmission is achieved over the spectrum. Third, when the governing parameter of the complex structure is simplified, one geometrical variable is selected to adjust the behavior of the metamaterial. Therefore, the strategy is rational for the construction of a complex index distribution. In addition, a more flexible and broadband lens can be constructed to enhance the competitiveness of metamaterials over conventional alternatives. In particular, the procedure can be employed to design an efficient wavefront modulator in acoustic imaging for the mechanical effects of the sound wave on manner and acoustic haptics. The proposed method helps in the construction of broadband absorbent walls with high strength performance.

Chapter 5. Summary and Suggestions for Future Research

5.1 Brief summary of the thesis

The introduction of this thesis briefly reviews the development of metamaterials. Specifically, it summarizes the work that makes acoustic metamaterial practical, for instance, the scheme to enhance the transparency, tunability, and flexibility. After comparison and investigation, the helical structured metamaterial is found to exhibit great potential as stated. The following section describe the state of the helicoid metamaterials and the motivation for this project, followed by the outline of the thesis.

This work starts from the helical-structured metamaterial with uniform pitch distribution along the axis. The metamaterial functions well in focusing sound by using phase engineering. Given that gradient-indexed material can improve impedance matching and enhance energy transmission, the linearly distributed pitch endows the original model with enhanced power efficiency and smooth phase shift over a broad frequency range. In theory, the gradient-pitched unit cell proves to behave similarly to a gradient-index inhomogeneous material, and this metamaterial maintains an excellent mechanical strength. The metamaterial can be an ideal alternative for broadband wave control with slow wave propagation, such as for wavefront modulation and sound amplification. Hence, a broadband focal lens composed of a helicoid metamaterial exhibits a predictable focal spot and a near 1/3 octave operating frequency band. A broadband passive amplifier also developed by using the monotone gradient helicoid metamaterial. These applications demonstrate the practical and efficient functionalities of the gradient helicoid metamaterials.

Owing to the flexibility of the helicoid blades, the cross-section of a unit cell can be changed from circular to square form to improve the space utilization rate while the unit cell inherits the characteristic from the gradient helicoid metamaterial. Meanwhile, the square cross section avoids the cavity effect of the transmitted sound wave. This type of unit cell can be used to construct an acoustic metalens with adjustable refractive angles. The designed metalens shows diverse index distribution when the arrangement of the unit cells is changed. This process results in a new phase profile to change the angle of the anomalous refraction in a broad bandwidth. This chapter develops the great potential of flexibility and adjustment for helicoid metamaterials.

On the basis of this strategy, a flat meta-lens with anomalous refraction realizes diverse refractive angles. The measured results verify the performance of the lens over the spectrum. At the same time, a broadband Bessel beam launcher is developed to experimentally demonstrate the feasibility of using the metalens. The wide frequency range of Bessel beam shows the stability of the helicoid metamaterial.

The gradient helicoid metamaterial shows great performance and can still be improved theoretically. The formation of the helicoid metamaterial is one of the specific cases of the spiraling structure. Therefore, the equivalent refractive index and equivalent impedance can be obtained analytically according to the behavior of wave propagation in a twisted tube with a variable section. Controlling the shape of the leading line of the blades enables perfect matching of the impedance to the host media on the interface to obtain a smoothly distributed impedance. This design strategy is suitable for the construction of 2D and 3D metalens for an arbitrary distribution of the index for wavefront manipulation in 3D space. The proposed design simplifies the inverse design by using the relationship between geometrical and acoustic parameters, instead of

parameter sweeping. A broadband wavefront converter from the spherical wave to the plane wave composed of the circular unit cell, as an example, indicates the flexibility and practicality of the spiraling metamaterials.

The experimentally measured field pattern and transmission efficiency show the transparency of the metamaterial for energy and stable functionality to control the wave over more than one octave in the frequency band.

5.2 Suggestions for future research

In this thesis, the helicoid and spiralling acoustic metamaterials have been investigated thoroughly both in theory and experiment. The study of wavefront modulation by using this type of acoustic metamaterial shows its excellent performance of impedance matching and energy transparency. Based on the current work, here are some possibilities that is worth exploring in the future.

1. Broadband sound absorption

This topic is based on the impedance-matching property of the gradient helicoid metamaterial and spiralling metamaterial. As is shown in Chapter 2, the gradient helicoid metamaterial has two characteristics which are good for absorption. On the one hand, it can match the impedance between two types of media. This makes it an ideal coupler for the surrounding media and the absorbers. See Fig. 6.1. This strategy is expected to broaden the bandwidth of the current absorbers. On the other hand, when pitch gradually decreases, the helicoid metamaterial can compress the wavelength, leading to energy enhancement. Meanwhile, the thermal and viscous loss increases with the decreasing pitch, and it contributes to the sound absorption function.

2. Better quality of wavefront manipulation for big angles by introducing coupling between unit-cells

The generalized laws of reflection and refraction solves the problem of phase redistribution. However, the energy distribution of the original wavefront is not applicable for the modulated wave. This is pointed out by recent works. To improve the performance of the current helicoid metamaterial, the energy redistribution of wavefronts should be a key point. One scheme that might work is to introduce coupling between unit-cells for a uniform energy distribution.

3. More general spiralling metamaterials

In Chapter 5, a cylinder is used as the basal body on which the twisted blade wraps, resulting in radial-distributed parameters, see Fig. 4.4. Actually, the basal body is diverse and not limited to three-dimensional shapes.

References

- [1] S. A. Cummer, J. Christensen, and A. Alù, “Controlling sound with acoustic metamaterials,” *Nat. Rev. Mater.*, vol. 1, no. 16001, pp. 1–14, 2016.
- [2] V. G. Veselago, “THE ELECTRODYNAMICS OF SUBSTANCES WITH SIMULTANEOUSLY NEGATIVE VALUES OF ϵ AND μ ,” *Sov. Phys. Uspekhi*, vol. 10, no. 4, pp. 509–514, 1968.
- [3] D. R. Smith, W. J. Padilla, D. C. Vier, S. C. Nemat-Nasser, and S. Schultz, “Composite medium with simultaneously negative permeability and permittivity,” *Phys. Rev. Lett.*, vol. 84, no. 18, pp. 4184–4187, 2000.
- [4] “Transmission line approach of left-handed (LH) materials and microstrip implementation of an artificial LH transmission line,” *IEEE Trans. Antennas Propag.*, vol. 52, no. 5, pp. 1159–1166, 2004.
- [5] C. R. Simovski, P. A. Belov, and S. He, “Backward Wave Region and Negative Material Parameters of a Structure Formed by Lattices of Wires and Split-Ring Resonators,” *IEEE Trans. Antennas Propag.*, vol. 51, no. 10 I, pp. 2582–2591, 2003.
- [6] P. Markoš and C. M. Soukoulis, “Numerical studies of left-handed materials and arrays of split ring resonators,” *Phys. Rev. E - Stat. Physics, Plasmas, Fluids, Relat. Interdiscip. Top.*, vol. 65, no. 3, pp. 1–8, 2002.
- [7] R. Marqués, F. Medina, and R. Rafii-El-Idrissi, “Role of bianisotropy in negative permeability and left-handed metamaterials,” *Phys. Rev. B - Condens. Matter Mater. Phys.*, vol. 65, no. 14, pp. 1–6, 2002.
- [8] C. Caloz and T. Itoh, *Electromagnetic metamaterials: transmission line theory*

- and microwave applications*. John Wiley & Sons, 2005.
- [9] C. Li and F. Li, “Two-dimensional electromagnetic cloaks with arbitrary geometries,” *Opt. Express*, vol. 16, no. 17, p. 13414, 2008.
- [10] W. X. Jiang *et al.*, “Equal-thickness invisible cloaks for arbitrarily polygonal-cylindrical regions,” *Eur. Phys. J. - Appl. Phys.*, vol. 46, no. 2, p. 20702, 2009.
- [11] W. X. Jiang, J. Y. Chin, Z. Li, Q. Cheng, R. Liu, and T. J. Cui, “Analytical design of conformally invisible cloaks for arbitrarily shaped objects,” *Phys. Rev. E - Stat. Nonlinear, Soft Matter Phys.*, vol. 77, no. 6, 2008.
- [12] T. Chen and C.-N. Weng, “Invisibility cloak with a twin cavity,” *Opt. Express*, vol. 17, no. 10, p. 8614, 2009.
- [13] D.-H. Kwon and D. H. Werner, “Polarization splitter and polarization rotator designs based on transformation optics,” *Opt. Express*, vol. 16, no. 23, p. 18731, 2008.
- [14] H. Chen, B. Hou, S. Chen, X. Ao, W. Wen, and C. T. Chan, “Design and experimental realization of a broadband transformation media field rotator at microwave frequencies,” *Phys. Rev. Lett.*, vol. 102, no. 18, pp. 1–4, 2009.
- [15] H. F. Ma, X. Chen, X. M. Yang, H. S. Xu, Q. Cheng, and T. J. Cui, “A broadband metamaterial cylindrical lens antenna,” *Chinese Sci. Bull.*, vol. 55, no. 19, pp. 2066–2070, 2010.
- [16] R. K. Luneburg and M. Herzberger, *Mathematical theory of optics*. Univ of California Press, 1964.
- [17] J. B. Pendry, “Negative refraction makes a perfect lens,” *Phys. Rev. Lett.*, vol. 85, no. 18, pp. 3966–3969, 2000.

- [18] A. Salandrino and N. Engheta, “Far-field subdiffraction optical microscopy using metamaterial crystals: Theory and simulations,” *Phys. Rev. B - Condens. Matter Mater. Phys.*, vol. 74, no. 7, pp. 1–5, 2006.
- [19] N. Yu *et al.*, “Light Propagation with Phase Discontinuities: Generalized Laws of Reflection and Refraction,” *Sci. (80-.)*, vol. 334, no. October, pp. 333–337, 2011.
- [20] F. Monticone, N. M. Estakhri, and A. Alù, “Full control of nanoscale optical transmission with a composite metascreen,” *Phys. Rev. Lett.*, vol. 110, no. 20, pp. 1–5, 2013.
- [21] C. Pfeiffer and A. Grbic, “Metamaterial Huygens’ surfaces: Tailoring wave fronts with reflectionless sheets,” *Phys. Rev. Lett.*, vol. 110, no. 19, pp. 1–5, 2013.
- [22] C. Pfeiffer, N. K. Emani, A. M. Shaltout, A. Boltasseva, V. M. Shalaev, and A. Grbic, “Efficient light bending with isotropic metamaterial Huygens’ surfaces,” *Nano Lett.*, vol. 14, no. 5, pp. 2491–2497, 2014.
- [23] M. Q. Qi, W. X. Tang, and T. J. Cui, “A broadband bessel beam launcher using metamaterial lens,” *Sci. Rep.*, vol. 5, pp. 1–11, 2015.
- [24] Y. Yang, W. Wang, P. Moitra, I. I. Kravchenko, D. P. Briggs, and J. Valentine, “Dielectric meta-reflectarray for broadband linear polarization conversion and optical vortex generation,” *Nano Lett.*, vol. 14, no. 3, pp. 1394–1399, 2014.
- [25] X. Ni, N. K. Emani, A. V. Kildishev, A. Boltasseva, and V. M. Shalaev, “Broadband light bending with plasmonic nanoantennas,” *Science (80-.)*, vol. 335, no. 6067, p. 427, 2012.
- [26] H. T. Chen, A. J. Taylor, and N. Yu, “A review of metasurfaces: Physics and

- applications,” *Reports Prog. Phys.*, vol. 79, no. 7, 2016.
- [27] Z. Liu, Z. Liu, X. Zhang, Y. Mao, and Y. Y. Zhu, “Locally Resonant Sonic Materials,” *Science (80-.)*, vol. 289, no. September, pp. 1734–1736, 2000.
- [28] G. Ma and P. Sheng, “Acoustic metamaterials: From local resonances to broad horizons,” *Sci. Adv.*, vol. 2, no. 2, p. e1501595, 2016.
- [29] N. Fang *et al.*, “Ultrasonic metamaterials with negative modulus,” *Nat. Mater.*, vol. 5, no. 6, pp. 452–456, 2006.
- [30] M. Yang, G. Ma, Z. Yang, and P. Sheng, “Coupled membranes with doubly negative mass density and bulk modulus,” *Phys. Rev. Lett.*, vol. 110, no. 13, pp. 1–5, 2013.
- [31] T. Brunet *et al.*, “Soft 3D acoustic metamaterial with negative index,” *Nat. Mater.*, vol. 14, no. 4, pp. 384–388, 2015.
- [32] Y. Ding, Z. Liu, C. Qiu, and J. Shi, “Metamaterial with simultaneously negative bulk modulus and mass density,” *Phys. Rev. Lett.*, vol. 99, no. 9, pp. 2–5, 2007.
- [33] L. Fok and X. Zhang, “Negative acoustic index metamaterial,” *Phys. Rev. B - Condens. Matter Mater. Phys.*, vol. 83, no. 21, pp. 1–8, 2011.
- [34] S. H. Lee, C. M. Park, Y. M. Seo, Z. G. Wang, and C. K. Kim, “Composite acoustic medium with simultaneously negative density and modulus,” *Phys. Rev. Lett.*, vol. 104, no. 5, pp. 1–4, 2010.
- [35] S. H. Lee, C. M. Park, Y. M. Seo, Z. G. Wang, and C. K. Kim, “Acoustic metamaterial with negative modulus,” *J. Phys. Condens. Matter*, vol. 21, no. 17, 2009.

- [36] S. H. Lee, C. M. Park, Y. M. Seo, Z. G. Wang, and C. K. Kim, “Acoustic metamaterial with negative density,” *Phys. Lett. Sect. A Gen. At. Solid State Phys.*, vol. 373, no. 48, pp. 4464–4469, 2009.
- [37] N. Kaina, F. Lemoult, M. Fink, and G. Lerosey, “Negative refractive index and acoustic superlens from multiple scattering in single negative metamaterials,” *Nature*, vol. 525, no. 7567, pp. 77–81, 2015.
- [38] J. Christensen, L. Martin-Moreno, and F. J. Garcia-Vidal, “Theory of resonant acoustic transmission through subwavelength apertures,” *Phys. Rev. Lett.*, vol. 101, no. 1, pp. 2–5, 2008.
- [39] J. Zhu *et al.*, “A holey-structured metamaterial for acoustic deep-subwavelength imaging,” *Nat. Phys.*, vol. 7, p. 52, Nov. 2010.
- [40] J. Christensen and F. J. G. de Abajo, “Anisotropic Metamaterials for Full Control of Acoustic Waves,” *Phys. Rev. Lett.*, vol. 108, no. 12, p. 124301, 2012.
- [41] V. M. García-Chocano, J. Christensen, and J. Sánchez-Dehesa, “Negative refraction and energy funneling by hyperbolic materials: An experimental demonstration in acoustics,” *Phys. Rev. Lett.*, vol. 112, no. 14, 2014.
- [42] C. Shen, Y. Xie, N. Sui, W. Wang, S. A. Cummer, and Y. Jing, “Broadband Acoustic Hyperbolic Metamaterial,” *Phys. Rev. Lett.*, vol. 115, no. 25, pp. 1–5, 2015.
- [43] G. Bartal *et al.*, “Experimental demonstration of an acoustic magnifying hyperlens,” *Nat. Mater.*, vol. 8, no. 12, pp. 931–934, 2009.
- [44] G. W. Milton, M. Briane, and J. R. Willis, “On cloaking for elasticity and physical equations with a transformation invariant form,” *New J. Phys.*, vol. 8,

- 2006.
- [45] S. A. Cummer and D. Schurig, “One path to acoustic cloaking,” *New J. Phys.*, vol. 9, no. 07, pp. 1–8, 2007.
 - [46] H. Chen and C. T. Chan, “Acoustic cloaking in three dimensions using acoustic metamaterials,” *Appl. Phys. Lett.*, vol. 91, no. 18, pp. 4–6, 2007.
 - [47] A. N. Norris, “Acoustic cloaking theory,” *Proc. R. Soc. A Math. Phys. Eng. Sci.*, vol. 464, no. 2097, pp. 2411–2434, 2008.
 - [48] A. Baz, “Active acoustic metamaterials,” *J. Acoust. Soc. Am.*, vol. 128, p. 2428, Oct. 2010.
 - [49] W. Akl and A. Baz, “Analysis and experimental demonstration of an active acoustic metamaterial cell,” *J. Appl. Phys.*, vol. 111, no. 4, 2012.
 - [50] B. I. Popa, L. Zigoneanu, and S. A. Cummer, “Tunable active acoustic metamaterials,” *Phys. Rev. B - Condens. Matter Mater. Phys.*, vol. 88, no. 2, pp. 1–8, 2013.
 - [51] X. Zhu, H. Ramezani, C. Shi, J. Zhu, and X. Zhang, “PT -symmetric acoustics,” *Phys. Rev. X*, vol. 4, no. 3, pp. 1–7, 2014.
 - [52] R. Fleury, D. Sounas, and A. Alù, “An invisible acoustic sensor based on parity-time symmetry,” *Nat. Commun.*, vol. 6, pp. 1–7, 2015.
 - [53] D. L. Sounas, R. Fleury, and A. Alù, “Unidirectional cloaking based on metasurfaces with balanced loss and gain,” *Phys. Rev. Appl.*, vol. 4, no. 1, pp. 1–11, 2015.
 - [54] T. Liu, X. Zhu, F. Chen, S. Liang, and J. Zhu, “Unidirectional Wave Vector

- Manipulation in Two-Dimensional Space with an All Passive Acoustic Parity-Time-Symmetric Metamaterials Crystal,” *Phys. Rev. Lett.*, vol. 120, no. 12, p. 124502, 2018.
- [55] Y. Xie, W. Wang, H. Chen, A. Konneker, B.-I. I. Popa, and S. A. Cummer, “Wavefront modulation and subwavelength diffractive acoustics with an acoustic metasurface,” *arXiv Prepr. arXiv1406.6306*, vol. 5, pp. 1–5, 2014.
- [56] X. Ni *et al.*, “Acoustic rainbow trapping by coiling up space,” *Sci. Rep.*, vol. 4, p. 7038, 2014.
- [57] Y. Li, B. Liang, X. Tao, X. F. Zhu, X. Y. Zou, and J. C. Cheng, “Acoustic focusing by coiling up space,” *Appl. Phys. Lett.*, vol. 101, no. 23, p. 233508, 2012.
- [58] Z. Liang and J. Li, “Extreme acoustic metamaterial by coiling up space,” *Phys. Rev. Lett.*, vol. 108, no. 11, 2012.
- [59] Z. Liang *et al.*, “Space-coiling metamaterials with double negativity and conical dispersion,” *Sci. Rep.*, vol. 3, pp. 1–6, 2013.
- [60] B. Yuan, Y. Cheng, and X. Liu, “Conversion of sound radiation pattern via gradient acoustic metasurface with space-coiling structure,” *Appl. Phys. Express*, vol. 8, no. 2, p. 027301, 2015.
- [61] K. Tang, C. Qiu, M. Ke, J. Lu, Y. Ye, and Z. Liu, “Anomalous refraction of airborne sound through ultrathin metasurfaces,” *Sci. Rep.*, vol. 4, pp. 1–7, 2014.
- [62] J. Lan, Y. Li, Y. Xu, and X. Liu, “Manipulation of acoustic wavefront by gradient metasurface based on Helmholtz Resonators,” *Sci. Rep.*, vol. 7, no. 1, p. 10587, 2017.

- [63] X. Yang, J. Yin, G. Yu, L. Peng, and N. Wang, “Acoustic superlens using Helmholtz-resonator-based metamaterials,” *Appl. Phys. Lett.*, vol. 107, no. 19, pp. 1–6, 2015.
- [64] N. Jiménez, T. J. Cox, V. Romero-García, and J. P. Groby, “Metadiffusers: Deep-subwavelength sound diffusers,” *Sci. Rep.*, vol. 7, no. 1, pp. 1–12, 2017.
- [65] Y. Chen *et al.*, “Analytical coupled vibroacoustic modeling of membrane-type acoustic metamaterials: Plate model,” *J. Acoust. Soc. Am.*, vol. 136, no. 6, pp. 2926–2934, 2014.
- [66] S. Xiao, G. Ma, Y. Li, Z. Yang, and P. Sheng, “Active control of membrane-type acoustic metamaterial by electric field,” *Appl. Phys. Lett.*, vol. 106, no. 9, 2015.
- [67] Z. Yang, J. Mei, M. Yang, N. H. Chan, and P. Sheng, “Membrane-type acoustic metamaterial with negative dynamic mass,” *Phys. Rev. Lett.*, vol. 101, no. 20, pp. 1–4, 2008.
- [68] X. P. Wang, L. Le Wan, T. N. Chen, A. L. Song, and X. W. Du, “Broadband reflected wavefronts manipulation using structured phase gradient metasurfaces,” *AIP Adv.*, vol. 6, no. 6, 2016.
- [69] G. Y. Song, B. Huang, H. Y. Dong, Q. Cheng, and T. J. Cui, “Broadband Focusing Acoustic Lens Based on Fractal Metamaterials,” *Sci. Rep.*, vol. 6, pp. 1–7, 2016.
- [70] S. Huang, B. Assouar, Y. Li, Q. Cheng, X. Wang, and X. Fang, “Acoustic perfect absorbers via spiral metasurfaces with embedded apertures,” *Appl. Phys. Lett.*, vol. 113, no. 23, p. 233501, 2018.
- [71] B. Assouar *et al.*, “Acoustic perfect absorbers via Helmholtz resonators with

- embedded apertures,” *J. Acoust. Soc. Am.*, vol. 145, no. 1, pp. 254–262, 2019.
- [72] J. Mei, G. Ma, M. Yang, Z. Yang, W. Wen, and P. Sheng, “Dark acoustic metamaterials as super absorbers for low-frequency sound,” *Nat. Commun.*, vol. 3, pp. 756–757, 2012.
- [73] Y. Zhu, X. Fan, B. Liang, J. Cheng, and Y. Jing, “Ultrathin acoustic metasurface-based schroeder diffuser,” *Phys. Rev. X*, vol. 7, no. 2, pp. 1–11, 2017.
- [74] Y. Li, X. Jiang, B. Liang, J. C. Cheng, and L. Zhang, “Metascreen-Based Acoustic Passive Phased Array,” *Phys. Rev. Appl.*, vol. 4, no. 2, pp. 1–7, 2015.
- [75] L. Kun, L. Bin, Y. Jing, Y. Jun, and C. Jian-chun, “Broadband transmission-type coding metamaterial for wavefront manipulation for airborne sound,” *Appl. Phys. Express*, vol. 11, no. 7, p. 77301, 2018.
- [76] S. Sun, Q. He, S. Xiao, Q. Xu, X. Li, and L. Zhou, “Gradient-index meta-surfaces as a bridge linking propagating waves and surface waves,” *Nat. Mater.*, vol. 11, no. 5, pp. 426–431, 2012.
- [77] P. Zhang *et al.*, “Generation of acoustic self-bending and bottle beams by phase engineering,” *Nat. Commun.*, vol. 5, pp. 1–9, 2014.
- [78] Z. Lin, X. Guo, J. Tu, Q. Ma, J. Wu, and D. Zhang, “Acoustic non-diffracting Airy beam,” *J. Appl. Phys.*, vol. 117, no. 10, 2015.
- [79] Y. Li *et al.*, “Tunable asymmetric transmission via lossy acoustic metasurfaces,” *Phys. Rev. Lett.*, vol. 119, no. 3, pp. 1–5, 2017.
- [80] Y. Zhu *et al.*, “Fine manipulation of sound via lossy metamaterials with independent and arbitrary reflection amplitude and phase,” *Nat. Commun.*, vol. 9, no. 1, pp. 1–9, 2018.

- [81] C. Ding, H. Chen, S. Zhai, S. Liu, and X. Zhao, “The anomalous manipulation of acoustic waves based on planar metasurface with split hollow sphere,” *J. Phys. D. Appl. Phys.*, vol. 48, no. 4, p. 45303, 2015.
- [82] Y.-F. F. Zhu *et al.*, “Dispersionless manipulation of reflected acoustic wavefront by subwavelength corrugated surface,” *Sci. Rep.*, vol. 5, no. February, pp. 1–12, 2015.
- [83] W. Wang, Y. Xie, A. Konneker, B.-I. Popa, and S. A. Cummer, “Design and demonstration of broadband thin planar diffractive acoustic lenses,” *Appl. Phys. Lett.*, vol. 105, no. 10, p. 101904, 2014.
- [84] Y. Tian, Q. Wei, Y. Cheng, Z. Xu, and X. Liu, “Broadband manipulation of acoustic wavefronts by pentamode metasurface,” *Appl. Phys. Lett.*, vol. 107, no. 22, 2015.
- [85] J. Lan, Y. Li, and X. Liu, “Broadband manipulation of refracted wavefronts by gradient acoustic metasurface with V-shape structure,” *Appl. Phys. Lett.*, vol. 111, no. 26, 2017.
- [86] L. Zigoneanu, B. I. Popa, A. F. Starr, and S. A. Cummer, “Design and measurements of a broadband two-dimensional acoustic metamaterial with anisotropic effective mass density,” *J. Appl. Phys.*, vol. 109, no. 5, pp. 2–7, 2011.
- [87] G. Memoli, M. Caleap, M. Asakawa, D. R. Sahoo, B. W. Drinkwater, and S. Subramanian, “Metamaterial bricks and quantization of meta-surfaces,” *Nat. Commun.*, vol. 8, pp. 1–8, 2017.
- [88] K. Li, B. Liang, J. Yang, J. Yang, and J. Cheng, “Acoustic broadband metacouplers,” *Appl. Phys. Lett.*, vol. 110, no. 20, p. 203504, 2017.

- [89] X. Zhu *et al.*, “Implementation of dispersion-free slow acoustic wave propagation and phase engineering with helical-structured metamaterials,” *Nat. Commun.*, vol. 7, no. May, pp. 1–7, 2016.
- [90] Y. Ding, E. C. Statharas, K. Yao, and M. Hong, “A broadband acoustic metamaterial with impedance matching layer of gradient index,” *Appl. Phys. Lett.*, vol. 110, no. 24, pp. 1–6, 2017.
- [91] H. Esfahlani, H. Lissek, and J. R. Mosig, “Generation of acoustic helical wavefronts using metasurfaces,” *Phys. Rev. B*, vol. 95, no. 2, p. 24312, 2017.
- [92] S. D. Zhao, A. L. Chen, Y. S. Wang, and C. Zhang, “Continuously Tunable Acoustic Metasurface for Transmitted Wavefront Modulation,” *Phys. Rev. Appl.*, vol. 10, no. 5, p. 1, 2018.
- [93] S. W. Fan, S. D. Zhao, A. L. Chen, Y. F. Wang, B. Assouar, and Y. S. Wang, “Tunable Broadband Reflective Acoustic Metasurface,” *Phys. Rev. Appl.*, vol. 11, no. 4, p. 1, 2019.
- [94] S. Liang, T. Liu, F. Chen, and J. Zhu, “Theoretical and experimental study of gradient-helicoid metamaterial,” *J. Sound Vib.*, vol. 442, pp. 482–496, 2019.
- [95] S. C. S. Lin, T. J. Huang, J. H. Sun, and T. T. Wu, “Gradient-index phononic crystals,” *Phys. Rev. B - Condens. Matter Mater. Phys.*, vol. 79, no. 9, pp. 1–6, 2009.
- [96] T. P. Martin *et al.*, “Transparent Gradient-Index Lens for Underwater Sound Based on Phase Advance,” *Phys. Rev. Appl.*, vol. 4, no. 3, pp. 1–8, 2015.
- [97] A. Håkansson, J. Sánchez-Dehesa, and L. Sanchis, “Acoustic lens design by genetic algorithms,” *Phys. Rev. B - Condens. Matter Mater. Phys.*, vol. 70, no.

- 21, pp. 1–9, 2004.
- [98] A. She, S. Zhang, S. Shian, D. R. Clarke, and F. Capasso, “Large area metalenses: design, characterization, and mass manufacturing,” *Opt. Express*, vol. 26, no. 2, p. 1573, 2018.
- [99] B. H. Song and J. S. Bolton, “A transfer-matrix approach for estimating the characteristic impedance and wave numbers of limp and rigid porous materials,” *J. Acoust. Soc. Am.*, vol. 107, no. 3, pp. 1131–1152, 2002.
- [100] J. Durnin, J. J. Miceli, and J. H. Eberly, “Diffraction-free beams,” *Phys. Rev. Lett.*, vol. 58, no. 15, pp. 1499–1501, Apr. 1987.
- [101] J. Durnin, “Exact solutions for nondiffracting beams I The scalar theory,” *J. Opt. Soc. Am. A*, vol. 4, no. 4, p. 651, 2008.
- [102] M. R. Akram, M. Q. Mehmood, T. Tauqeer, A. S. Rana, I. D. Rukhlenko, and W. Zhu, “Highly efficient generation of Bessel beams with polarization insensitive metasurfaces,” *Opt. Express*, vol. 27, no. 7, p. 9467, 2019.
- [103] Z. Lin, X. Li, R. Zhao, X. Song, Y. Wang, and L. Huang, “High-efficiency Bessel beam array generation by Huygens metasurfaces,” *Nanophotonics*, vol. 8, May 2019.
- [104] T. Shen, T. Lang, M. Wu, and Z. Han, “Bessel-like beam generated by an axicon based on parallel-plate waveguides,” *Appl. Opt.*, vol. 57, no. 21, p. 6174, 2018.
- [105] M. Kim, A. M. H. Wong, and G. V. Eleftheriades, “Optical huygens’ metasurfaces with independent control of the magnitude and phase of the local reflection coefficients,” *Phys. Rev. X*, vol. 4, no. 4, pp. 1–11, 2014.
- [106] M. Chen, M. Kim, A. M. H. Wong, and G. V. Eleftheriades, “Huygens’

- metasurfaces from microwaves to optics: A review,” *Nanophotonics*, vol. 7, no. 6, pp. 1207–1231, 2018.
- [107] L. Huang and L. Huang, “Nanophotonics High-efficiency Bessel beam array generation by Huygens metasurfaces,” vol. 8, no. 6, pp. 0–6, 2019.
- [108] H. Kurt and M. Turduev, “Two-dimensional quasi-bessel beam creation,” *Int. Conf. Opt. MEMS Nanophotonics*, no. August, pp. 219–220, 2011.
- [109] H. Kurt, “Limited-diffraction light propagation with axicon-shape photonic crystals,” *J. Opt. Soc. Am. B*, vol. 26, no. 5, p. 981, 2009.
- [110] Y. Tian, Q. Wei, Y. Cheng, Z. Xu, and X. Liu, “Broadband manipulation of acoustic wavefronts by pentamode metasurface,” *Appl. Phys. Lett.*, vol. 107, no. 22, p. 221906, 2015.